REPORT DOCUMENTATION PAGE

Form Approved OMB No. 0704-0188

1. REPORT DATE *(DD-MM-YYYY)*	2. REPORT TYPE	3. DATES COVERED *(From – To)*
31-08-2009	Final Report	15 December 2007 - 02-Feb-10

4. TITLE AND SUBTITLE

Unsteady Aerodynamics and Aeroelasticity Calculations of Flapping Motion for Micro Air Vehicle Applications

5a. CONTRACT NUMBER
FA8655-08-1-3015

5b. GRANT NUMBER

5c. PROGRAM ELEMENT NUMBER

6. AUTHOR(S)

Dr. Dilek Funda Kurtulus

5d. PROJECT NUMBER

5d. TASK NUMBER

5e. WORK UNIT NUMBER

7. PERFORMING ORGANIZATION NAME(S) AND ADDRESS(ES)

Middle East Technical University
Middle East Technical University
Ankara 06531
Turkey

8. PERFORMING ORGANIZATION REPORT NUMBER

N/A

9. SPONSORING/MONITORING AGENCY NAME(S) AND ADDRESS(ES)

EOARD
Unit 4515 BOX 14
APO AE 09421

10. SPONSOR/MONITOR'S ACRONYM(S)

11. SPONSOR/MONITOR'S REPORT NUMBER(S)
Grant 08-3015

12. DISTRIBUTION/AVAILABILITY STATEMENT

Approved for public release; distribution is unlimited.

13. SUPPLEMENTARY NOTES

14. ABSTRACT

This report results from a contract tasking Middle East Technical University as follows: The aim of this work is to gain an understanding of the unsteady aerodynamics of flapping motion in order to implement the data obtained to the design of a Micro Air Vehicle. The second task is increase the experimental capability of the existing 2D flapping motion experimental setup to 3D.
The main objective of the previous works was to understand the physics and the aerodynamics of lift generation by flapping motion during hover. The initial phase of the study was limited to 2D analysis where a symmetrical NACA 0012 airfoil is moved upstroke and downstroke with variable speeds. This research will be a continuation of the research work undertaken by D. Funda Kurtulu^{o}, during her Ph.D studies in ENSMA Poitiers France since 2002. With this project it is intended to improve and enhance the experimental studies in 3D.

Two different methods of analysis are used during this study.
1. Numerical methods (DNS and aeroelastic simulations)
2. Experimental techniques

Expected results: The results of the project will be a part of the NATO AVT-149 Technical Team group and will be published in the final report.

Numerical Method:
In numerical analysis, 2D flapping airfoil and 3D flat plate rigid platforms will modelled by Direct Numerical Simulation technique (DNS) using a computer programme, based on an available commercial code Star-CD (or any other 3D unsteady codes that will be decide in NATO AVT 149 technical group) for low and high Re numbers. For the first trials, 3D results will be limited to 1 degree of freedom (rotation). The major aim of flapping motion research is based on the understanding of the relation between the temporal and the spatial changes of the wake structure and the resulting instantaneous aerodynamic forces over the flapping wings. The essential physics of non-steady airfoil problems can be observed from simplified two-dimensional experiments, and the interpretations of the behaviour can be supported by theoretical or numerical models. In addition to the instantaneous aerodynamic forces, pressure distributions and vorticity contours, the average lift and drag coefficient values are also calculated. The 3D platforms (flat plate) will be also investigated with aeroelastic simulations using MSC Nastran program which uses Doublet Lattice Method for aerodynamic analysis and couples with its structural model. The program could handle also gust responses. Some preliminary tests are performed with static analysis.

Experimental Techniques:
The experimental technique is based on the flow visualisation studies of a two-dimensional wing in a water tank, whose motion is controlled

through a computer. The experimental setup used is a 1.5m×1m×1m water tank equipped with a precise traversing system activated by two step motors and computer controlled motion is generated for the displacement of the 2D wing inside the water tank. The command of simultaneous translational and of rotational motions are achieved with the help of these two step motors according to a law with a variable speed. 3D effects could first be visualized by removing one of the end plates of the 2D experimental setup. The second step will be to design a 3D 1degree of freedom (rotation) motion. The objective is the experimental analyses of the vortex dynamics and validation of the numerical simulations with the help of the visualizations by PIV. The real time operation of the system is performed by means of a real time data acquisition and control system which is interfaced to the computer.

Existing facilities in the Department which will be used for the project:

Numerical Codes:

1. Star-CD (2 licenses for whole department)
2. MSC. Nastran, MSC Patran, MSC Flds

Experimental Setup:

1. Water Tank
2. 2D flapping motion setup for hover
3. 3D PIV

One mechanical technician and one electrical technician will be worked for the project for the design and construction of the rotational 3D motion in the water tank. The equipments needed are described below in Cost Estimate Section.

SCHEDULE OF REPORTS/DELIVERIES:

The major stages of the proposed project are:

A. Literature survey (May-June 2007)
B. Numerical Simulations (motion description, grid refinement, parametrical study) (July 2007-May 2008)
C. Establishment of the lab and experimental setup (July 2007-December 2007)
D. Submission of an internal report (December 2007)
E. Experimental results (January 2008-May 2008)
F. Submission of the final report (May 2008)

15. SUBJECT TERMS

EOARD, Aerodyanamics, Micro Air Vehicle, Aeroelasticity

16. SECURITY CLASSIFICATION OF:			**17. LIMITATION OF ABSTRACT**	**18, NUMBER OF PAGES**	**19a. NAME OF RESPONSIBLE PERSON**
a. REPORT	**b. ABSTRACT**	**c. THIS PAGE**			SURYA SURAMPUDI
UNCLAS	UNCLAS	UNCLAS	UL	78	**19b. TELEPHONE NUMBER** *(Include area code)* +44 (0)1895 616021

METU Aerospace Engineering Department

EOARD Report 2

Aerodynamics and Aeroelasticity Calculations of Flapping Motion for Micro Air Vehicle

Assistant Prof. Dr . Dilek Funda Kurtulus
24/08/2009

PROJECT NO	
PROJECT NAME	Aerodynamics and Aeroelasticity Calculations of Flapping Motion for Micro Air Vehicle
ORGANIZATION	METU Aerospace Engineering Department
NAME	Asst. Prof. Dr. Dilek Funda Kurtuluş

Abstract

The numerical and experimental investigations on the characteristics of low Re number regime are increasing due to the advances in micro-technologies enabling the development of Micro Air Vehicles (MAV's). One of the main objectives of MAV applications, i.e. constant position surveillance, reveals the need to focus the researches on hover mode. There are three generations of MAV's namely fixed wings, rotating wings (like helicopters) and wings based on micro technologies (MEMS, flapping or vibrating wings). The definition employed in Defense Advanced Research Projects Agency (DARPA) program limits these crafts to a size less than 15 cm in length, width or height. This physical size puts this class of vehicle at least an order of magnitude smaller than any UAV developed to date.

The studies on flapping motion flight can be classified into two main parts as the zoological configurations and the simplified configurations. The zoological configurations are performed based on the study of insects or birds. Comprehensive reviews of the biological flight mechanisms could be found in Nachtigall (1974); Rayner (1979, 1985); Ellington (1984); Norberg (1985); Azuma et al. (1985); Pennycuick (1988) and Dudley (1998).

The simplified configurations are mostly the works based on the aerodynamics of the flow. The models are simplified such that the real insect/bird wing geometries are replaced with different pre-defined aerodynamic profiles (Shyy et al. 1999; Ramamurti and Sandberg 2002; Platzer and Jones 2006). Although numerical methods are widely used for unsteady aerodynamic problems, it is highly difficult to solve the full 3D Navier–Stokes equations for complex flows like the ones of the flapping insect wings. Hamdani and Sun (2000) simulated a series of impulsive starts at different accelerations around a 2D insect wing. The mean streamwise velocity field of the wake of a NACA 0012 airfoil oscillating in plunge at zero freestream velocity and at a zero angle of incidence at the neutral position was calculated by Lai and Platzer (2001). The vortical flow patterns in the wake of a NACA 0012 airfoil pitching at small amplitudes are studied by Koochesfahani (1989) in a low-speed water

channel by considering the effect of both sinusoidal and non-sinusoidal shape of the waveform. The aeroelastic simulations of the problem are another important concern of the researchers in this domain. Some first simulations with doublet lattice method will be represented for this project.

The objective of the present work could be classified as follows:

1. Numerical simulations

a. 3D Rigid Platform (Flat plate) 1DOF with low Re number simulations (translational impulsive start, rotational impulsive start, parametrical study)

b. 2D Rigid Platform 2DOF high Re number simulations with SD 7003 airfoil

2. Experimental results

a. 3D Platform translational impulsive start, rotational impulsive start visualization in water tank with a parametrical study

b. 3D flapping motion in low Re number (Re<2000) by using existing experimental setup and investigating the 3D effects by removing one of the end plates.

3. The aeroelastic numerical calculations

a. 3D flat plate methods could be calculated with MSC. Nastran aeroelastic module. Conventional MSC.Nastran Structural Model performs Static Analysis and Normal Modes Analysis. MSC.Nastran Aerodynamic Analysis, uses flat plate methods (Doublet Lattice Method). The program maps Aerodynamic Forces to Structure and Maps Structural Deflections to the Aerodynamics

b. Unsteady Gust analysis could be performed with this module to the 3D flat plate

1. Computational Method

The solutions have been performed in two aspects. One is the low Reynolds number laminar solutions of flapping profiles in hover mode and the second part is related to the results of AVT 149 Technical Team pure plunge and pitch/plunge case studies around SD 7003 profile. Additionally different sinusoidal motions at low Reynolds number has also been studied and compared with the experimental data in literature.

The low Reynolds number results for hover mode were given in Report 1 (Appendix A) and they are not repeated in this second report. The additional works carried out from January 2009 are summarized in this Report 2.

1.1 AVT 149 Case studies

(by Erkan Günaydınoglu (M.Sc. student AE METU, Asst. Prof. Dr. D. Funda Kurtulus AE METU)

In this study, the flow structures and the instantaneous forces around SD7003 airfoil undergoing plunging and combined pitching-plunging motions are investigated numerically for different frequencies. The results are a part of the NATO AVT-149 Micro Air Vehicle Unsteady Aerodynamics Task Group work. The resulting flow-fields are visualized in terms of normalized velocity and out-of plane component of vorticity. The two-dimensional solutions agree well with experimental studies. The effect of Reynolds number is also studied for a range of 10,000 to 60,000. It is observed that the combined pitching- plunging is sensitive to the Reynolds number while plunging is independent of Reynolds number in terms of instantaneous forces and flow structures.

INTRODUCTION

It has been more than a century that fluid mechanists are aware of that a sinusoidal plunging airfoil is capable of generating thrust [18, 19]. Recent interests in Micro Aerial Vehicles take into consideration the flapping-wing motion as an alternative propulsion system for which the unsteady low Reynolds number aerodynamics must be studied. One of the diffuculities in flapping-wing studies is the transitional regime for Reynolds numbers because of their limited sizes as 15 cm in height, length or width [13] and the low-speed range. One other difficulty is simulating real bird-insect flight and that complex motion is simplified by using basic models i.e. airfoils-wings in pitch, plunge or ramp motions [7, 8]. Tuncer *et al*. [14, 15] have performed the Navier-Stokes computations to explore the effect of flow separation on the thrust and propulsive efficiency of a single flapping airfoil in combined pitch and plunge motions. It is observed that generated thrust and propulsive efficiency are significantly increased in case of flapping/stationary airfoil combination in tandem. Elredge *et al.* [12] analyzed the pitch plunge motion with a viscous vortex particle method.

Platzer *et al.* [10] emphasizes that most of the studies on flapping wing propulsion analyzed on literature are limited to NACA and elliptical airfoils. The recent studies on flapping motion are tent to study on special low Reynolds number airfoils such as SD7003 that is used in the study. Kang *et a*l [2] investigated a sequence of sinusoidal pitch and plunge motions of SD7003 airfoil computationally and compared the results with two-dimensional particle image velocimetry experiments. The forces are compared with Theodorsen's model and get an agreement for cases where massive separations do not occur. Yuan *et al.* [1] conducted Large-eddy simulations to study plunging and pitching-plunging SD7003 airfoil and compared the results with PIV experiments. Ol *et al.* [2] studied the same motion numerically and the results are compared with PIV experiments in water tunnel in terms of vorticity and velocity. Moreover, dye injection method is used for a wide range of Reynolds number to visualize the flow-field qualitatively. McGowan *et al.* [6] studied sinusoidal pure-pitch and pure-plunge oscillations of SD7003. The PIV experiments are compared with computations with an unsteady RANS solver and Immersed Boundary Method at Reynolds number of 10,000 and 40,000 which are in the transitional region. In their study experimental-computational agreement for plunge is satisfied whereas the for pitch case agreement is not achieved.

The flapping motion study has also been performed experimentally in hover mode by Kurtulus *et al*. [5] and numerically by Akay *et al.* [9]. The prescribed flapping motion has been investigated for different airfoil profiles including NACA 0012 and ellipses with different thicknesses. Particle Image Velocimetry technique has been used to obtain the flow-field around the NACA0012 airfoil in hover mode at Re=1000 and the results are compared with numerical solutions by Kurtulus *et al.* [5].

In this study, the unsteady aerodynamics of SD7003 airfoil undergoing sinusoidal plunging and combined pitching-plunging motions is investigated at Reynolds number range of 10,000 to 60,000 for reduced frequencies of 0.25 and 3.93. The numerical solution is compared with the experimental data of US Air Force Research Laboratory (AFRL) and TU Braunschweig [2, 8] and numerical solutions agree with experimental data in terms of flow structures and instantaneous aerodynamic forces.

METHOD

Kinematics

Pure plunge and combined pitch-plunge motions are studied for two different reduced frequencies. The motions studied are the case studies of NATO AVT 149 Micro Air Vehicle Unsteady Aerodynamics Task Group .The equations of motion of flapping motion is given in equation (1)

$$\theta(t) = A\cos\left(\omega t + \frac{\pi}{2}\right) + \alpha_0 \qquad (1)$$

$$h(t) = h_0 c\cos(\omega t)$$

where $h(t)$ is the plunge position of the airfoil with time and $\theta(t)$ is the pitch angle variation with respect to the pivot point. The parameters for four flapping motion is given in Table (1) where k is the reduced frequency, $k = \omega c/2U_\infty$, α_0 is the mean angle of attack, h_0 is non-dimensional plunging amplitude and A is the pitch amplitude in degrees.

Table 1 Parameters used to define flapping kinematics

Cases investigated	**k**	α_0	h_0	**A**	Re range
Pure-plunge	0.25	8	0.5	0	10k, 30k, 60k
Pitch-plunge	0.25	8	0.5	8.43	10k, 30k, 60k
Pure-plunge	3.93	4	0.05	0	60k
Pitch-plunge	3.93	4	0.05	8.43	60k

The plunging and pitching motion of the airfoil results in an instantaneous effective angle of attack. Instantaneous effective angle of attack for flapping motion is defined by equation (2)

$$\alpha_{eff} = \alpha - \arctan\left(\frac{\dot{h}(t) + \frac{1}{4}c\dot{\alpha}(t)\cos(\alpha(t))}{U_\infty - \frac{1}{4}c\dot{\alpha}(t)\sin(\alpha(t))}\right) \qquad (2)$$

The geometric and effective angle of attack variations of the airfoil during both motions can be observed in Figure 1. The red line denotes the effective angle of attack for pure-plunge motion. For pure plunge motion, the plunge induced velocity and the free-stream velocity are used to define the effective angle of attack. The blue line in Figure 1 denotes effective angle of attack with respect to pivot point for pitch-plunge motion. The black line, for which a time-shift is observed for both motions, is the effective angle of attack for pitch-plunge motions with respect to the leading edge of the airfoil. In this last case, the angular speed also induces an instantaneous velocity normal to the chord direction at the leading edge of the airfoil.

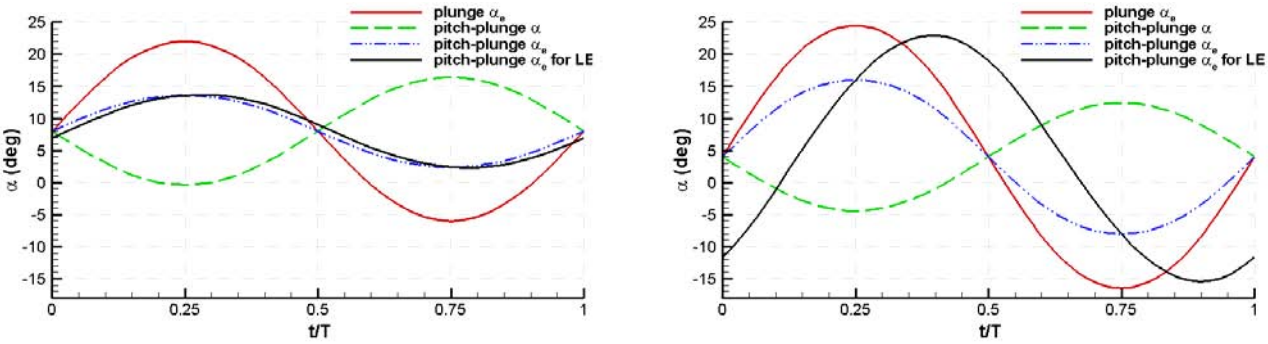

Figure 1 *The instantaneous geometric and effective angle of attacks for k=0.25, h=0.5, theta=8 cases (left) and k=3.93, h=0.05, theta=4 cases (right)*

Grid Generation

In all cases unstructured O type grid with outer diameter of 60c around the SD7003 airfoil is used. The y^+ value for both cases is chosen as less than 1. Figure 2 shows the whole domain and the grid around the airfoil. A grid refinement process is conducted to have grid-independent solution. The previous studies showed that a grid with 92358 cells is enough to have the grid-independent solution [3]. Moreover, 960 steps per period are chosen for time step.

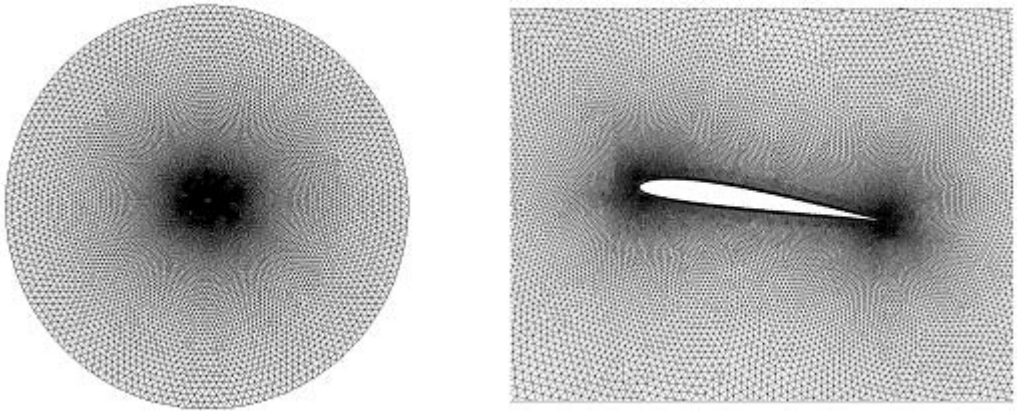

Figure 2 ***Unstructured grid distribution around SD 7003 airfoil***

Solver Description

The numerical simulation of flapping motion is performed by commercially available CFD code Fluent in which unsteady, pressure based Reynolds-Averaged Navier-Stokes solver with second order upwind spatial discretization is used. The pressure-velocity coupling is handled by SIMPLE algorithm [17]. The flapping motion of the airfoil and the wing is implemented into the code by using 'dynamic mesh' feature of Fluent [11]. To model the motion, the whole grid is divided into two parts: inner grid with 20c diameter and outer grid with 60c diameter. In solution process, the inner grid around the airfoil performs the prescribed motion while the outer grid is stationary and deforming with appropriate rules. The dynamic mesh feature of the code limits the unsteady formulation to the first order in time and so for all calculations first-order temporal discretization is used. The far boundary conditions are set as velocity inlet and pressure outlet. The free-stream flow is assumed to be turbulent and Menter's Shear Stress Transport model is used for turbulence closure, which is a favorable model in prediction of adverse pressure gradients [16].

RESULTS

Pitch-plunge case

Figure 3 represents the u-velocity component of pitch-plunge with a reduced frequency of k=0.25 and Re=60,000. The results are represented for different phases. The left column represents the numerical solutions of the present study. The results are compared with the TU Braunschweig PIV solutions (middle column) and AFRL solutions (right column). The PIV solutions of TU Braunschweig is taken very close to the SD 7003 profile, in order to visualize the transition location of the airfoil from laminar to turbulent flow with 11 different PIV windows close to the upper surface of airfoil. The numerical results seem to be closer to their results close to the profile.

Figure 4 shows the non-dimensional vorticity contours for pitch/plunge case. At t/T=0, the instantaneous angle of attack is 8°. The numerical results are very close to the both of the experimental simulations at that instant. At t/T=0.25, the angle of attack reduces close to zero, however the effective angle of attack is observed to be 13.6°. From velocity and vorticity contours, the numerical results reveal a separation at this time instant at the leading edge of the airfoil. Similar behavior is observed at the experimental study in the second column of Figure 3 and Figure 4. At t/T=0.5, the angle of attack once more increase to 8°, for which the effective angle of attack is 9^{o}. A trailing edge vortex is observed at this time instant. The leading edge vortex is separated from the upper surface of the airfoil. At t/T=0.75, the geometric angle of attack increases to 16.43° which is the maximum angle reached for this prescribed motion. However, the effective angle of attack at this time instant is close to 2.4° so that we observe an attached flow close to the leading edge of the airfoil at this time instant.

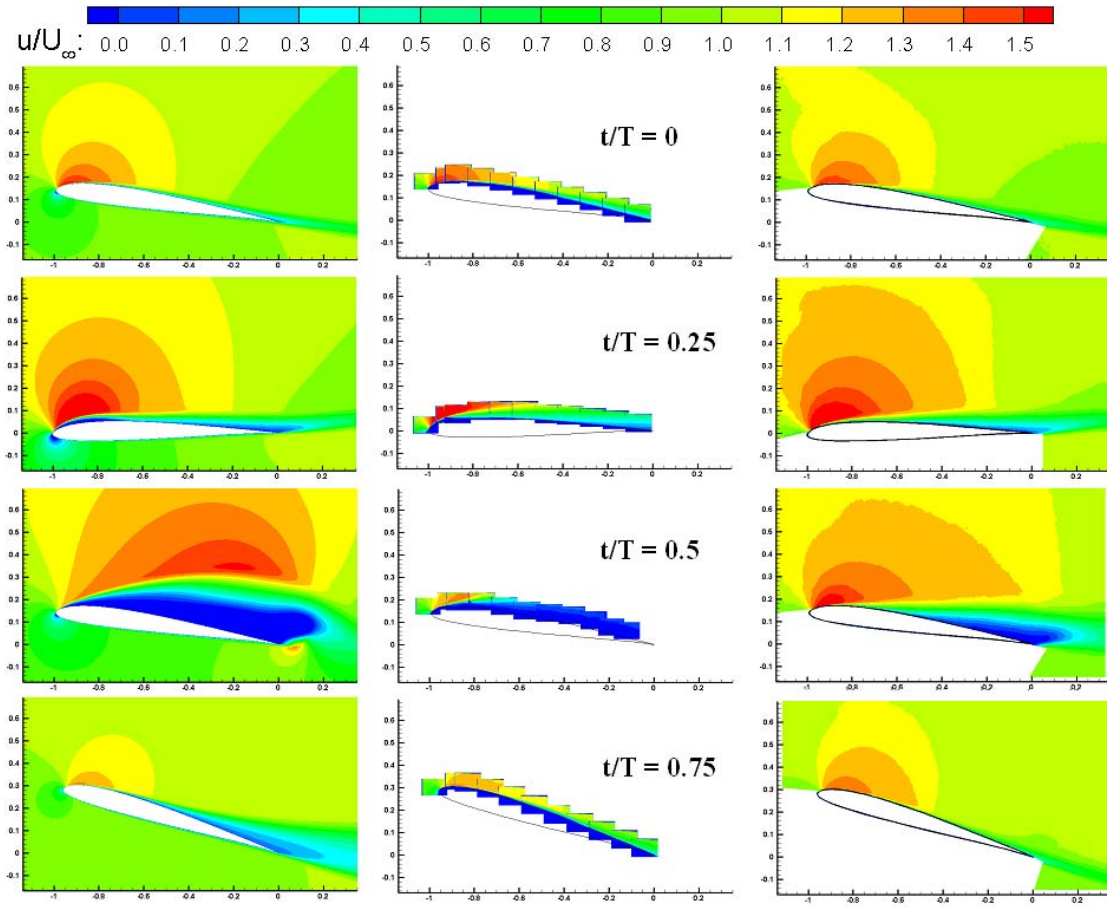

Figure 3 ***Normalized u-velocity contours from computation (left column), experiment of TU Braunschweig (middle column) and experiment of AFRL [2] (right) for pitch/plunge, Re=60,000, k=0.25***

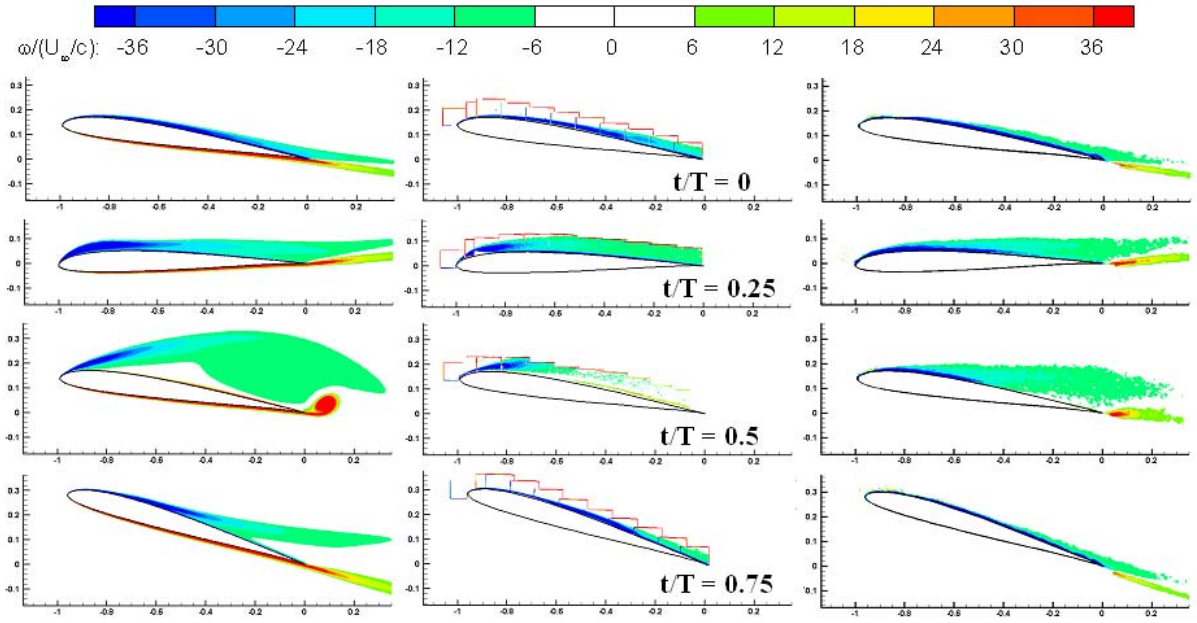

Figure 4 ***Normalized out-of-plane vorticity contours from computation (left column), experiment of TU Braunschweig (middle column) and experiment of AFRL [2] (right column) for pitch/plunge, Re=60,000, k=0.25***

Pure-plunge case

Figure 5 represents the u-velocity component of the pure plunge motion at k=0.25 and Re=60,000. For pure plunge motion, the angle of attack is 8° however the effective angle of attack changes as in Figure 1 (left column). The results are represented at different phases of the motion and they are compared with the experimental and numerical solutions of Ol *et al* [2]. Pure plunge case represents very good agreement with the experimental data. The beginning of the motion at t=t/T=0 is very close to PIV results of Ol *et al.[*2] where the effective angle of attack is equal to 8°. At t/T=0.25, the effective angle of attack increases to high values on the order of 22°. This results a massive detachment from the airfoil upper surface. U-velocity component at this time instant seems to be in very good agreement with experimental solutions. Figure 6 represents contours of normalized out-of-plane component of vorticity for pure plunge case. At t/T=0.25, a counter-clockwise vortex grows at the upper surface of the airfoil, which results the detachment of the clockwise leading edge vortex from the airfoil surface. At t/T=0.417, a trailing edge vortex in counter-clockwise direction grows, and this vortex detaches from the airfoil surface very quickly. The trace of the detached vortex could be observed in Figure 6 at t/T=0.5. Similar trailing edge vortex structure is also observed from the PIV measurements of Ol *et al.* [2].

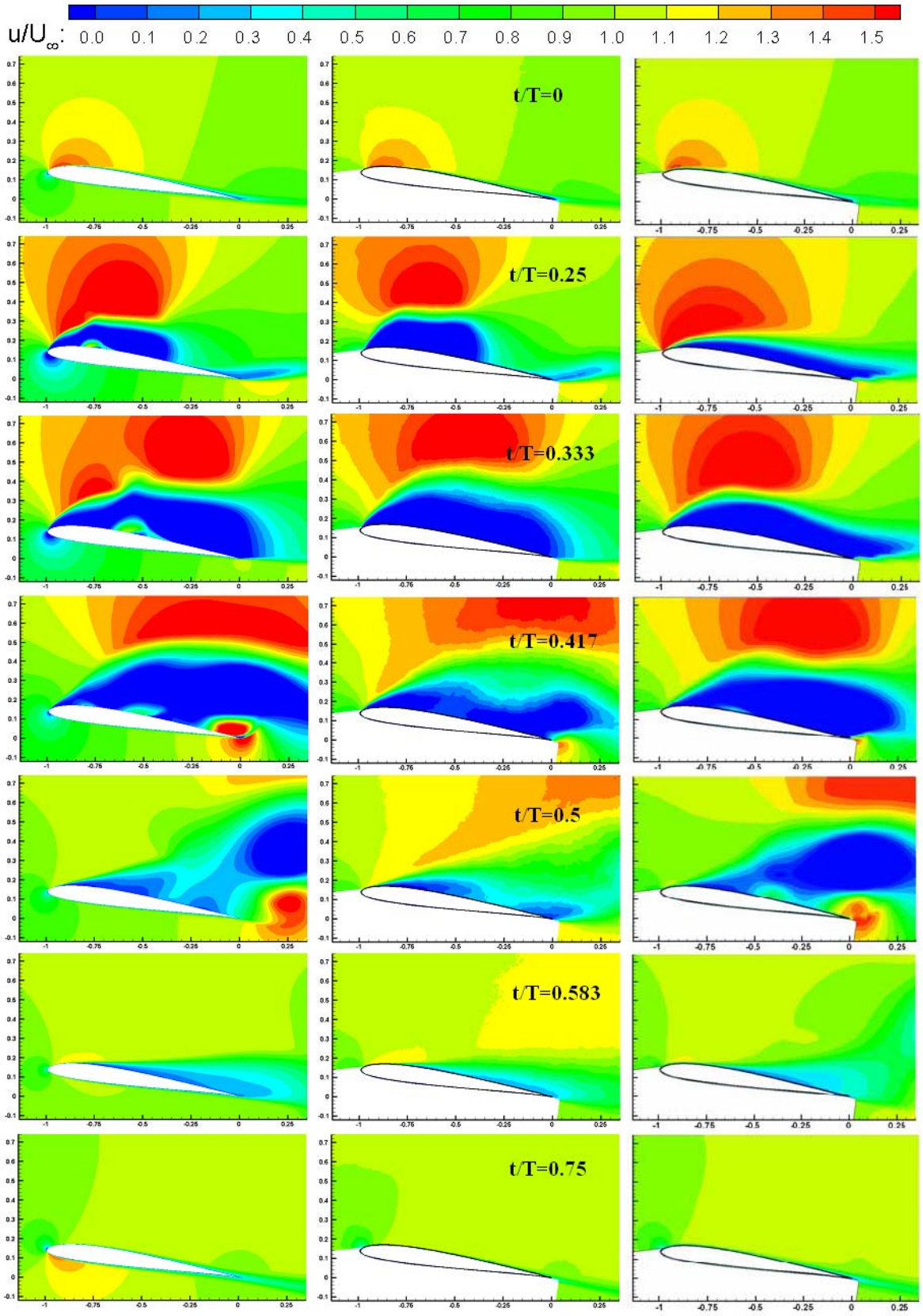

Figure 5 ***Normalized u-velocity contours from present computation (left column), experiment of AFRL [2] (middle column) and numerical study of Ol et al. [2] (right column) for pure plunge, Re=60,000 k=0.25***

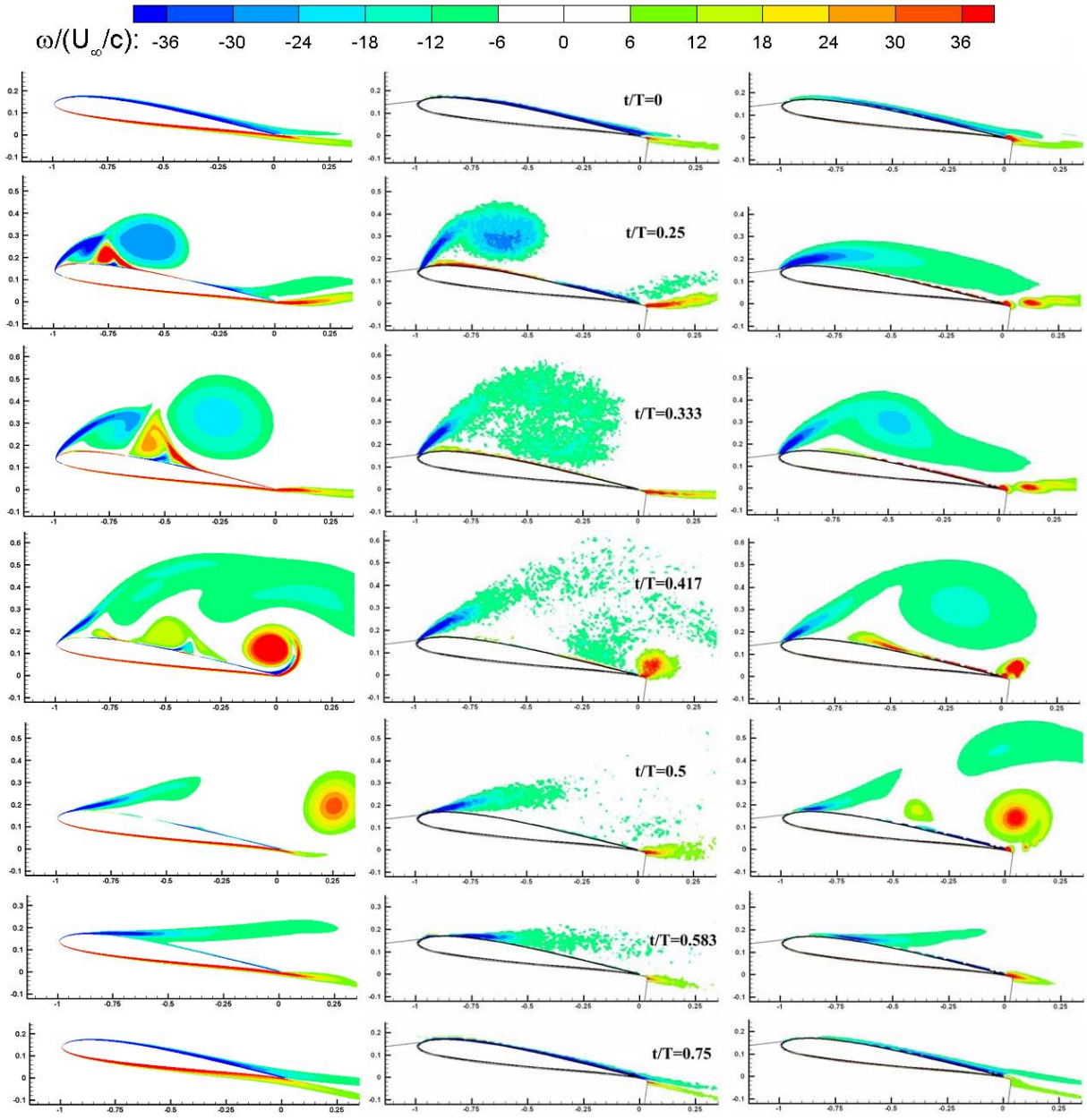

Figure 6 ***Normalized out-of-plane component of vorticity contours from present computation (left column), experiment of AFRL [2] (middle column) and numerical study of Ol et al. [2] (right column) for pure plunge, Re= 60,000, k=0.25***

Reynolds Number Effect

Figure 7 compares the u-velocity components for pitch-plunge case at k=0.25 for different Reynolds numbers of 10k, 30k and 60k. Figure 8 shows the contours of normalized out-of-plane component of

vorticity for similar cases. At Re=10,000, a counter-clockwise vortex is observed at the mid-location of the upper surface of the airfoil, which pushed the leading edge vortex towards up and causes it to detach from the airfoil surface. At t/T=0.333, when in the same time as this upper surface vortex structure, the trailing edge vortex in counter-clockwise direction also grows for Re=10,000 case (Figure 8). The formation of trailing edge vortex is observed at t/T=0.417 for Re=30,000 and at t/T=0.5 for Re=60,000.

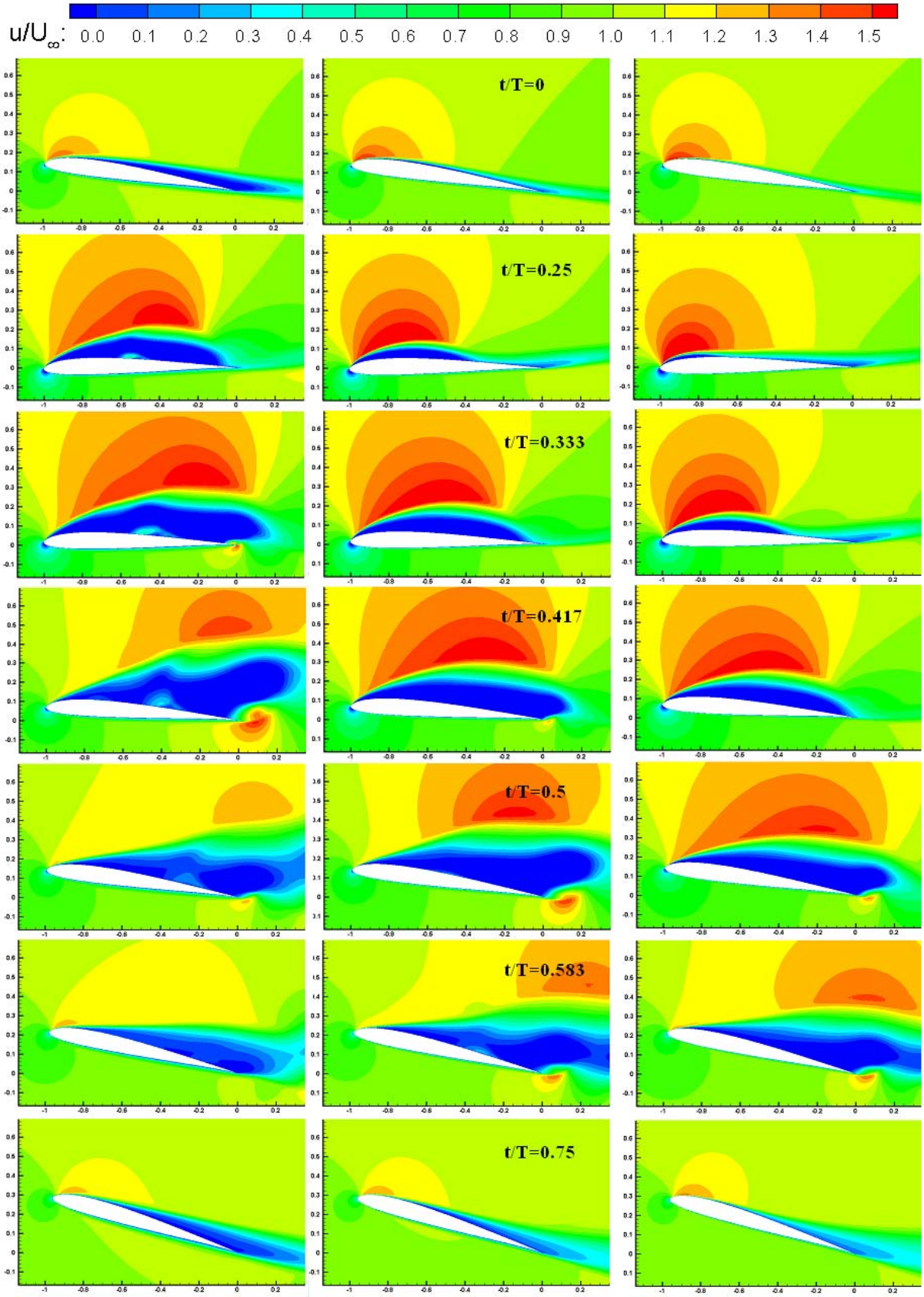

Figure 7 ***Normalized u-velocity contours for pitch-plunge at Re=10,000 (left column), Re=30,000 (middle column) and Re= 60,000 (right column), k=0.25***

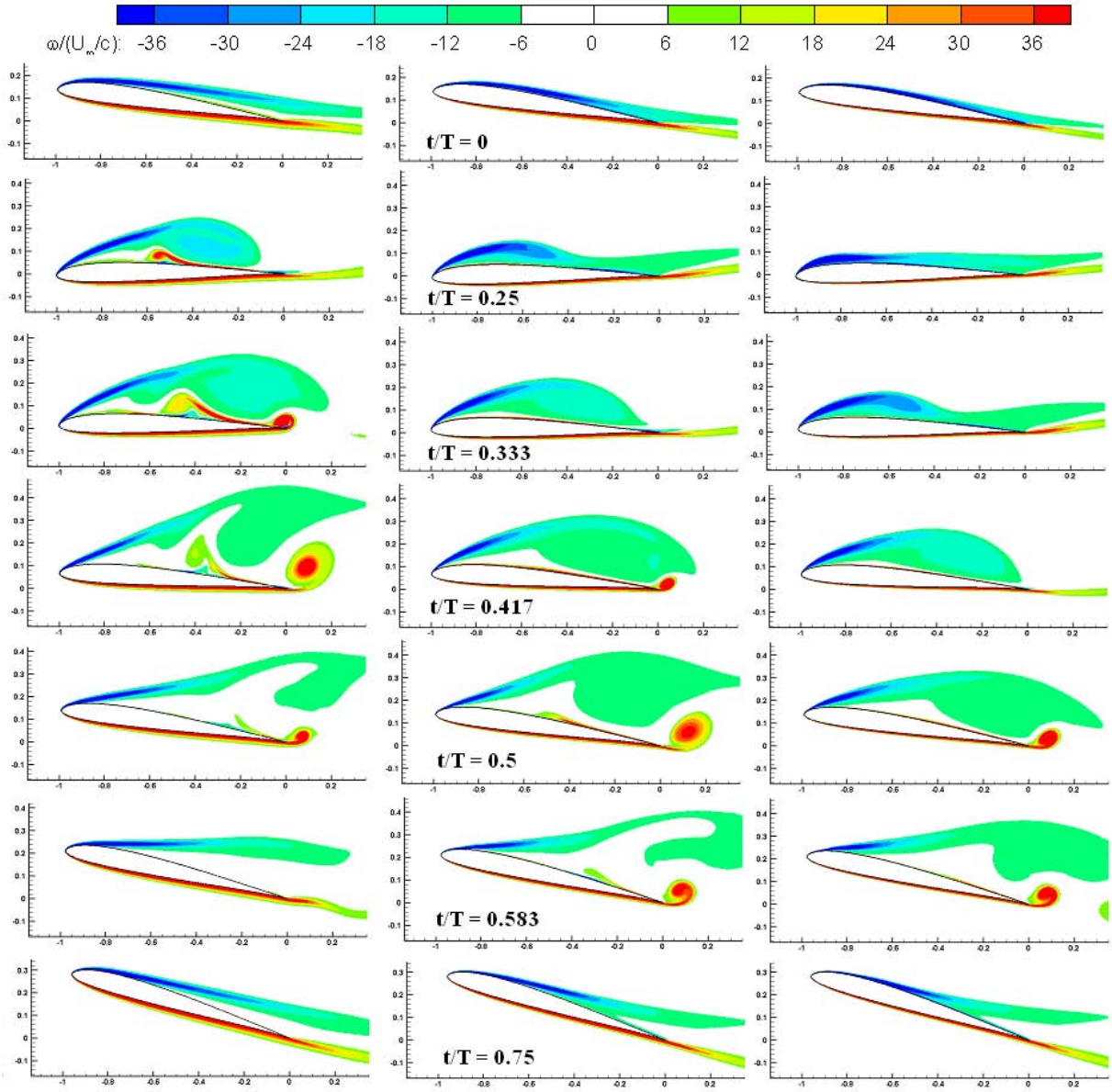

Figure 8 ***Contours of normalized out-of-plane component of vorticity for pitch-plunge at Re=10,000 (left column), Re=30,000 (middle column) and Re= 60,000 (right column), k=0.25***

The pure plunge case with k=0.25 is also solved for Re= 10,000; 30,000 and 60,000. The u-velocity contours for all Reynolds number variants are given in Figure 9 and Figure 10 represents the vorticity contours for the same time instances of Figure 9. The leading edge vortex structures are much more dominant for lower Reynolds number case (Re=10,000). As Reynolds number increases, the position of the counter-rotating vortex on the upper surface of the airfoil shifts towards the leading edge of the airfoil (see t/T=0.25 in Figure 9). At t/T=0.417, the core of the trailing edge

vortex is observed to be more far away from the airfoil surface for Re=10,000 case. As the Reynolds number increases, the trailing edge vortex becomes closer to the trailing edge of the airfoil.

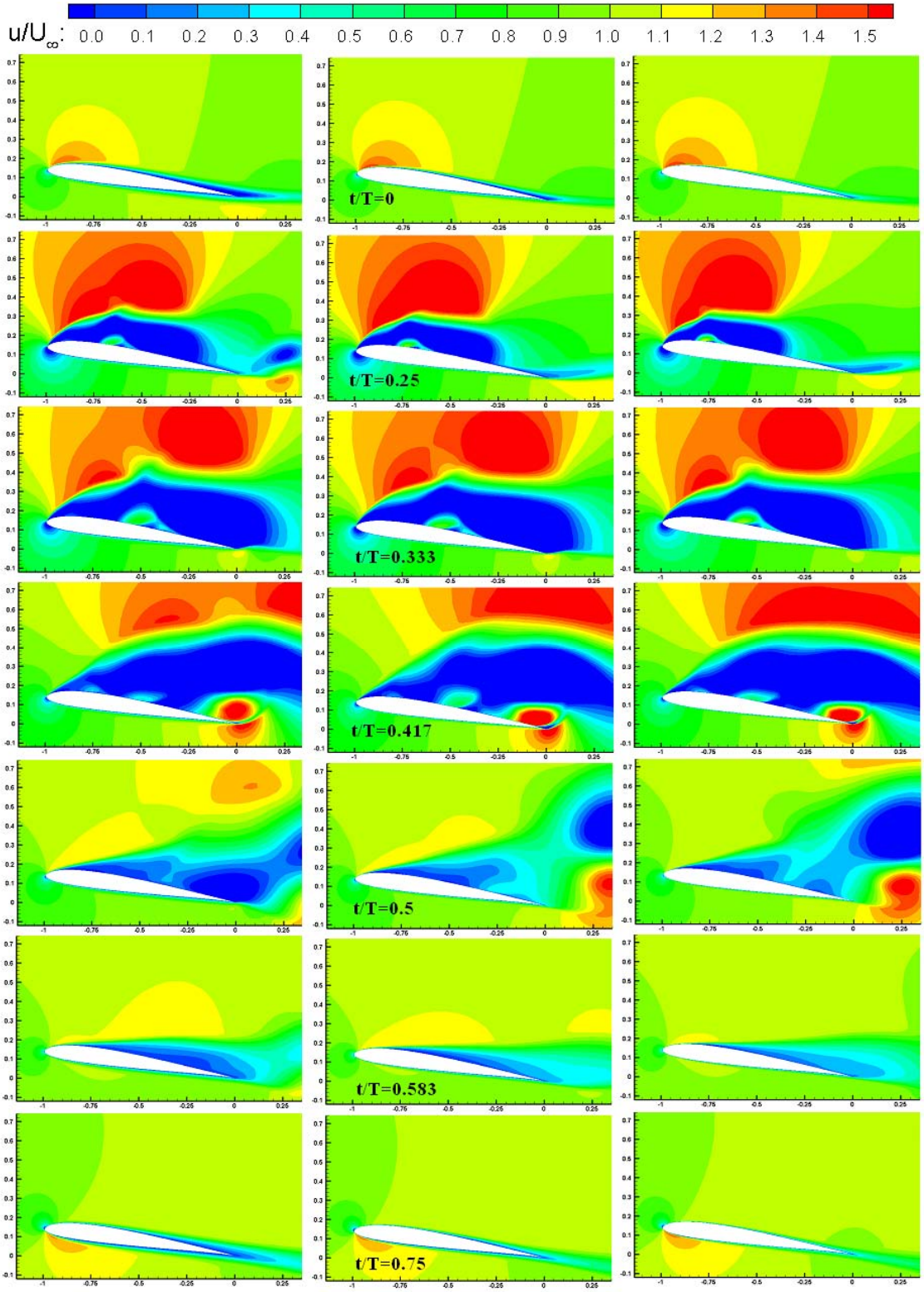

Figure 9 ***Normalized u-velocity contours for pure-plunge at Re=10,000 (left column), Re=30,000 (middle column) and Re= 60,000 (right column), k=0.25***

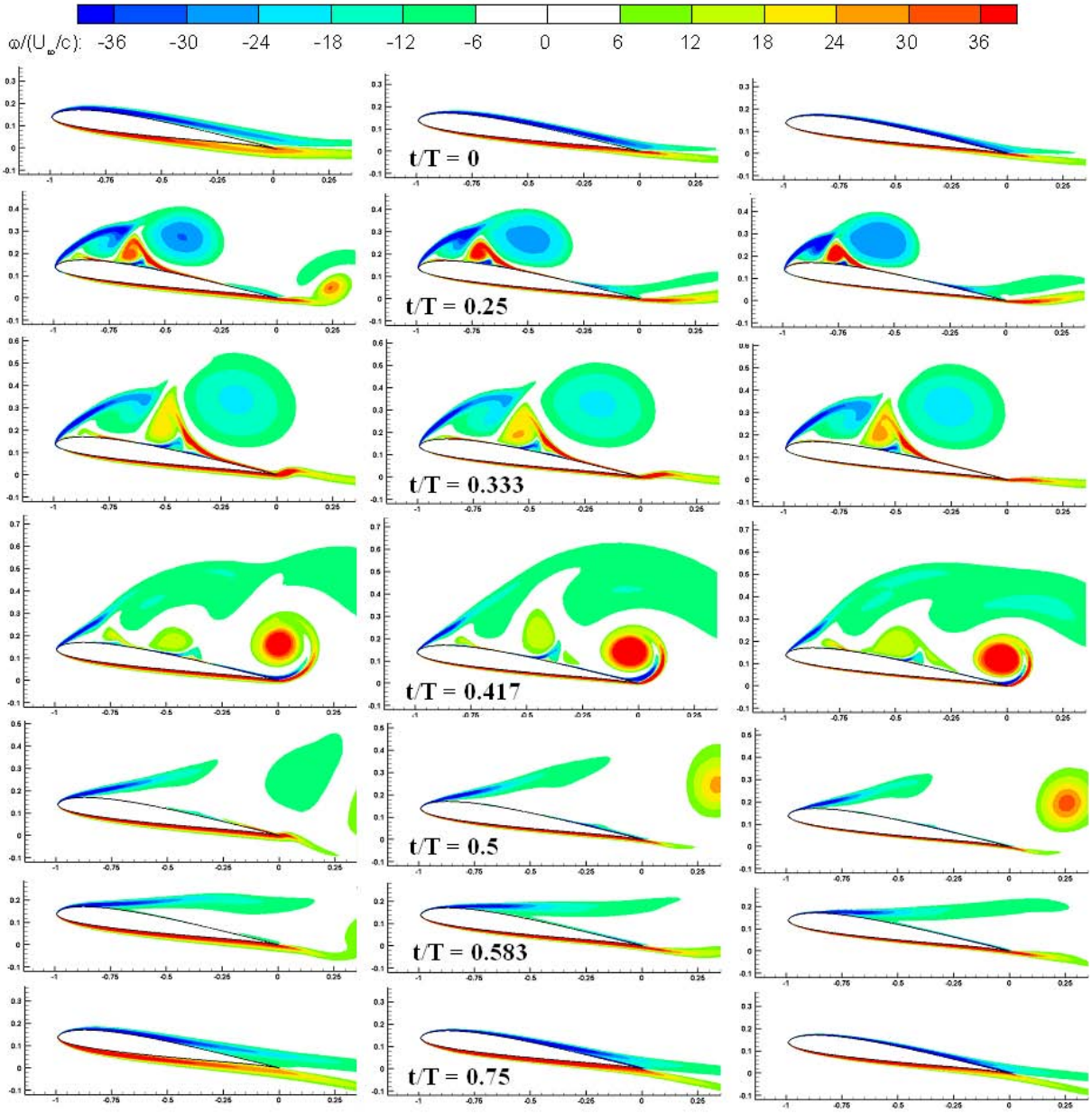

Figure 10 ***Contours of normalized out-of-plane component of vorticity for pure-plunge at Re=10,000 (left column), Re=30,000 (middle column) and Re= 60,000 (right column), k=0.25***

Figure 11 represents the aerodynamic force coefficients for pure plunge and pitch/plunge cases at different Reynolds numbers for k=0.25. The effect of Reynolds number is not abrupt for pure plunge case (right column of Figure 11). However, the peak location of the pitch/plunge case is found to shift as the Reynolds number increases. A similar behavior is observed after t/T=0.6 for Re=30,000

and 60,000. Positive lift coefficient values are obtained during the whole period of pitch/plunge motion.

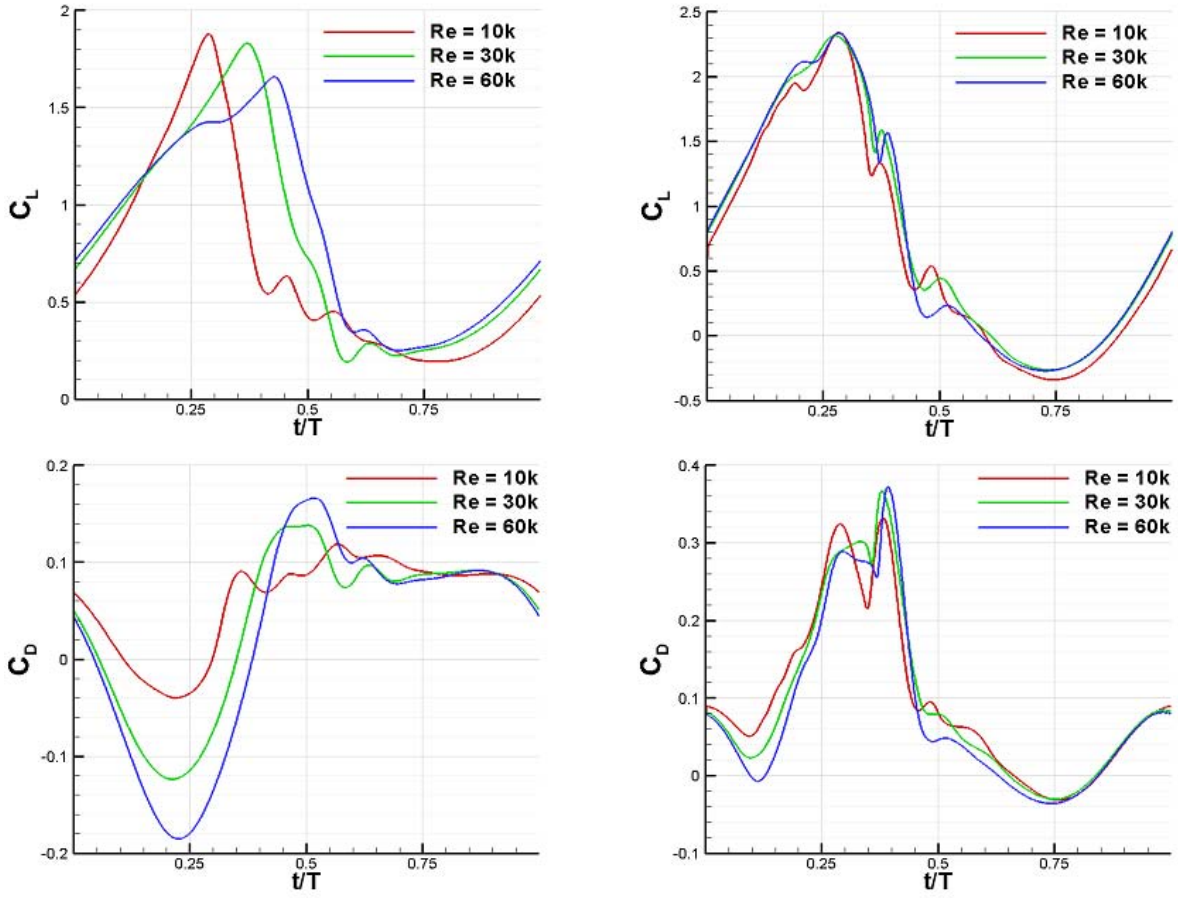

Figure 11 ***Computed force coefficients for different Reynolds numbers, pitch-plunge case (left column) and pure plunge case (right column), k=0.25***

High Reduced Frequency Cases

The results are also obtained for a higher value of reduced frequency which is equal to 3.93 for pure plunge and pitch/plunge cases. Figure 12 shows the u-velocity component of pure plunge case at k=3.93 and Re=60000. The results are also compared with the PIV solutions of Ol et al. [8]. The solutions at 4 different phases of the motion are represented in Figure 12 and the results are in good agreement with experimental data. Similar vortex structures are observed in numerical solutions of

present study and experimental solutions of Ol et al. [8] which could be observed from the vorticity contours in Figure 13. Figure 14 shows the instantaneous u-velocity components of pitch/plunge case at k=3.93 and Re=60000. As the reduced frequency increases, the vortex structures detach from the trailing edge of the airfoil and seem to be attached on the upper surface of the airfoil during the pitch/plunge case. A Karman-vortex street is obtained from the detached vortex structure from the trailing edge of the airfoil. At t=0, a clockwise trailing edge vortex is observed which detaches from the airfoil surface very quickly and leaving its place to a counter-clockwise trailing edge vortex at t/T=0.25 (Figure 15). This vortex grows until t/T=0.75 and detaches from the airfoil surface. A new clockwise trailing edge vortex grows after that instant. During the whole period, the flow is found to be attached to the airfoil upper and lower surfaces. No leading edge vortex is observed for this case.

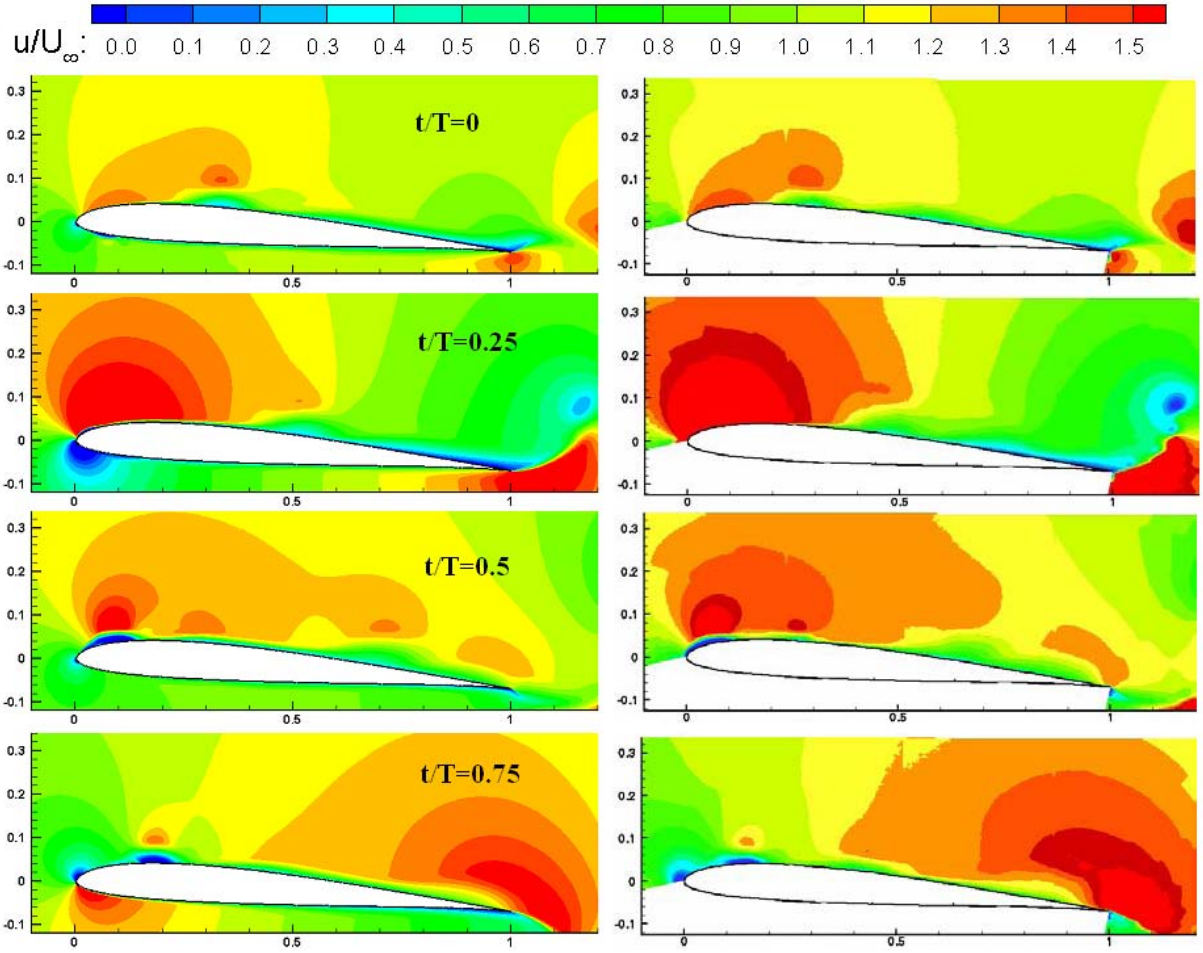

Figure 12 ***Contours of normalized u-velocity for pure-plunge from computation (left column) and experiment of Ol [8] (right column) k=3.93***

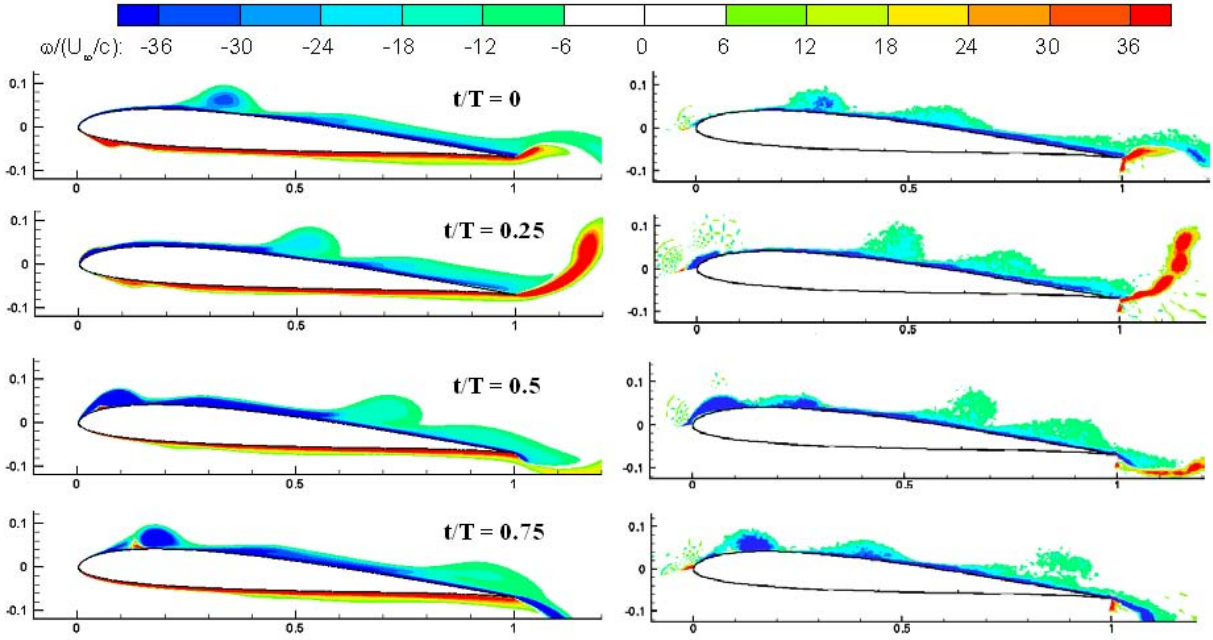

Figure 13 ***Contours of normalized out-of-plane component of vorticity for pure-plunge from computation (left column) and experiment of Ol [8] (right column) k=3.93***

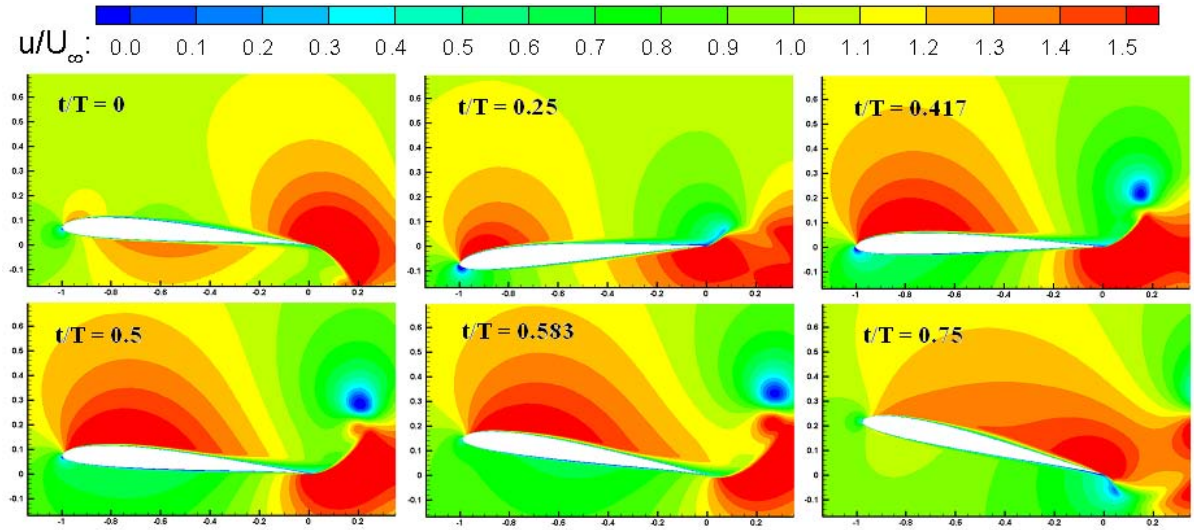

Figure 14 ***Contours of normalized u-velocity for pitch-plunge from computation, Re=60,000 and k=3.93***

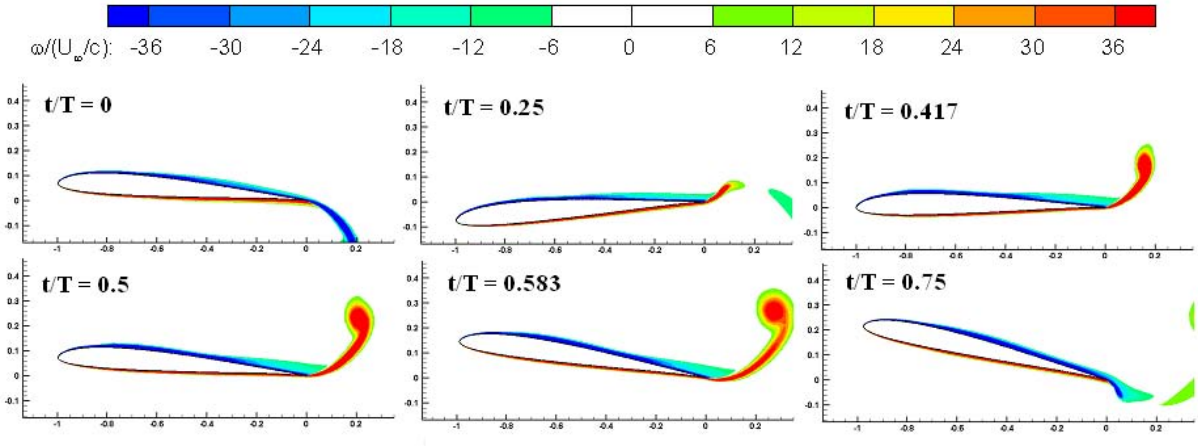

Figure 15 ***Contours of normalized out-of-plane component of vorticity for pitch-plunge from computation, Re=60,000 and k=3.93***

Figure 16 shows the instantaneous lift and drag coefficients for pure plunge and pitch/plunge cases at k=3.93 and Re=60,000. The maximum of the lift coefficient is found to be very high compared to low reduced frequency case. Negative drag coefficient values are observed for pitch/plunge case during the whole period that will result a mean drag coefficient of -0.2677 as shown in Table 2

Table 2 *Computed mean force coefficients for investigated cases*

Cases investigated	Mean C_L	Mean C_D
Pitch-plunge Re=60k k=0.25	0.856	0.0224
Pitch-plunge Re=30k k=0.25	0.802	0.0376
Pitch-plunge Re=10k k=0.25	0.683	0.0609
Pure-plunge Re=60k k=0.25	0.766	0.0805
Pure-plunge Re=30k k=0.25	0.779	0.0931
Pure-plunge Re=10k k=0.25	0.682	0.0956
Pitch-plunge Re=60k k=3.93	0.838	-0.2677
Pure-plunge Re=60k k=3.93	0.703	-0.0664

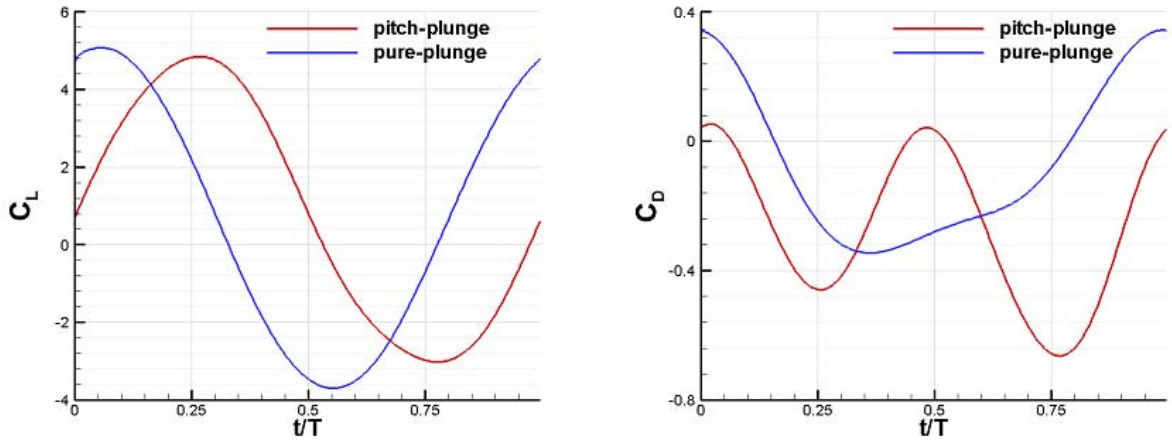

Figure 16 ***Computed force coefficients for high frequency case, Re=60,000 and k=3.93***

The pitch plunge and pure plunge motions are also investigated with a flat plate having 2.5% thickness. The normalized u-velocity component and vorticity contours at different phases of the pitch/plunge motion are given in Figure 17 at Re=60000. Figure 18 shows the normalized u-velocity contours and vorticity contours for pure plunge case at different phases of the motion.

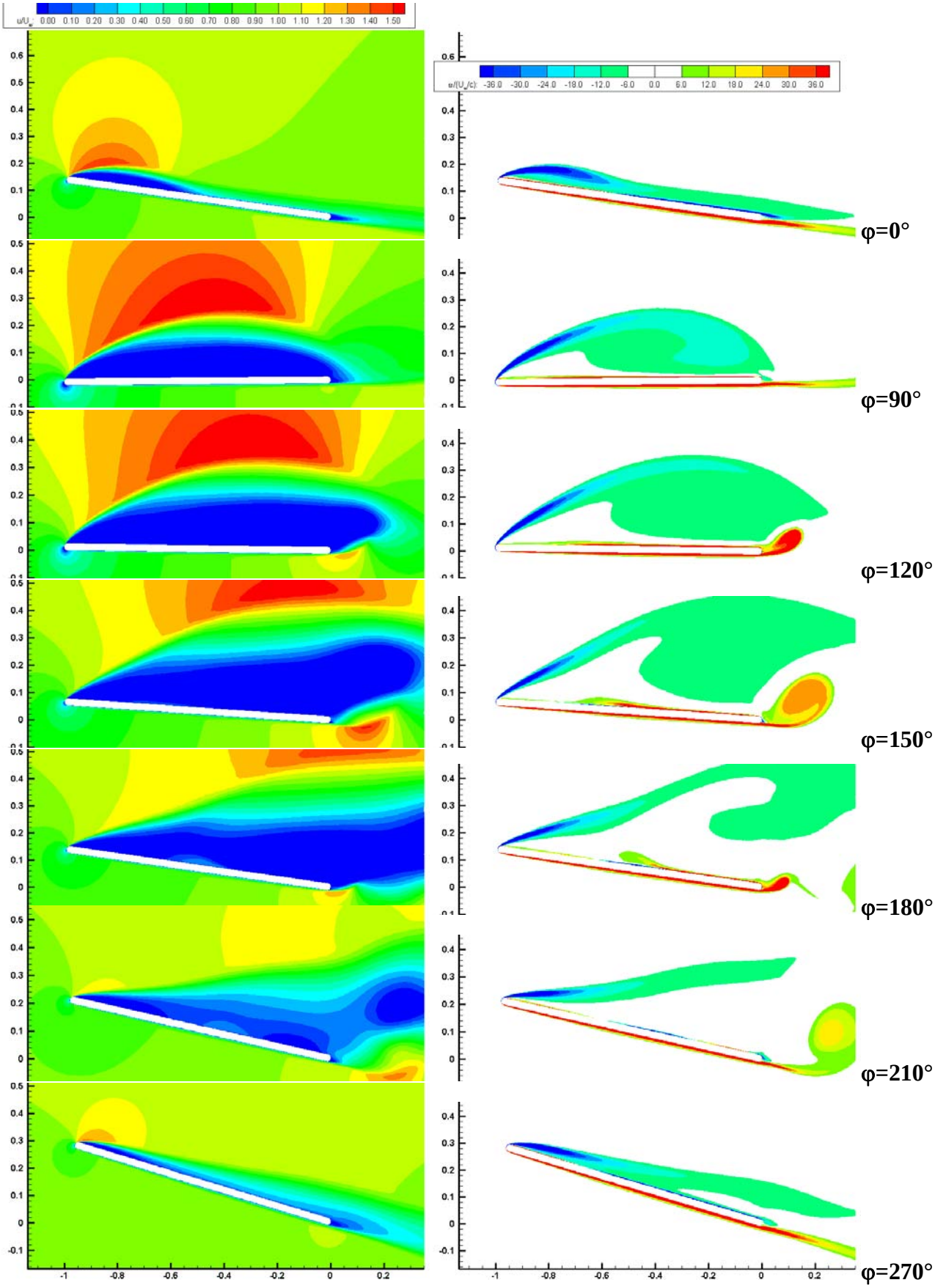

Figure 17 Contours of normalized u-velocity(left) and vorticity (right) for pitch/plunge motion of a flat plate with 2.5% thickness

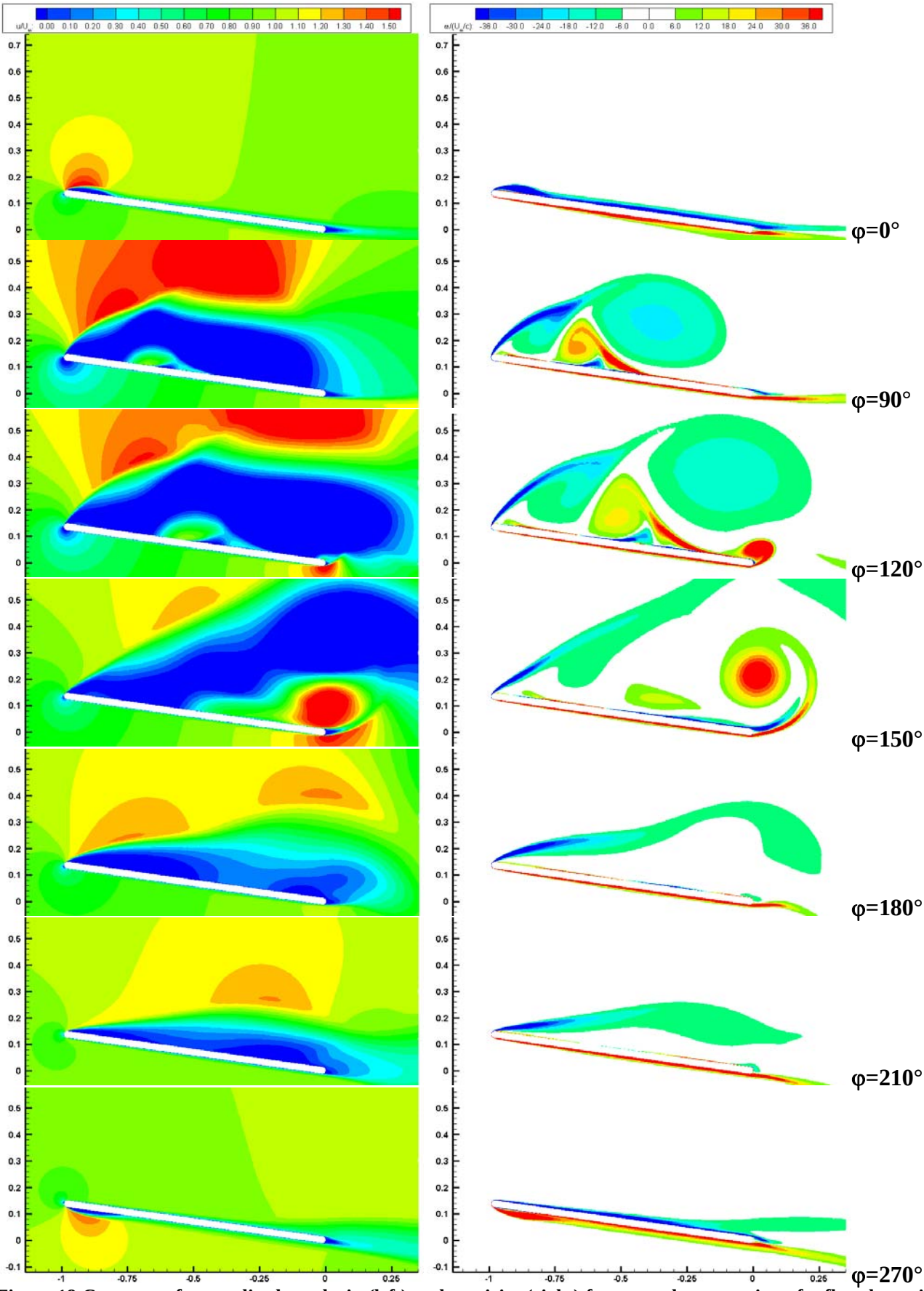

Figure 18 Contours of normalized u-velocity(left) and vorticity (right) for pure plunge motion of a flat plate with 2.5% thickness

CONCLUSIONS

The pitch plunge and pure plunge cases at different reduced frequencies are investigated during this study. The results are compared with the experimental solutions available in literature. The solutions are part of the AVT-149 technical team work.

Acknowledgements

This work is supported by EOARD Grant No: 073007. Dr. Kurtulus thanks support by EOARD, AFRL (USA). The authors acknowledges also the support by TUBITAK and TUBITAK 105M230 project.

References

[1] Yuan, W., and Khalid, M., *Flow Analysis of a Flapping SD7003 Airfoil at Transitional Reynolds Numbers*, 27th AIAA Applied Aerodynamics Conference, San Antonio, Texas, AIAA 2009-3955, June 2009

[2] Ol, M.V., Bernal, L., Kang, C.K., Shyy, Wei., *Shallow and Deep Dynamic Stall for Flapping Low Reynolds Number Airfoils*, Experiments in Fluids, Vol. 46, 883-901, April 2009

[3] Gunaydinoglu, E., and Kurtulus, D.F., *Numerical Investigation of Pure Plunge and Pitch/Plunge Motions at Low Reynolds Numbers*, International Symposium of Light-Weight Unmanned Aerial Vehicle Systems and Subsystems, Ostend, Belgium, March 2009

[4] Kang, C.K., Baik, Y.S., Bernal, L., Ol, M.V., and Shyy, W., *Fluid Dynamics of Pitching and Plunging Airfoils of Reynolds Number between 1×10^4 and 6×10^4*, 47th AIAA Aerospace Sciences Meeting Including The New Horizons Forum and Aerospace Exposition, Orlando, Florida, AIAA 2009-536, January 2009.

[5] Kurtulus D.F., David, L., Farcy A., Alemdaroglu N., *Aerodynamic characteristics of flapping motion in hover*, Experiments in Fluids, Vol.44, pp. 23-36, 2008

[6] McGowan G.Z., Gopalarathnam A., Ol M.V., Edwards, J.R., Fredberg D.,Computation vs. Experiment for High-Frequency Low-Reynolds Number Airfoil Pitch and Plunge, 7 - 10 January 2008, 46th AIAA Aerospace Sciences Meeting and Exhibit, Reno, Nevada, 2008

[7] Ashraf, M. A., Lai, J. C. S., Young, J., *Numerical Analysis of Flapping Wing Aerodynamics*, 16th Australasian Fluid Mechanics Conference (AFMC), Gold Coast, Queensland, Australia, 2-7 December 2007

[8] OL, M. V., *Vortical Structures in High Frequency Pitch and Plunge at Low Reynolds Number*, 37th AIAA Fluid Dynamics Conference and Exhibit, 25 - 28 June 2007, Miami, FL, AIAA 2007-423, 2007

[9] Akay, B., Kurtulus D.F., Alemdaroglu N., *Unsteady Aerodynamic of Different Wing Profiles at Low Reynolds Number*, NATO AVT-146, Platform Innovations and System Integration for Unmanned Air, Land and Sea Vehicles, 14-17 May 2007.

[10] Platzer M.F., Jones K.D., *Flapping Wing Aerodynamics – Progress and Challenges*, 44th AIAA Aerospace Sciences Meeting and Exhibit, 9 - 12 January 2006, Reno, Nevada, AIAA 2006-500, 2006

[11] Fluent v.6.3 User's Guide, 2006

[12] Elredge, J.D., *Efficient Tools for the Simulation of Flapping Wing Flows*, 43rd Aerospace Meeting, Reno, NV., AIAA 2005-0085, January 10-13 2005

[13] McMichael, J.M. and Francis, M.S., *Micro Air Vehicles - Toward a New Dimension in Flight*, DARPA, USA. 1997.

[14] Tuncer, I.H., Lai J., Ortiz, M.A., and Platzer, M.F., *Unsteady Aerodynamics of Stationary/Flapping Airfoil Combination in Tandem*, AIAA Paper 97-0659

[15] Tuncer, I.H., Platzer, M.F., *Thrust Generation due to Airfoil Flapping*, AIAA Journal Vol. 34, No. 2, pp. 324-331, December 1995,

[16] Menter, F.R.,*Two-Equation Eddy-Viscosity Turbulence Models for Engineering Applications*,AIAA Journal, Vol. 32, No. 8, pp. 1598-1605, August 1994

[17] Patankar, S. V., *Numerical Heat Transfer and Fluid Flow*, Hemisphere Publishing Corporation, Washington NewYork London, 1980.

[18] Betz, A., *Ein beitrag zur Erklärung des Segelfluges*, Zeritschrift für Flugtechnik und Motorluftschiffahrt, Vol. 3, pp. 269-272, January 1912

[19] Knoller,R.,*Die Gesetze des Luftwiderstandes*, Flug- und Motortechnik (Wien), Vol. 3, No.21,pp.1- 7, 1909

1.2 Steady state computations of SD 7003 and flat plate with 3.5% thickness

a) Steady state solution around SD 7003 at Re= 60000

Figure 17 and Figure 18 show the grid used for the stead state solution around SD 7003 airfoil.

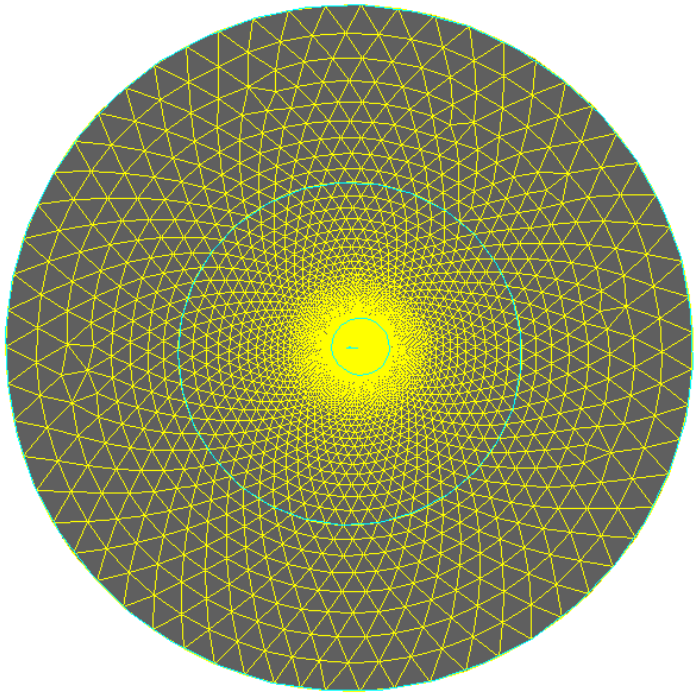

Figure 19 Unstructured grid around SD 7003

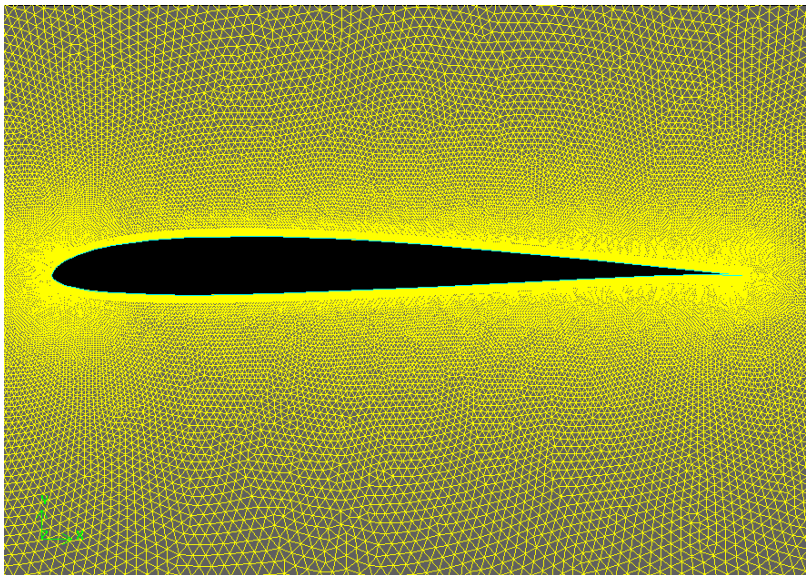

Figure 20 Boundary layer close to the airfoil

Figure 21 and Figure 22 show the lift and drag coefficients for SD 7003 airfoil at Re=60000. The numerical results of the present study are compared with the experimental and numerical solutions in the literature.

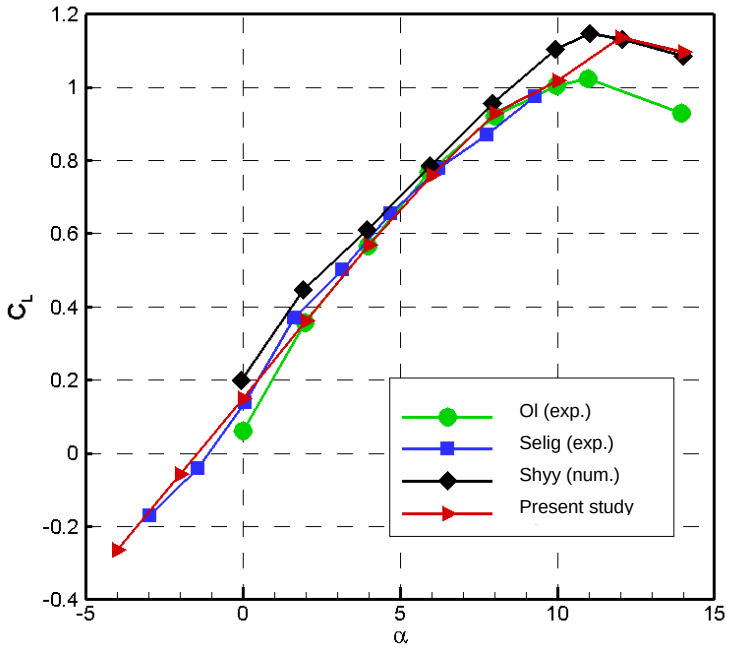

Figure 21 Lift coefficient versus angle of attack at Re=60000 for SD 7003 airfoil [compared with from Shyy, W., Lian, Y., Tang, J., Viieru, D. and Liu, H. (2008) Aerodynamics of Low Reynolds Number. Flyers, Cambridge University Press, New York]

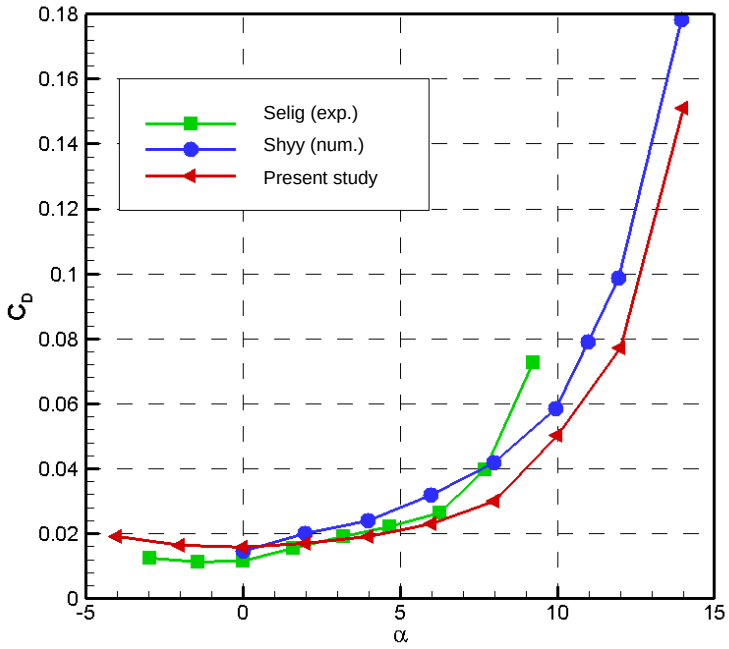

Figure 22 Drag coefficient versus angle of attack at Re=60000 for SD 7003 airfoil

Figure 23 shows the pressure coefficient contours around SD 7003 airfoil at Re=60000 for different angles of attack. As the angle of attack increses, the suction peak region close to the leading edge of the airfoil spreads towards the trailing edge of the airfoil. Stall angle is close to 11 degrees. Figure 24 shows the non-dimensional u-velocity component around SD 7003 at different angles of attack. The non-dimensional vorticity contours are also represented in Figure 25 for the stead-state solution.

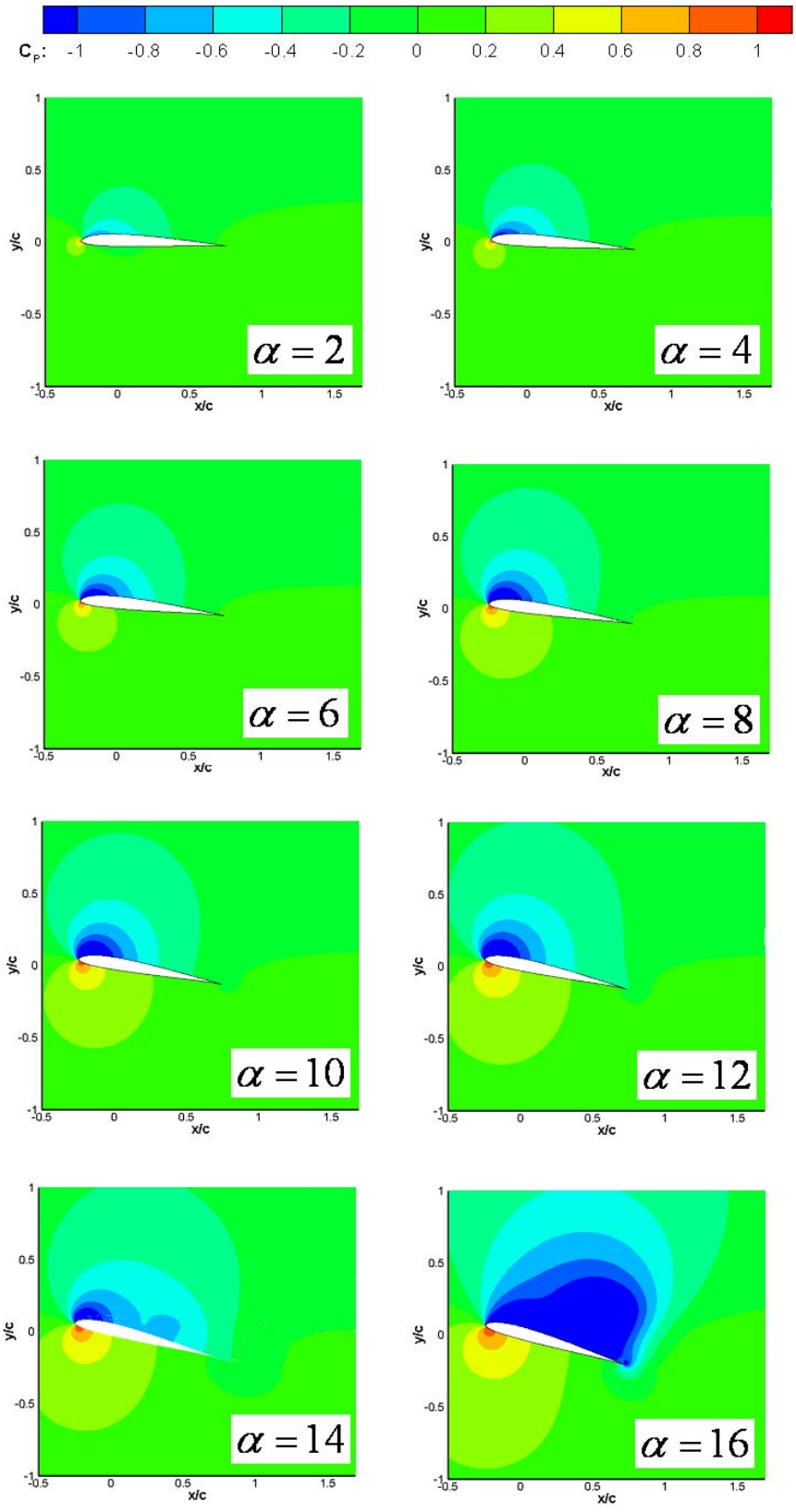

Figure 23 Pressure coefficient (C_P) around SD 7003 airfoil at different angle of attacks.

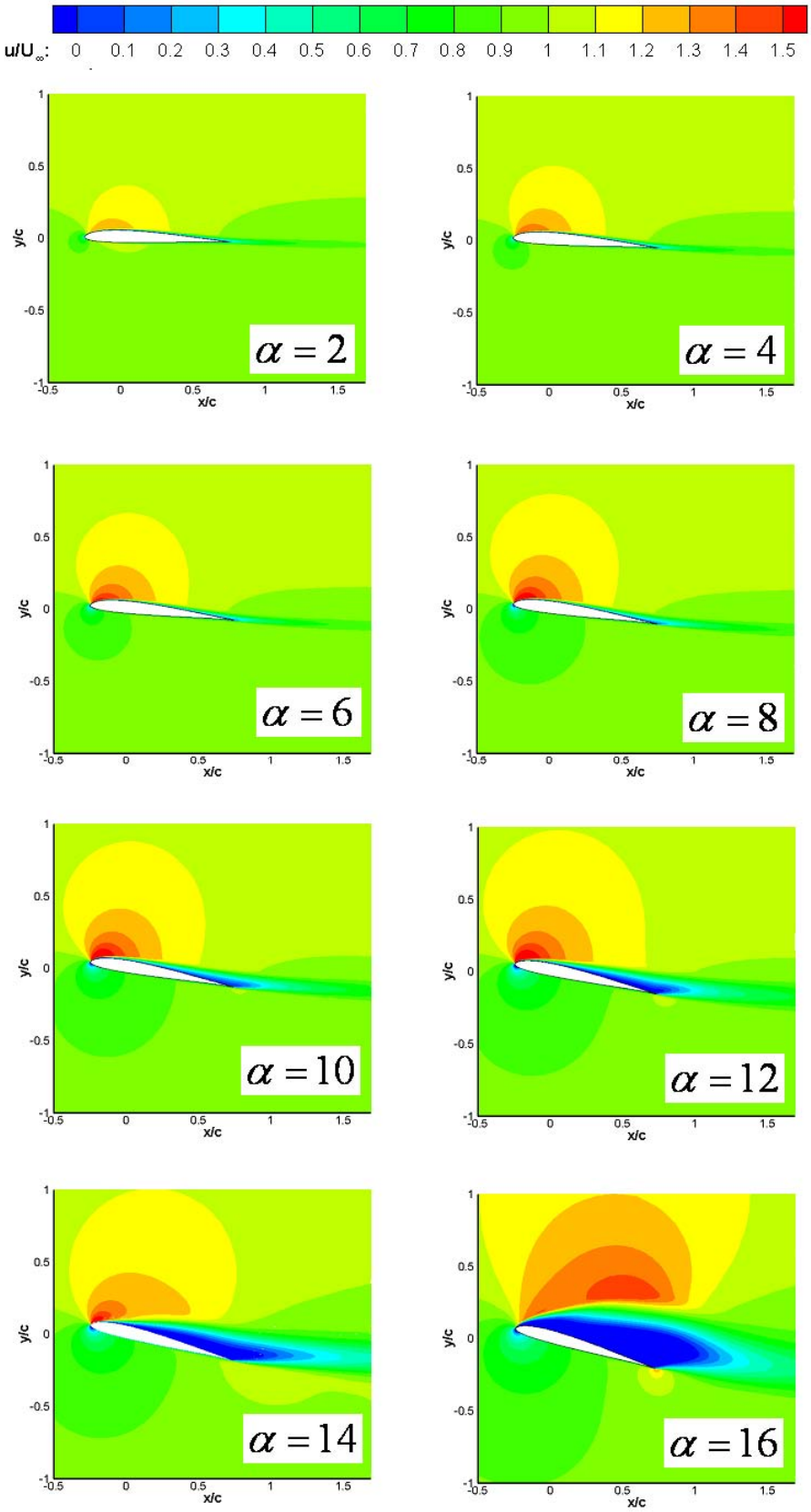

Figure 24 (u/U_∞) graph around SD 7003 at different angles of attack (Re=60000).

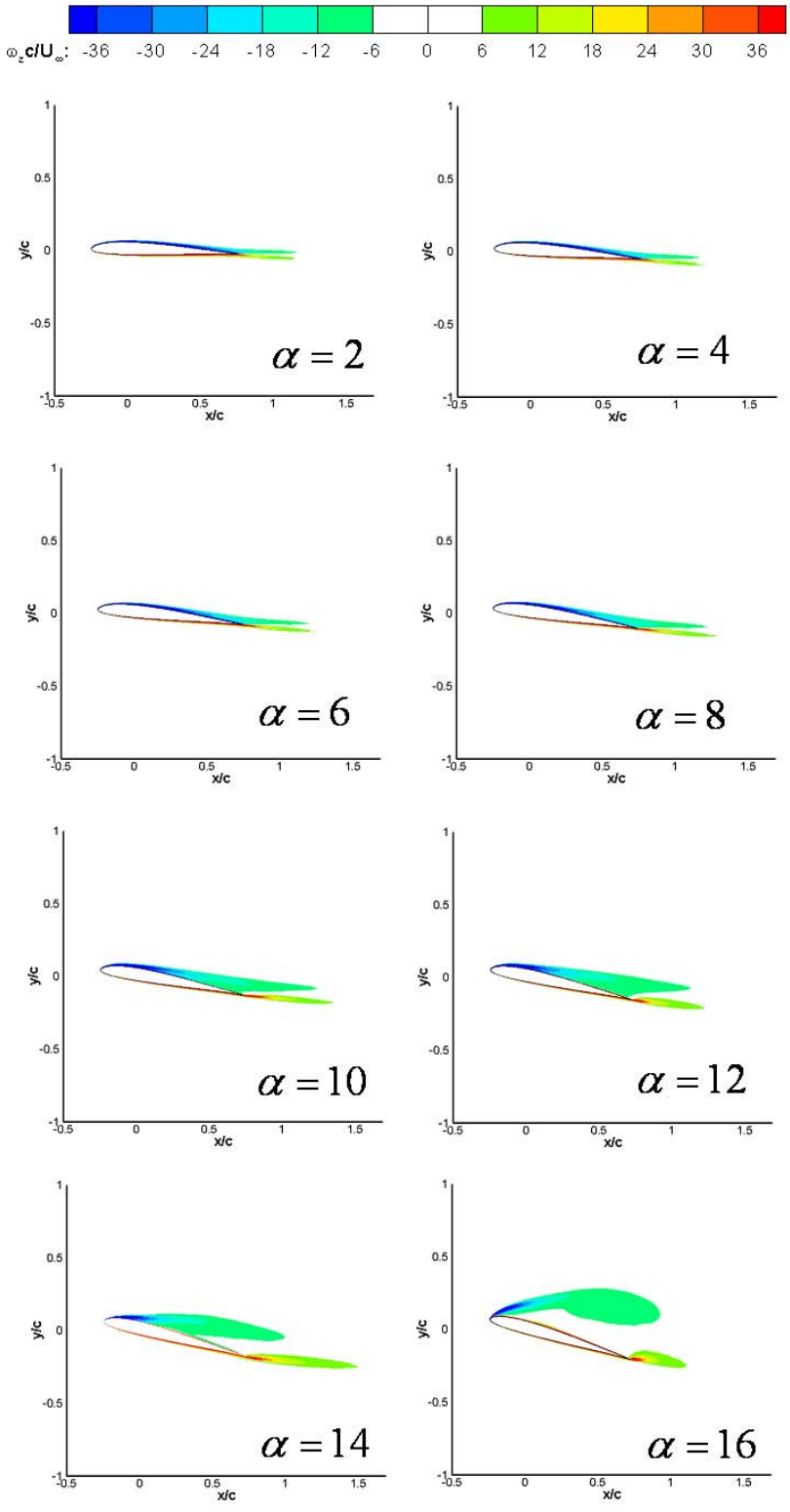

Figure 25 Non dimensional vorticity ($\omega_z c / U_\infty$) graph around SD 7003 airfoil.

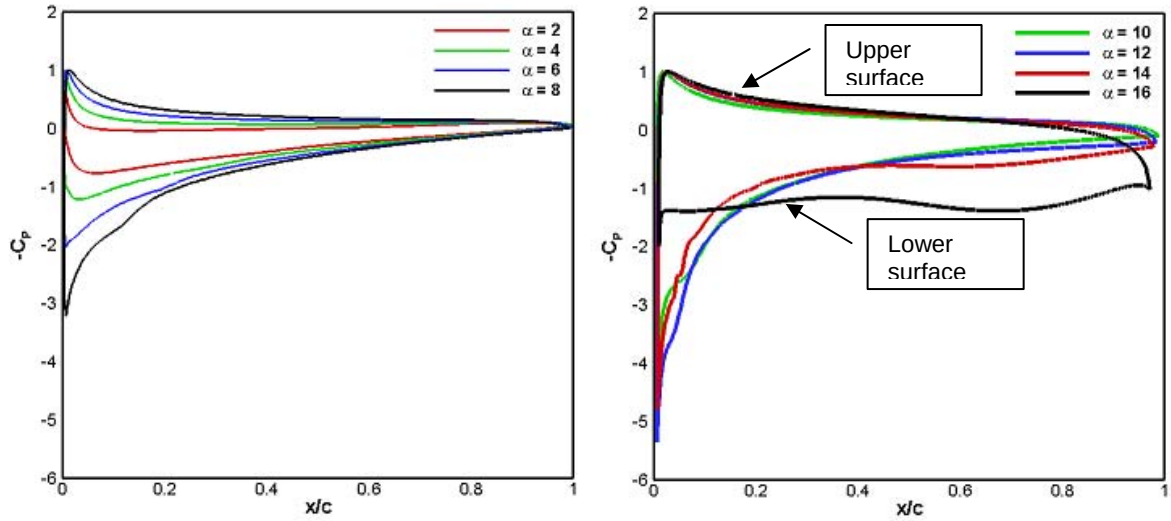

Figure 26 Pressure coefficient around SD 7003 airfoil at different angles of attack

Figure 27 represents the streamlines around SD 7003 airfoil. A trailing edge vortex structure is obseved at 12° angle of attack. A leading edge vortex structure detached form the airfoil surface with a trailing edge vortex is observed at 16° angle of attack. The suction region on the upper surface of the airfoil becomes dominant after 10° angle of attack as can be observed from Figure 24.

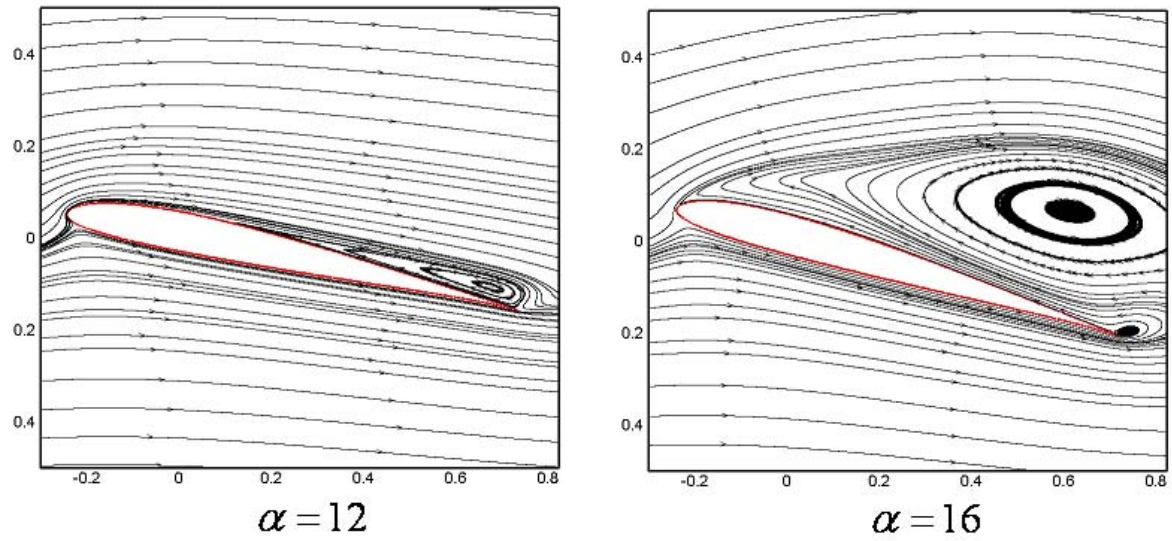

Figure 27 Streamlines around SD 7003 airfoil for 12° and 16° angles of attack (Re=60000).

b) Steady state solution around flat plate with 3.5% thickness at Re= 60000

For steady state solutions around flat plate, 84142 elements are used for the grid. The lift and drag coefficients at different angles of attack are given in Table 3 for Re=60000.

Table 3 Steady-state lift and drag coefficients for different angles of attack at Re=60000

AOA	CL	CD
4	0.46432	0.044677
8	0.78616	0.12399
12	0.68309	0.16936
16	0.85031	0.26908

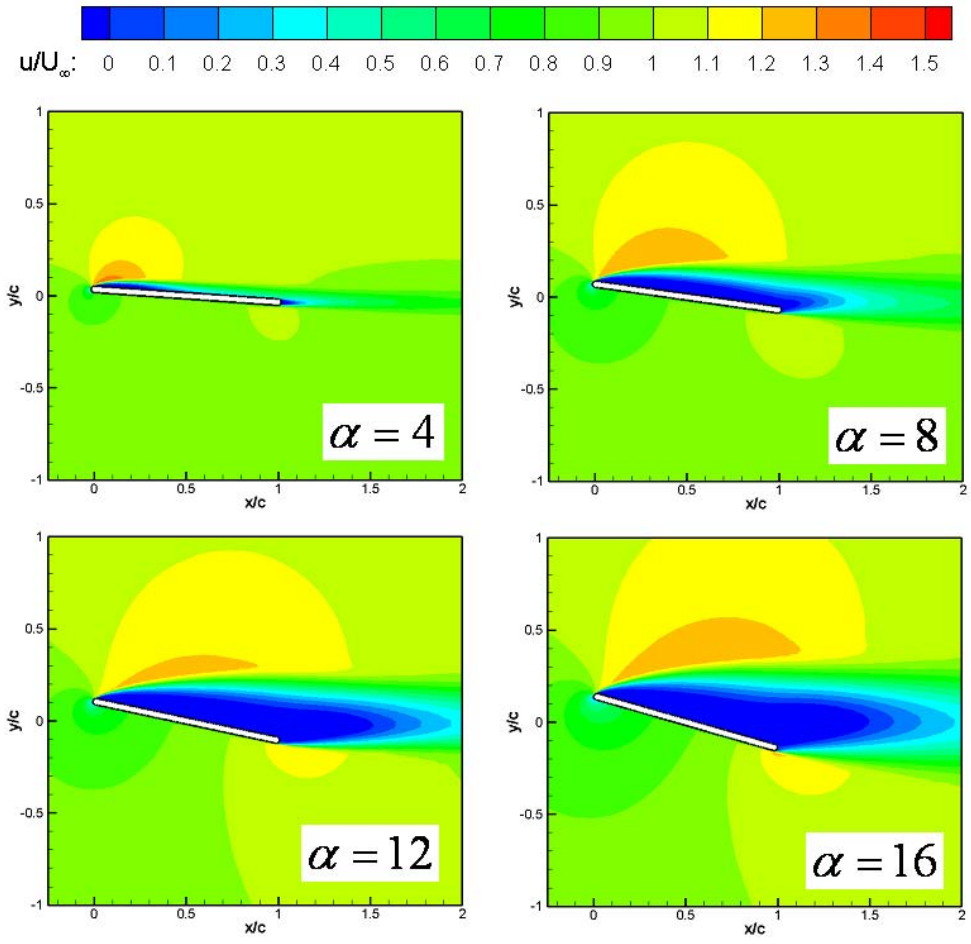

Figure 28 u/U_∞ contours around flat plate with 3.5% thickness (Re=60000)

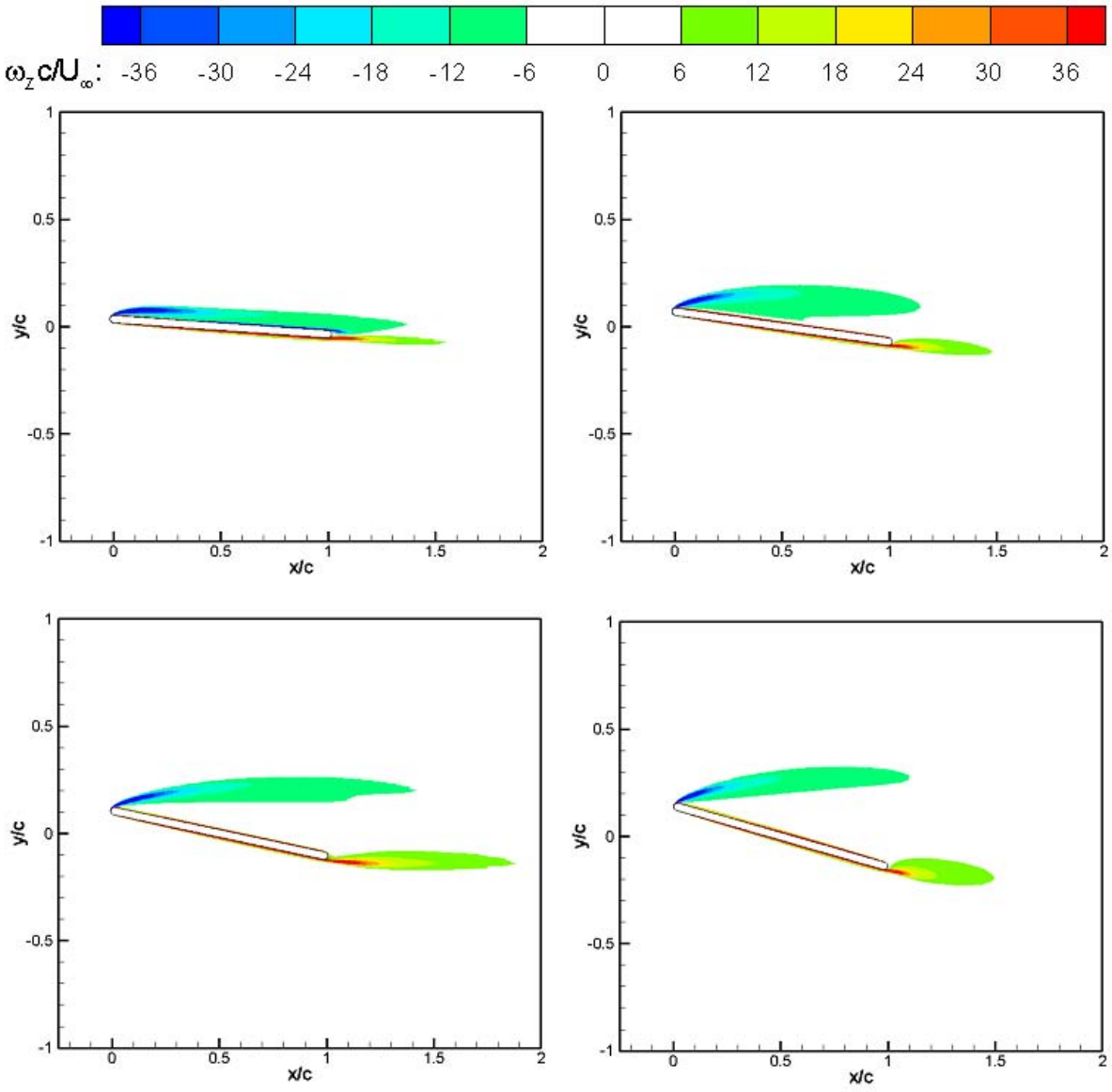

Figure 29 Non-dimensional vorticity contours around flat plate with 3.5% thickness (Re=60000)

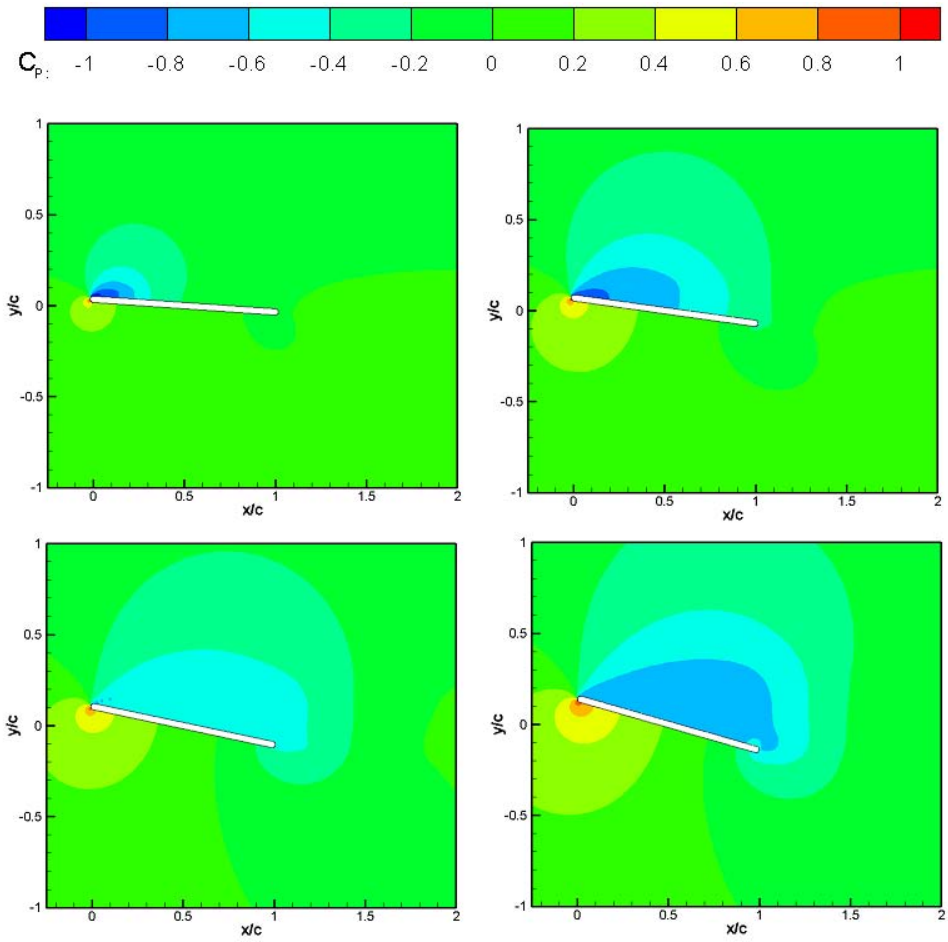

Figure 30 Pressure coefficient contours around flat plate with 3.5% thickness (Re=60000)

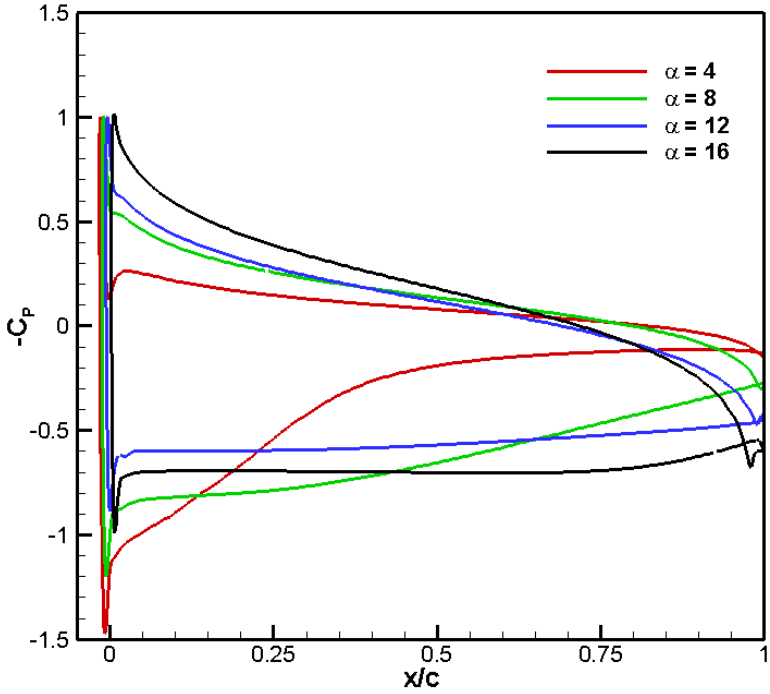

Figure 31 Pressure coefficient contours on the surface of flat plate with 3.5% thickness (Re=60000)

1.3 Unsteady Aerodynamic Computations of Different Sinusoidal Flapping Motions

(by Busra Akay (Ph.D. student TU Delft, Asst. Prof. Dr. D. Funda Kurtulus AE METU)

This study aims to analyze the present numerical method by simulating two dimensional flapping motion in hovering mode. Direct Numerical Simulation is used to solve the flow field around the two dimensional wing during the flapping motion. Unsteady, laminar, incompressible two dimensional Navier-Stokes Equations are solved by using moving grid technique. Two different sinusoidal motions are simulated by implementing the sinusoidal translational and angular motions using the same numerical solver and compared with the experimental results. This study is performed to explore the computational performance of the present numerical method and to analyze the sinusoidal flapping motion aerodynamics for different Reynolds numbers in the range 10^{1}-10^{3} by using different kinematics.

INTRODUCTION

Interest in the aerodynamics of insect flights has increased in conjunction with the concept of Micro Air Vehicles (μAVs). Based on their size, flying insects operate in a wide range of Reynolds numbers; from approximately 10 to 10^{5} [1]. Operating Reynolds numbers range of μAVs is similar with those of birds or insects. Thus, this similarity leaded most of the researchers to understand the aerodynamic basis for the flight of birds and insects.

Wang has defined hovering as an extreme mode of flight where the forward velocity is zero. To hover insects must draw clean air from the ambient flow and get rid of the `messy vortices' they have created to obtain a large periodic lift [2]. However, the hovering flight is quite expensive. While weak fliers and strong flying birds invest about 15 and 20 percent (respectively) of the total body weight in the breast muscles, hummingbirds invest about 30 percent of the total body weight in the breast muscles [3]. Although flapping wing design is more complex than a fixed wing design, there are many reasons to explore the possibilities of flapping wing flight. While the vehicle becomes smaller, the fixed wing application becomes less reasonable. The lift which a fixed wing generates to support the weight of the vehicle is directly proportional to wing area and velocity of air flow over the wing. Thus, the smaller the vehicle, the less lift it can supply. Provided with enough power, a vehicle with flapping wings could actually takeoff and land vertically [4].

To explore this complex topic, many researches have been performed numerically and experimentally. Here, some of the numerical works are reviewed. Many applications have been performed by using Navier-Stokes solvers in the field of flapping motion. NACA 0012 airfoil profile has been used as wing section in many applications ([5]-[9]). Elliptic profiles have also been used to investigate the flapping motion characteristics ([10]-[13]). Lan and Sun [10] explored the flapping motion at Re=1000 by using a Navier-Stokes solver for incompressible flow implementing moving overset grid. The results show that, if the insect employs a larger angle of attack or changes the timing of wing rotation, much greater lift can be produced for maneuvering and for other purposes. 3D flapping motion of the model fruit fly wing at Re=136 has been investigated by Sun and Tang [11] with some insights into the unsteady aerodynamic force generation process from the force and flow-structure information. They compared their results with the model wing experimental results and fruit-fly data provided by Dickinson et al. [14] and Weis-Fogh [15]. Weis-Fogh [15] aimed to provide new material and novel solutions to make use of the large number of observations on freely flying animals. His major conclusion is that most insects perform normal hovering on the basis of the well-established principles of steady-state flow. However, one must also realize that any type of flapping flight involves also non-steady periods, particularly at the reversal points where active pronation and supination occur. Wang ([2], [12]) has analyzed 2D hovering and flapping flight on elliptic wing section to identify the vortex shedding and their frequencies in the Re number range of 10^{2}<Re<10^{4}. Eldredge [13] has performed DNS solutions with viscous vortex particle method to investigate the pitching and plunging motion at Re=550.

NUMERICAL METHOD

Direct Numerical Simulation (DNS) technique is used to solve the present flapping motion problems. Simulation is performed for laminar, incompressible flow condition. The CFD code (Star-CD) used in this simulation has the capability to solve transient flow problems, to use moving mesh with arbitrary motions, to handle user defined properties and conditions by the use of user-defined subroutines, and it also has the capability of handling a large variety of boundary conditions, and offers a range of moving mesh features.

Wing Models and Their Kinematics

Two different sinusoidal flapping motions are analyzed in the present study. The first one is defined by Wang et al. [16] and in this study it is called 'Type A' flapping motion. It is applied to an ellipse having 12% thickness and 0.01m chord length. The computed results are then compared with three dimensional experiments and empirical data [16]. The second flapping motion is defined by Freymuth [17] and in this study it is called 'Type B' flapping motion. It is implemented to an elliptic wing model having a thickness of 1.6mm and a chord length of 0.0254m as in Freymuth's experiments [17]. Defined boundary conditions and inner grid domains used in the both simulations are presented in Figure 32. Grid domain is formed via GRIDGEN V15, a package programmed to generate grid domain. O-type grid domain is used around the profiles. According to the results of grid refinement study, 229x340 (229 number of nodes around the profile) grid domain is used in the numerical simulation of this study. The domains are formed in two sub-domains, inner domain is finer. The radius of the whole domain is 20 chords having a total of 77292 cells for the case of 'Type A' simulation. 259 numbers of nodes are put on the profile of case of Type B simulation. The radius of the whole domain is 20 chords having 82560 cells.

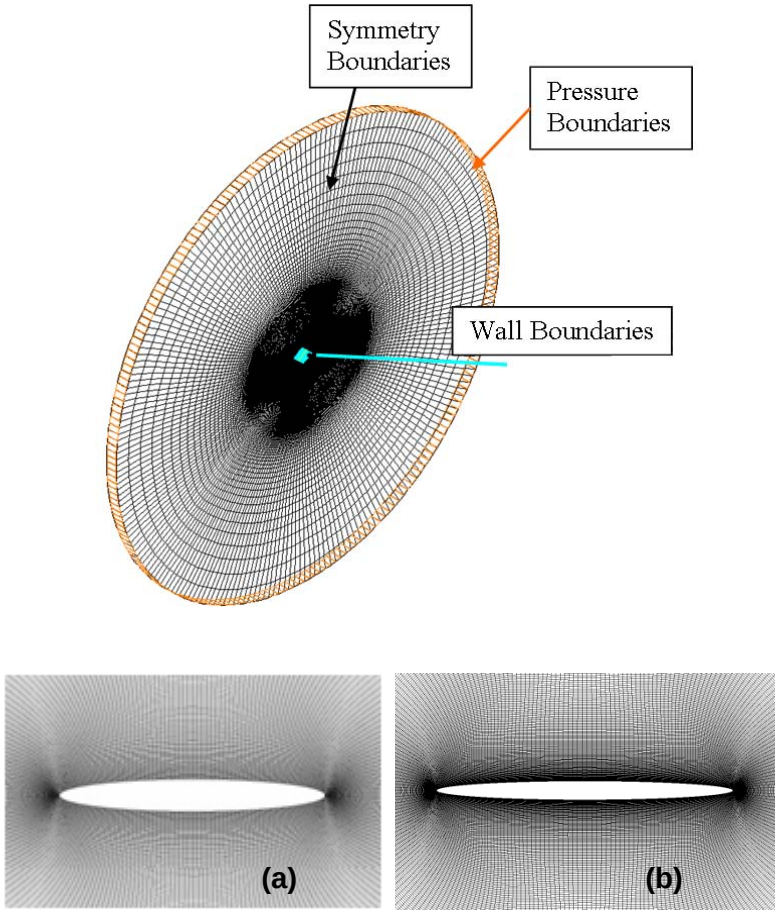

Figure 32 Defined boundary conditions and inner grid domains. Profile of (a) Type A simulation (b) Type B simulation

Kinematics of 'Type A' Flapping Motion

For the simulation of flapping kinematics of Wang et al. [16], an ellipse of 12% chord thickness is used (c=0.01m). For the ellipse (e=12%c), the same grid domain is used as the previous study. The wing follows a sinusoidal flapping and pitching motion (Eqs. 1-2, respectively) [16]. Specifically, the wing sweeps in the horizontal plane and pitches about its spanwise axis with a single frequency *f*:

$$x(t) = \frac{A_0}{2}\cos(2\pi ft) \tag{1}$$

$$\alpha(t) = \alpha_0 + \beta\sin(2\pi ft + \phi) \tag{2}$$

where *x(t)* is the position of the center of the wing, and α (t) is the wing orientation with respect to the x-axis. By definition, the translational and angular velocities are given by $U_0(t)=dx(t)/dt$ and $\Omega(t)=d\alpha(t)/dt$. The parameters include the stroke amplitude A_0, the initial angle of attack α_0, the amplitude of pitching angle of attack β, the frequency *f* and the phase difference ϕ between *x*(*t*) and $\alpha(t)$.

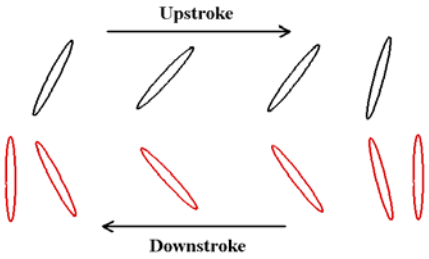

Figure 33 Sinusoidal motion of the profile during one stroke.

The translational motion of the wing is completely specified by two dimensionless parameters, Reynolds number, $Re=U_{max}c/\nu=\pi fA_0c/\nu$, and A_0/c, where U_{max} is the maximum flapping velocity, and *c* is the chord length. From their steady-state 2D numerical data Wang et al. [16] found the approximated empirical correlations for both of the aerodynamic coefficients, namely, C_L (Eq. 3) and C_D (Eq. 4) in terms of angle of attack α.

$$C_L = 1.2\sin(2\alpha) \tag{0}$$

$$C_D = 1.4 - \cos(2\alpha) \tag{4}$$

The constants depend on the Reynolds number, details of the wing, etc. They implemented this empirical data (Eq. 3-Eq. 4) for all of the instantaneous angle of attack variations that they have investigated. For each α value, C_L and C_D values are calculated. Quasi-steady translational lift (L_T) and drag forces (D_T) are calculated $0.5\rho u^2C_L$ and $0.5\rho u^2C_D$, respectively. All of the numerical and empirical forces are normalized by the maxima of the corresponding to quasi-steady forces as described in the study of Wang et al. [16].

Kinematics of 'Type B' Flapping Motion

In this part of the study, the flapping motion as defined by Freymuth [17] is investigated. Freymuth [17] used a planar airfoil having a thickness of 1.6mm and a chord of c=2.54cm with rounded edges to execute the combined plunging and pitching motions in the experiments. In the present numerical investigations an elliptical wing having the same thickness and chord as Freymuth's model is used.

The airfoil performs a translating (plunging) motion [17] h in horizontal direction (Eq. 5):

$$h = h_a \sin(2\pi f t) \tag{5}$$

where h_a is the amplitude of linear translation, f is the frequency of sinusoidal oscillation and t is the time. Considering that the airfoil performs a pitching motion (Eq. 6) simultaneously, around its half chord axis:

$$\alpha = \alpha_0 + \alpha_a \sin(2\pi f t + \phi) \tag{6}$$

where α is the pitch angle with respect to the horizontal as shown in Figure 34, α_0 is the mean pitch angle, α_a is the pitch amplitude and ϕ is the phase difference between pitching and plunging.

Dimensionless parameters of the system are: α_0, α_a, ϕ, the dimensionless plunge amplitude h_a/c and a Reynolds number;

$$R_f = 2\pi f h_a c / \nu \tag{7}$$

based on the maximum plunge speed $2\pi f h_a$ and on c, where v is the kinematic viscosity.

Two simple modes of hovering were initially identified by Freymuth [17]. In the present study only Mode 1 has been analyzed. "Mode 1" or "water treading mode" is characterized by $\alpha_0=0^o$ and $\phi=90^o$ and is sketched in Figure 34. The airfoil starts a cycle from the position of having pitch amplitude (α_a) at middle of the downstroke (indicated as right arrow). It moves a distance $2h_a$ to the right to reach its initial position. The right edge of the airfoil is leading during its motion to the right but when the airfoil returns left, the leading and trailing edges switch their roles.

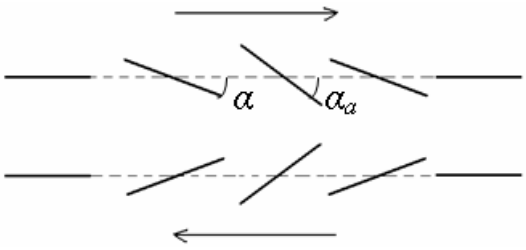

Figure 34 Sketch of combined translating-pitching motions of the airfoil for one cycle of mode 1 hovering ($\alpha_0=0^o$, $\phi=90^o$).

To characterize the time averaged thrust T on the airfoil, a thrust coefficient C_T is defined in Reference [17] (Eq. 8):

$$C_T = \frac{T}{0.5\rho\overline{V_t^2}cl} \tag{8}$$

where ρ is the air density, l>>c, is the span of the airfoil.

RESULTS

This part is devoted to the numerical analysis of different flapping motion kinematics for different Reynolds numbers in the range of (10^1-10^3). To explore the consistency of the present numerical method, experimental results obtained from the previous studies in the literature are compared with the numerical results of the present study.

Analysis of Type A Flapping Motion

Sinusoidal angle of attack and velocity distributions of the motion for different stroke amplitudes are presented in Figure 35 to show the difference of the kinematics by the change of A_0/c value. The frequency of the former is approximately twice of the later one.

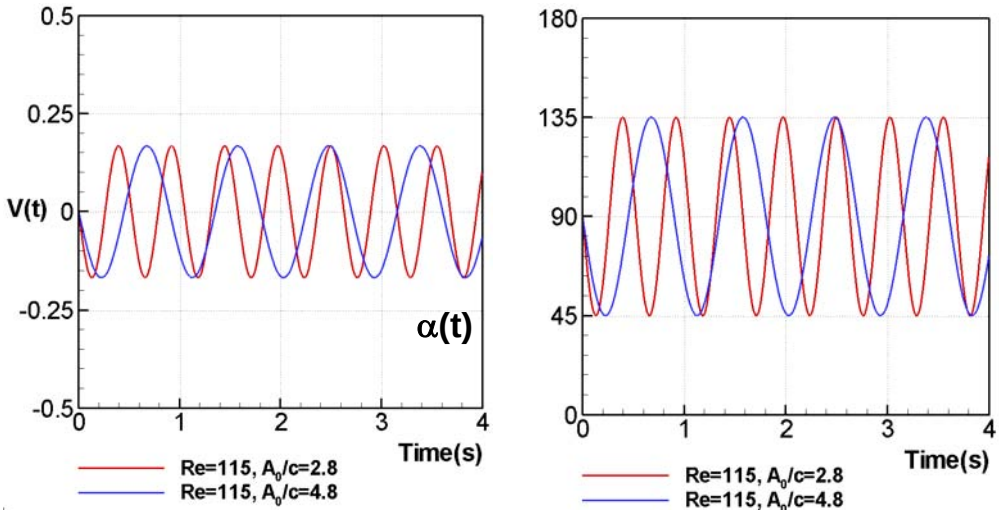

Figure 35 Instantaneous velocity and angle of attack (α (t)) distribution vs. time

In the following results, time is non-dimensionalized with respect to the flapping period of the case. In Figure 36, the computed forces obtained from the present study are compared with the experimental and empirical data of Wang et al. [16]. The empirical data is carried out by using the Eqs. 3-4 based on the translational velocity. The forces are normalized by the maxima of the corresponding quasi-steady forces [16]. For lift coefficient distribution, although there is a slight over estimation at the mid-strokes, the present computations catch the C_L values of the experiment during translation of the wing (see Figure 36). Also, the present computations estimate the right rotation position as in the experiment. For drag coefficient, it is observed that the general behavior of the distribution obtained by the present computations is very similar with that of the experiment [16]. Especially in the translational phase, they are very successful. Generally, it is noted that the present computations are very good at estimating the force coefficients of this problem.

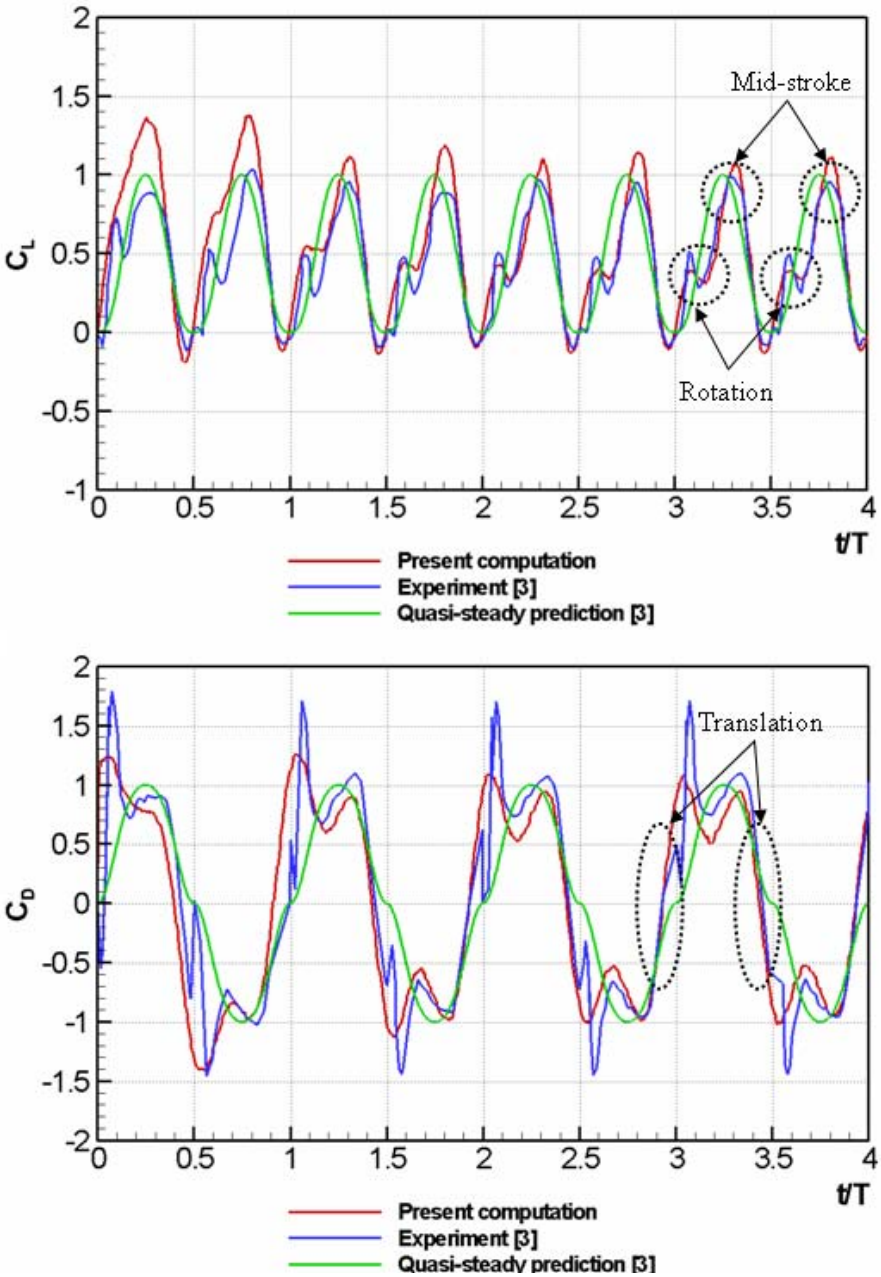

Figure 36 Lift and Drag coefficients comparison between experiment [16], present computation and quasi-steady estimations [16] for symmetric (φ=0) rotation, Re=75, and A_0/c=2.8. Time is non-dimensionalized with the flapping period of the case 1.

A comparison between computation and experiments of Wang et al. [16] and the present computational results will be presented for the case of A_0/c=4.8 and Re=115. In the first column of Figure 37, 2D computational results [16]; in the second column 3D experimental results in a 2D slice at 0.65R taken from DPIV measurements [16] and in the third column 2D computational results of the present study are represented respectively in columns 1 to 3 of Figure 37. Ten different time sequences are shown during the fourth stroke for each case. Time is non-dimensionalized with the flapping period of the case.

The vorticity contours are presented (see Figure 37) to show the major features of vortex dynamics through a complete stroke cycle. When the three results at each indicated time steps are compared, it is seen that the major features of vortex dynamics are similar. The color scale for vorticity of

computation and experiments [16] did not correspond to the exact same contour values. Due to lack of the color scale of vorticity contours achieved by Wang et al. [16], the figure of our computational results and their results should be viewed more qualitatively than quantitatively.

Notice that even though the kinematics of left and right strokes is identical, the flow fields for each case differ slightly for the computational results of Wang et al. [16]. However, this discrepancy in the flow field is not observed in our computational results.

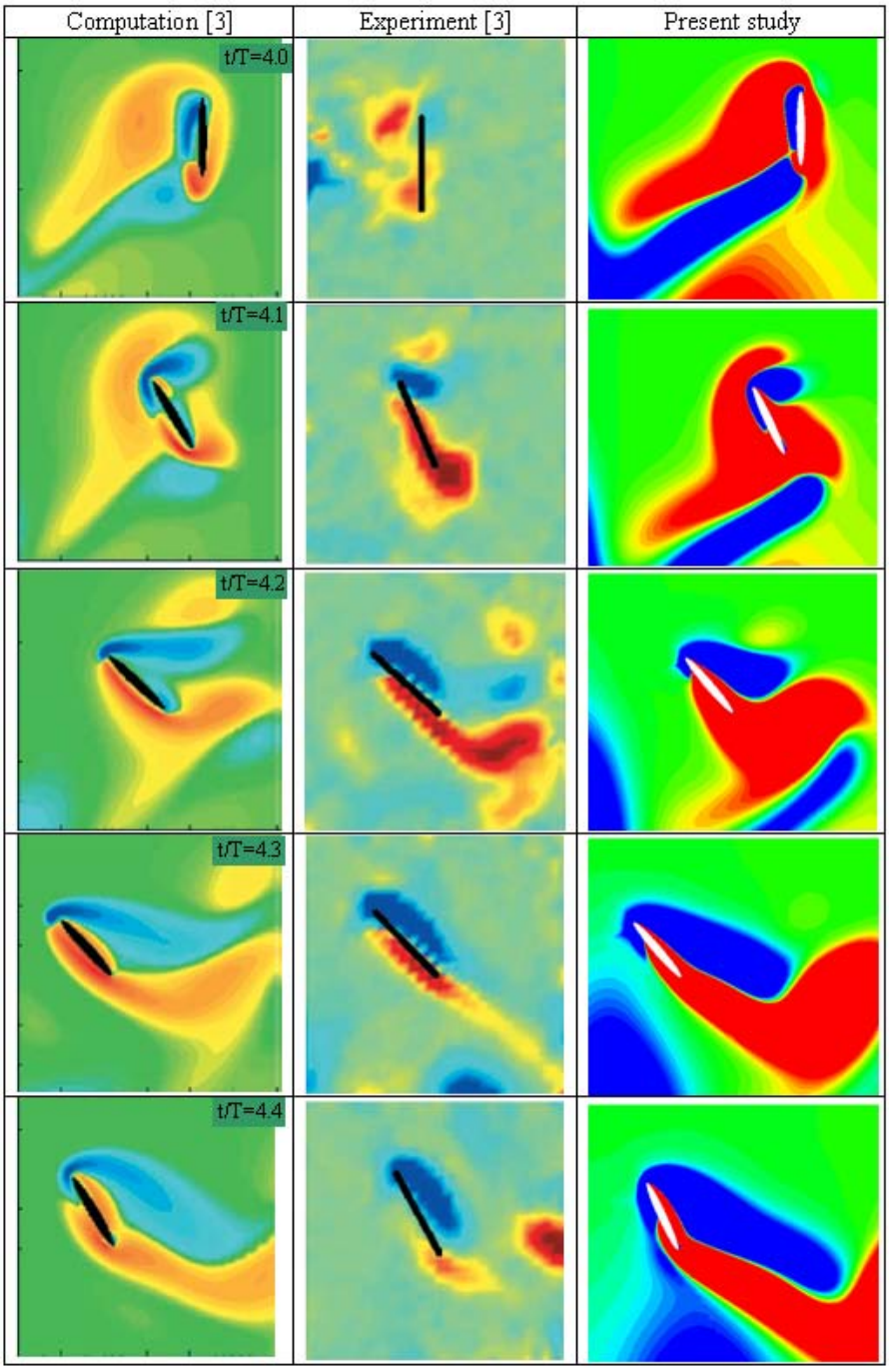

Figure 37 Instantaneous vorticity contour for case of A_0/c= 4.8, Re=115, φ=0. First two columns are the results of Wang et al. [16] and the third column is the results of the present study.

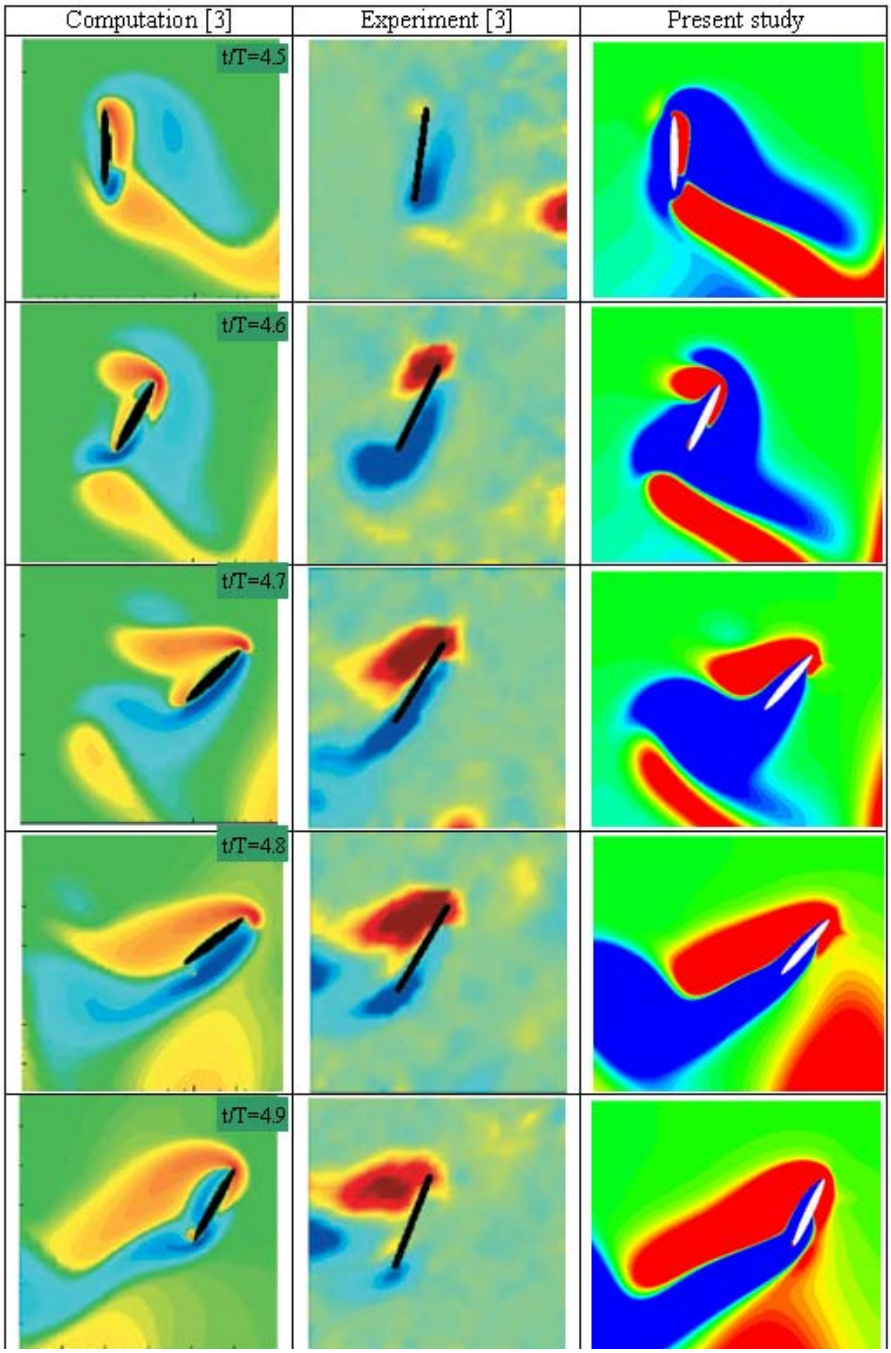

Figure 6 (Cont'd) Instantaneous vorticity contour for case of A0/c= 4.8, Re=115, φ=0. First two columns are the results of Wang et al. [16] **and the third column is the results of the present study.**

Analysis of Type B Flapping Motion

Sinusoidal variations angle of attack and velocity distributions of the motion for mode 1 are presented in Figure 38. Mode 1 flapping motion prescribed by Freymuth [17] is applied to the wing model. In Figure 39, force coefficient computed by using the present numerical method is compared with the experimental data of Freymuth [17]. The computed lift is non-dimensionalized according to Eq. 8. The results should be compared by bearing in mind the differences between two studies such as wing model, three dimensional effects of the experiments [17].

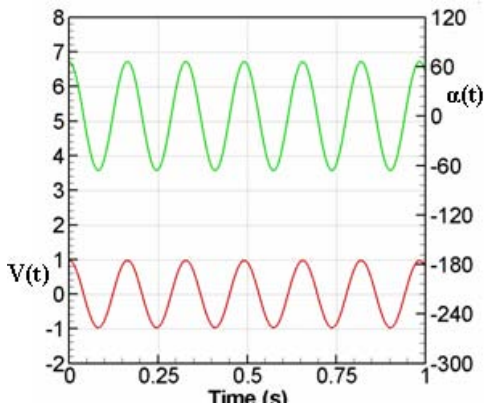

Figure 38 Instantaneous angle of attack (α(t)) and velocity distribution vs. time for mode 1 hovering.

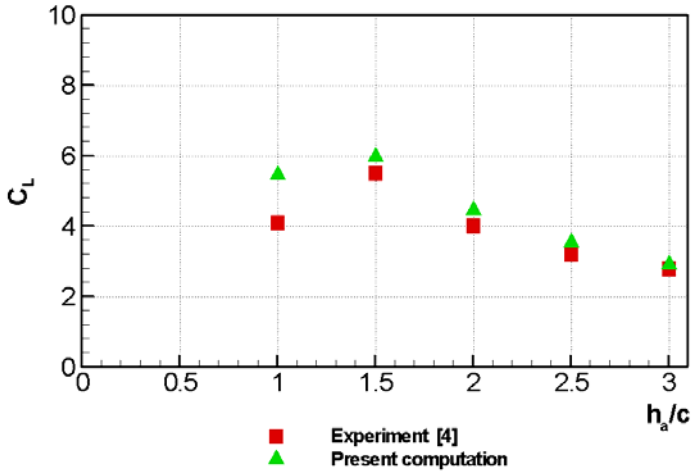

Figure 39 Lift coefficient comparison between experiment [17] and present computation for mode 1, $\alpha_a=66^o$, $\alpha_0=0$, $\varphi=90$ and $R_f=1700$.

Entire cycle of airfoil flapping in Mode 1 with $\alpha_a=66^o$, $h_a/c=1.5$ is shown in Figure 40 (a-b). Black and white pictures belong to Freymuth's experiment [17]. Flow visualization was by means of the titanium-tetra-chloride method described by Freymuth et al. [18]. Colorful pictures are results of the present study. Frames are ordered into columns from top to bottom and columns are ordered from left to right. Time between consecutive frames is $\Delta t=1/16$s. One should analyze the pictures by following the first and second columns together. First row of left two columns show the farthest right position of the airfoil (lower right corner of the frames). From this position to the bottom of the third and fourth columns, the airfoil moves its left position. During this movement, airfoil creates a clockwise (blue) rotating vortex which is very similar with the experiment [17] (see Figure 40 (a)-indicated in the last row). In columns 1 and 2 of Figure 40 (b), the airfoil moves to the right. The previously generated clockwise (blue) rotating vortex (see Figure 40 (a)-indicated in the last row) starts to detach from the upper surface of the airfoil and moves upward. And a new counterclockwise (red) rotating vortex is formed and grows (see Figure 40 (b)-indicated in the last row). This process repeats during each cycle and results in an upward moving vortex street. These vortex formations were observed in the experiment also [17].

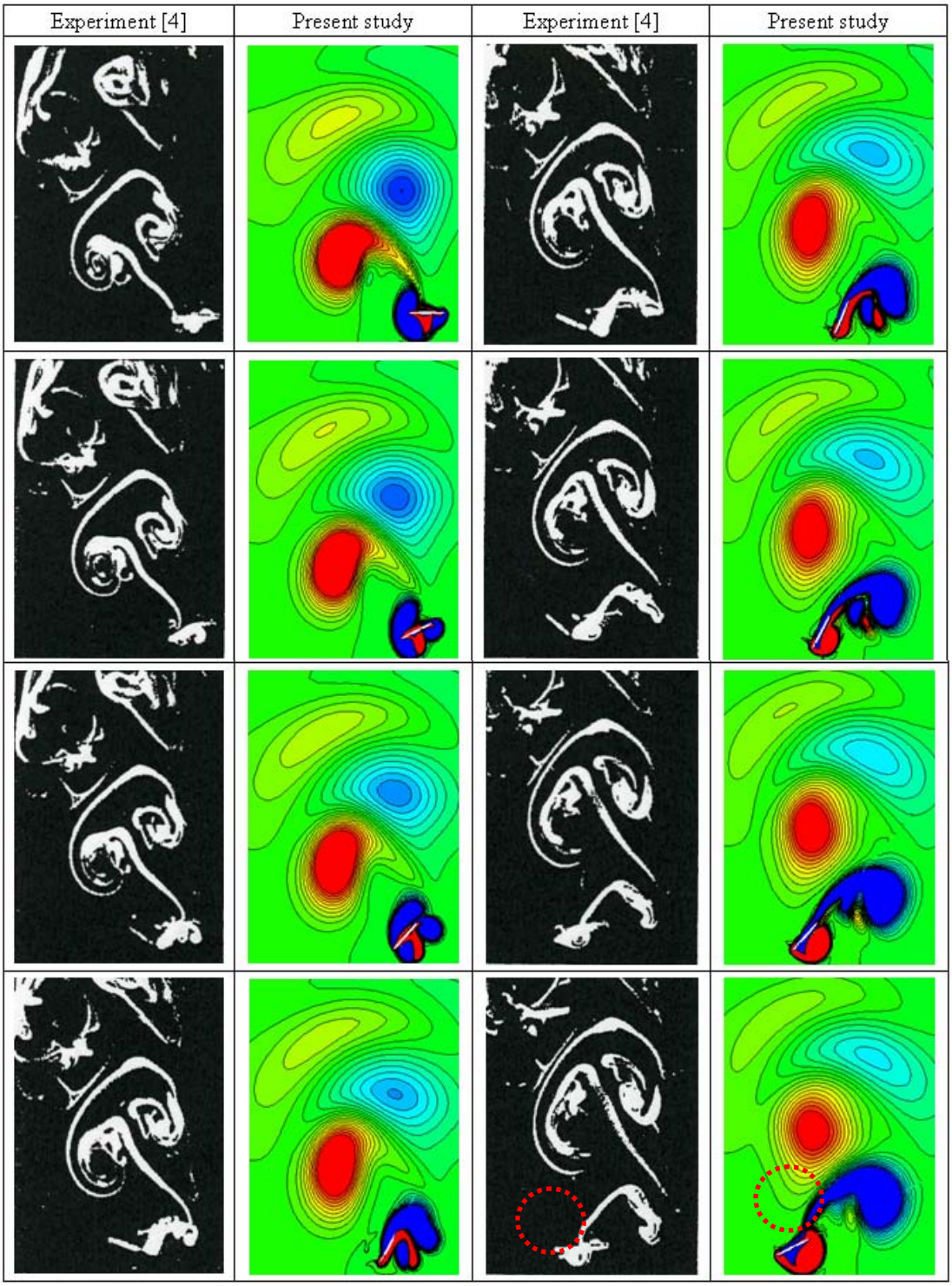

Figure 40 (a) Instantaneous vorticity contours for Mode 1. Black and white pictures are results of Freymuth [17] and the colorful pictures are results of the present study. α_a=66°, h_a/c=1.5, R_f=340, f=1Hz., Δt=1/16s.

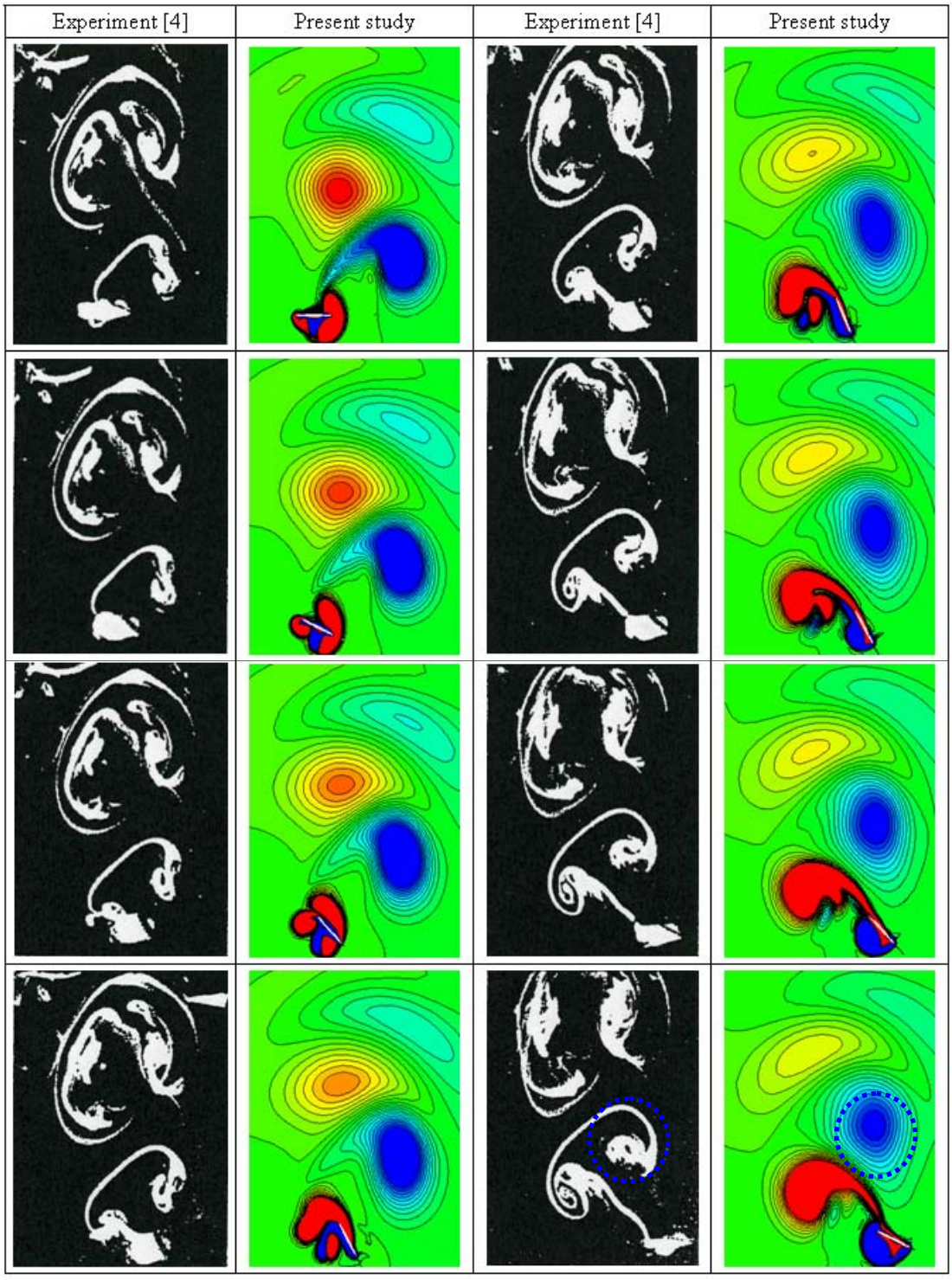

Figure 40 (b) Instantaneous vorticity contours for Mode 1. Black and white pictures are results of Freymuth [17] and the colorful pictures are results of the present study. α_a=66°, h_a/c=1.5, R_f=340, f=1Hz., Δt=1/16s.

CONCLUSION

A study is performed to analyze the different sinusoidal flapping motion kinematics defined by Wang et al. [16] and Freymuth [17] for different Reynolds numbers in the range of 10^1-10^3 by implementation of the sinusoidal translational and angular motions. Force coefficients and vorticity contours obtained from the experiments [16], [17] and present study are compared.

The sinusoidal motion defined by Wang et al. [16] is applied to a thin wing element of elliptic cross section having a thickness of 12% of its chord. The computed forces and vorticity distribution obtained from the present study are compared with 3D experimental, 2D numerical and empirical data of Wang et al. [16]. It is observed that the present computational method is good at estimating the force coefficients and the major features of vortex dynamics of the problem.

The sinusoidal flapping motion defined by Freymuth [17] is implemented to an elliptic profile having 1.6mm thickness and 0.0254m chord length. Force coefficients and vortex dynamics obtained from the experiments of Freymuth [17] and present study are compared. Although some parameters are different for numerical and experimental tests good agreement is observed between these two studies.

REFERENCE

[1] Sane, S.P., *The Aerodynamics of Insect Flight, J. Exp. Biol*, 206, pp. 4191-4280, 2003.

[2] Wang, J.Z., *Two Dimensional Mechanism of Hovering*, Phys. Rev. Lett. 85, 2216-2219, 2000.

[3] Copy right by Ehrlich, P.R., Dobkin, D.S., Wheye, D., "Hovering Flight", http://www.stanford.edu/group/stanfordbirds/text/essays/Hovering_Flight.html. (Last accessed date: August 2007)

[4] Michelson, R., Helmick, D., Reece, S., and Amarena, C., *A Reciprocating Chemical Muscle (RCM) for Micro Air Vehicle "Entomopter" Flight.*

[5] Tuncer, I.H. and Kaya, M., *Optimization of Flapping Airfoils for Maximum Thrust and Propulsive Efficiency,* AIAA Journal, Vol. 43, No. 11, pp. 2329-2336, 2005.

[6] Young, J. and Lai, J.C.S., *Oscillation Frequency and Amplitude Effects on the Wake of a Plunging Airfoil,* AIAA Journal, Vol. 42, No.10, pp. 2042-2052, 2004.

[7] Young, J., Numerical Simulation of the Unsteady Aerodynamics of Flapping Airfoils, PhD Thesis, Australian Defence Force Academy, 2005.

[8] Tuncer, İ.H., Walz, R., Platzer, M.F., *A Computational Study on the Dynamic Stall of a Flapping Airfoi*l, AIAA-98-2519, 1998.

[9] Kurtuluş DF, Farcy A, Alemdaroglu N., *Unsteady Aerodynamics of Flapping Airfoil in Hovering Flight at Low Reynolds Numbers*. AIAA-2005-1356, 43rd AIAA Aerospace Sciences Meeting and Exhibit, Reno, Nevada, USA, 10 - 13 Jan 2005.

[10] Lan, S.L., Sun, M., *Aerodynamic Force and Flow Structures of Two Airfoils in Flapping Motions*, Acta Mechanica Sinica (English Series), No.17, pp310-331, 2001.

[11] Sun, M., Tang, J., *Unsteady Aerodynamic Force Generation by a Model Fruit Fly Wing in Flapping Motion*, J. Exp. Biol, 205, pp. 55-70, 2002.

[12] Wang, J.Z., *Vortex Shedding and Frequency Selection in Flapping Flight*, Journal of Fluid Mech., 410,323-341, 2000.

[13] Eldredge, J.D., *Efficient Tools for the Simulation of Flapping Wing Flows*, 43rd Aerospace Sciences Meeting, January 10–13, Reno, NV. AIAA 2005-0085, 2005.

[14] Dickinson, M. H., Lehmann, F. O., Sane, S. P., *Wing Rotation and the Basis of Insect Flight, Science*, 284, June 1999.

[15] Weis-Fogh, T., *Quick Estimates of Flight Fitness in Hovering Animals, Including Novel Mechanisms for Lift Production*, J. Exp. Biol. 59, 169-230, 1973.

[16] Wang Z. J., Birch, J. M., Dickinson, M.H., *Unsteady Forces and Flows in Low Reynolds Number Hovering Flight: Two-Dimensional Computations vs. Robotic Wing Experiments,* J. Exp. Biol, 207, pp. 449-460, 2004.

[17] Freymuth, P., *Thrust Generation by an Airfoil in Hover Modes*, Experiments in Fluids, Vol. 9, pp. 17-24, 1990.
[18] Freymuth, p., Bank, W., Palmer, M., *Use of Titanum tetra-chloride for flow visualization of accelerating flow around airfoils.* In Flow Visualization III. (ed. Yang, W.-J.). Pp.99-105. Washington: Hemisphere, 1985.
[19] Akay B, Kurtulus D.F., Alemdaroglu N., *Unsteady Aerodynamics of Different Wing Profiles at Low Reynolds Number*, NATO AVT-146 Symposium on Platform Innovations and System Integration for Unmanned Air, Land and Sea Vehicles, 14-17 May 2007, Florence, Italy, 2007 .
[20] Akay B, Kurtulus DF, Alemdaroglu N., *Parametrical Study of Sinusoidal Flapping Motion Aerodynamics*, 4th Ankara International Aerospace Conference, Ankara, Turkey, (accepted), 2007.

2. Experimental Method

2.1 Vortex topology using PIV

(by Dr. D. Funda Kurtulus AE METU)

The flow around a flapping airfoil is investigated for different angles of attack by means of particle image velocimetry (PIV) technique at Re=1000. The objective is to show the influence of flapping motion in a flow where there exist abundant vortex structures. The instantaneous circulations are calculated for the vortices generated at the leading edge and trailing edge of the airfoil during the impulsive start of the flapping motion and during the pseudo-periodic motion where the influence of the impulsive start disappears. The vortex generation mechanism at the impulsive start is studied for the understanding of the flapping motion vortex topology in order to distinguish the characteristics of vortices generated during the motion without the influence of the traces from the previous strokes. By comparison with the same location for the periodic motion, the influences of the traces of the previous motion and the last vortices shedded at the end of the translational phase are exhibited.

1. Introduction

In order to understand the high lift mechanisms of flapping wings, lots of investigations are performed these last years. The vortical flow patterns in the wake of a NACA 0012 airfoil pitching at small amplitudes are studied experimentally by Koochesfahani (1989) in a low-speed water channel by considering the effect of both sinusoidal and non-sinusoidal shape of the waveform. The unsteady flow structures are investigated with dye visualization by Freymuth (1990). He has worked on experimental simulation of sinusoidally pitching and plunging thin flat plate to investigate the thrust generation mechanism in hover mode with Re number range of 340 to 1700. He examines the dynamic stall vortices effects in order to obtain large thrust values.

PIV and SPIV have been often used as an experimental tool to analyze the flapping flight vortical structures. Poelma et al. (2006) have performed a 3D Steoreoscopic PIV experiment in a mineral oil tank for the flapping flight with dynamically scaled robotic wing at Re=256. Wang et al. (2004) have performed PIV experiment together with the force measurement by using 2D force sensors at low Re number (50<Re<200). Dynamically scaled robotic fly has been used in their experiments. Laser sheet visualizations and 2D PIV experiments in a water tank have been performed by Kurtulus et al. (2008) with NACA 0012 airfoil in the Re number range of 500<Re<2000. Ol (2007) and Radespiel et al. (2007) recently investigated vortical structures generated during the pitch and plunge motions of SD7003 airfoil at Re=60000.

Dickinson et al. (1999) have performed an experiment in a mineral oil tank with a dynamically scaled model of the fruit fly to investigate 3D flapping motion at Re=136. The wing was equipped with a 2D force transducer. Before this study, Dickinson and Götz (1993) have performed similar experiment in an aquarium by using 2D impulsively moved model wings in the range of 10<Re<1000. In this experiment, the direct force measurements were correlated with CCD camera visualization. Clap and fling movement have been analyzed using dynamically scaled mechanical model of the small fruit fly by Lehmann et al. (2005). They performed 3C SPIV experiment and used force transducer to get the force distribution in the range of 100<Re<200.

Some zoological experiments have also been carried out by the researchers. Tian et al. (2006) have implemented PIV by using fog generator in a flight cage to understand 3D kinematic motion during straight and turning of bat flight in the Re number range of 10^4<Re<10^5. Galvao et al. (2006) have

explored 3D mammalian flight with compliant membrane wing models in the range of 70000<Re<200000. They have used low-speed, low turbulence wind tunnel with stereo photogrammetric method. 2D biomimetic flapping-pitching wing is analyzed by Singh et al. (2005) using laser sheet visualization method. Usherwood et al. (2005) have investigated flapping flight to obtain dynamic pressure maps of wings and tails of Pigeons. Platzer and Jones (2006) have recently reviewed different flapping wing studies.

In the view of all these different studies, different effects are analyzed in order to explain the fluid physics responsible for lift generation (Dickinson 1994, Sane 2003, Viieru et al. 2006). Wagner effect (Wagner 1925, Sane 2003) is only applicable at the beginning of the impulsive start of the motion. When an inclined wing starts impulsively from rest, the circulation around it does not immediately attain its steady state value. This effect is found to be not strong both in 2D experiments of Dickinson and Götz (1993) and 3D flapping translation experiments of Dickinson et al. (1999) at low Re number regimes.

Delayed stall effect results from the growth of the attached leading edge vortex which produces very high lift coefficients for several chord length translations before its detachment from the airfoil upper surface and before the formation of trailing edge vortex. These leading-edge vortices result in a large suction region on the upper surface of the airfoil during translation phase of the flapping motion and enhance the lift (Kurtulus et al. 2008). This phenomenon repeats by the detachment of trailing edge vortex and creation of new leading edge vortex (von Karman vortex street).

Kramer effect (rotational forces or fast pitching up) is due to the rotation of the airfoil at the end of the stroke reversals. The wing generates a rotational circulation (proportional to the angular velocity of rotation) in the fluid to counteract the effects of rotation and as a result rotational force peaks are generated during stroke reversals to re-establish the Kutta condition during the rotation. (Sun and Tang 2002, Sane and Dickinson, 2002, Sane 2003, Viieru et al. 2006). Another phenomena is the added mass effect due to the acceleration of the airfoil and the reaction of the fluid to this acceleration (Sane 2003, Ansari et al. 2006).

Wake capturing is another concept which is widely investigated in flapping motion studies. During reversal, airfoil enters to the trace of the vortices generated during the previous stroke and encounters to their velocity and acceleration fields, thus resulting in higher aerodynamic forces immediately following stroke reversal (Sane 2003). This is the explanation of the second peak observed at the instantaneous aerodynamic force coefficients.

This study aims to investigate the flow around a flapping airfoil for different angles of attack by means of particle image velocimetry (PIV) technique at Re=1000. The objective is to show the influence of flapping motion in a flow where there exist abundant vortex structures. The instantaneous circulations are calculated for the vortices generated at the leading edge and trailing edge of the airfoil during the impulsive start of the flapping motion and during the pseudo-periodic motion where the influence of the impulsive start disappears.

2. Description of Motion and Experimental Setup

The model is simplified by use of a symmetrical airfoil (NACA 0012). The flapping motion is composed by the superposition of a translational motion and a rotational motion around a center of rotation. During the translational phase, the airfoil translates with a constant velocity until the time t_v and the position x_v, where a rotational motion around a point on the chordline is superposed to the translational motion at a predefined time t_a and position x_a. The translational velocity is zero ($V = 0$) at the end of the strokes. When the time t_a and the position x_a is reached, the airfoil starts to rotate around its center of rotation to have 90° angle of attack at the end of the stroke. The rotation is such that the leading edge stays as leading edge during all phases of the motion. The translational velocity (V) and the angular velocity (ω) variation are given by Eq. 1 and Eq. 2. The continuity of the velocities is conserved by these suggested motions.

$$V = V_0 \cos\left(\frac{\pi}{2}\frac{t - t_v}{\frac{T}{4} - t_v}\right) \tag{1}$$

$$\omega = -\frac{\alpha_0}{\frac{T}{4} - t_a}\left(1 - \cos\left(\frac{\pi(t - t_a)}{\frac{T}{4} - t_a}\right)\right) \tag{2}$$

V_0 is the constant translational velocity, α_0 is the constant angle of attack and T is the period of the motion.

The experimental setup is a 1.5 m× 1 m× 1 m water tank made of altuglas and filled with water (Figure 41). A rectangular wing of 6 cm chord and 50 cm length having a NACA 0012 airfoil section is displaced inside the tank by associating a rotational and a translational motion. The center of rotation is at the quarter chord location. The wing is delimited by two rectangular plates made of epoxy with 50 cm × 90 cm dimensions in order to obtain a 2D flow. PIV measurements are performed with a 30 mJ Quantel Twin Ultra Nd:YAG laser using two CCD cameras in order to visualize the whole flapping domain with a field of view of 25 cm × 50 cm with each one recording 80 double frames per period. The laser is coupled with a spherical lens followed by a cylindrical lens. A mirror is located at the bottom center of the water tank to spread the light of the laser to the whole flow domain as wide as possible and to limit the shadow generated by the model. Two CCD cameras with 60 mm objectives and F number of 4 are used to record the entire flow domain.

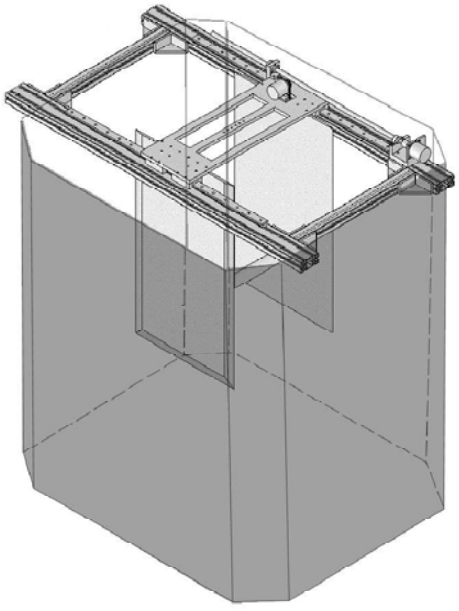

Figure 41 Experimental setup in water tank

3. Results

The flow periodicity is investigated for a single case chosen with starting angle of attack $\alpha_0=60°$ and impulsive period and the following periods are compared until the flow periodicity occurs. The impulsive start effect is observed to disappear before the 7th period. Thereafter, the influence of different parameters on vortex topology and circulation of the vortices are represented.

3.1 Vortex recognition method

The velocity gradient is made of two parts:

$$u_{i,j} = \frac{\partial u_i}{\partial x_j} = \frac{1}{2}\left(\frac{\partial u_i}{\partial x_j} + \frac{\partial u_j}{\partial x_i}\right) + \frac{1}{2}\left(\frac{\partial u_i}{\partial x_j} - \frac{\partial u_j}{\partial x_i}\right) \tag{3}$$

where i,j (=1,2) are free indices, u_i is corresponding velocity component and x_j is the corresponding space coordinate in Cartesian system. The velocity gradient is summation of the symmetrical rate-of-strain (deformation) tensor S_{ij} and the skew-symmetrical rate-or rotation tensor Ω_{ij}).

$$S_{ij} = \frac{1}{2}\left(\frac{\partial u_i}{\partial x_j} + \frac{\partial u_j}{\partial x_i}\right) \tag{4}$$

$$\Omega_{ij} = \frac{1}{2}\left(\frac{\partial u_i}{\partial x_j} - \frac{\partial u_j}{\partial x_i}\right) \tag{5}$$

The second invariant of velocity gradient (also called as second invariant of the mean rate-of-displacement tensor) is given by Eq.6.

$$Q = \frac{1}{2}\left(\Omega_{ij}\Omega_{ij} - S_{ij}S_{ij}\right) = -\frac{1}{2}\frac{\partial u_i}{\partial x_j}\frac{\partial u_j}{\partial x_i} \tag{6}$$

Nondimensional Q is defined as:

$$Q_{ND} = \frac{Q \cdot c^2}{(V_0)^2} \tag{7}$$

where c is the chord length and V_0 is the maximum velocity of the airfoil during the flapping motion.

For the 2D motion:

$$Q = -\frac{1}{2}\left(\left(\frac{\partial u_1}{\partial x_1}\right)^2 + \frac{\partial u_1}{\partial x_2}\frac{\partial u_2}{\partial x_1} + \left(\frac{\partial u_2}{\partial x_2}\right)^2\right) \tag{8}$$

A technique by use of Q criteria is used to distinguish the instantaneous and local vortex formation. The centers of the instantaneous local vortices are found by using maximum local Q values in the velocity flowfield. In addition, positive Q contours are used to detect the boundaries of each local vortex.

Circulation of each vortex is calculated by Eq. 9.

$$\Gamma_{ND} = \frac{\Gamma}{V_0 c} = \frac{1}{V_0 c}\oint \vec{V} \cdot d\vec{l} \tag{9}$$

where the integration is carried out along the detected vortex boundary. $\vec{V}$ denotes the velocity vector along the contour of the vortex and *dl* stands for the elemental length along the contour.

The airfoil starts from the rest its motion with a 90° angle of attack with zero translational velocity and reaches at a constant angle of attack α_0 at x_a and at a constant velocity V_0 at $x_v=2c$. The rotation and translation of the airfoil are referenced with respect to the 1/4c centre of rotation.

The flow periodicity is investigated with starting angle of attack $\alpha_0=60°$ and impulsive period and the following periods are compared until the flow periodicity occurs. The impulsive start effect is observed to disappear before the 7th period. Figure 42 represents instantaneous vorticity distribution beginning from the impulsive start of flapping airfoil for $\alpha_0=60°$ case. Consecutive PIV images are represented with a time step of $\Delta t^*=0.0125$ (80 photo per period) from the beginning to the half-amplitude location of the upstroke.

Erreur ! Source du renvoi introuvable. represents the vortices distinguished by the Q criteria from the PIV flowfield. The centers of the vortices are represented by the red symbols for the counter-clockwise vortices and by blue symbols for the clockwise vortices.

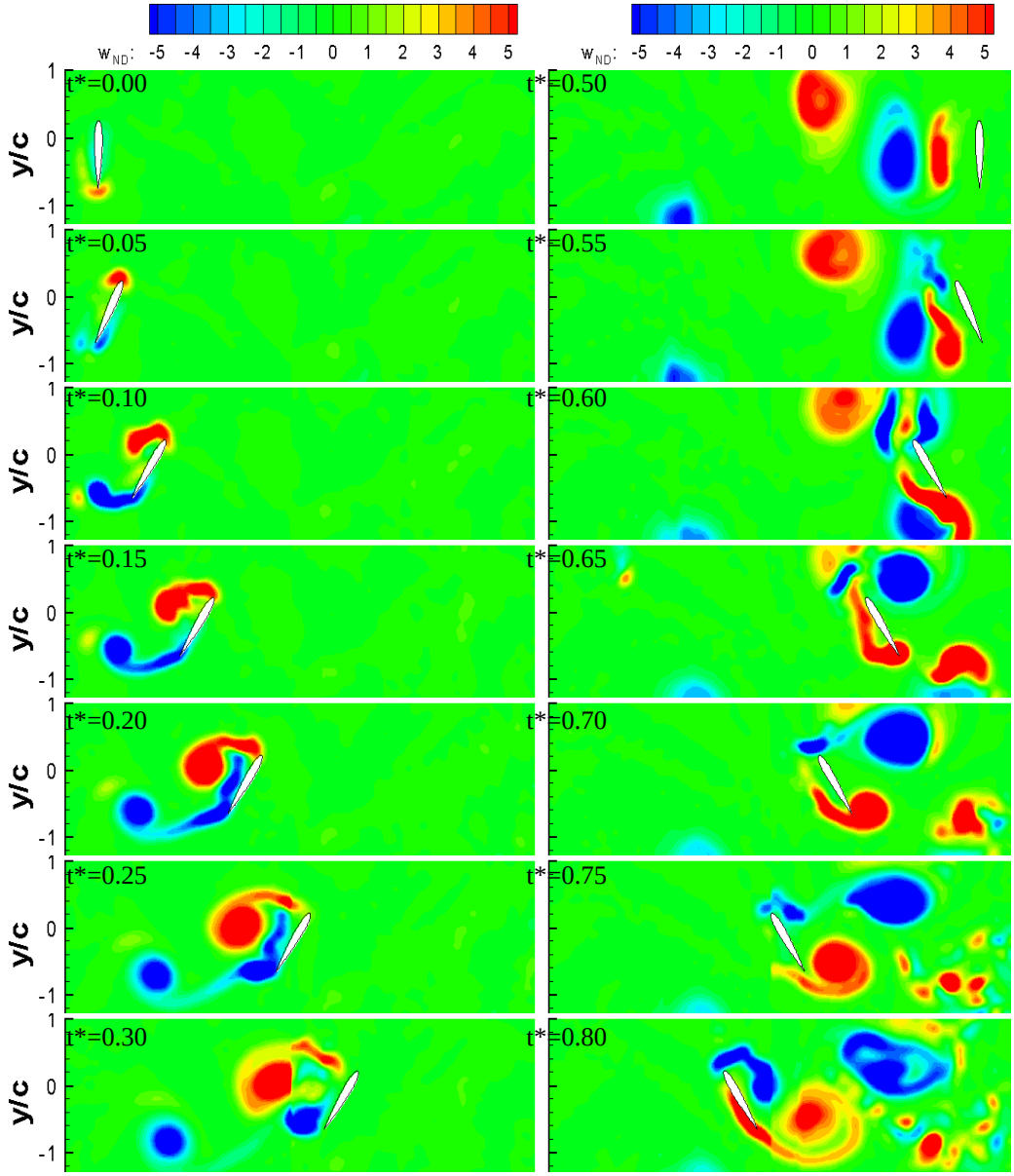

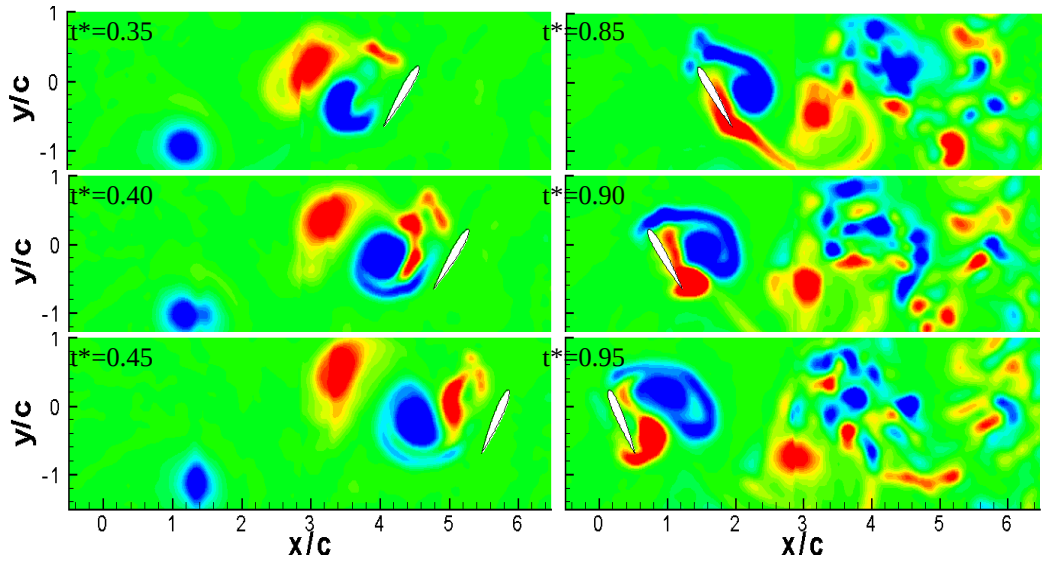

Figure 42 Instantaneous vorticity for α_0=60° beginning from impulsive start (photos are consecutive PIV images during 1st stroke.

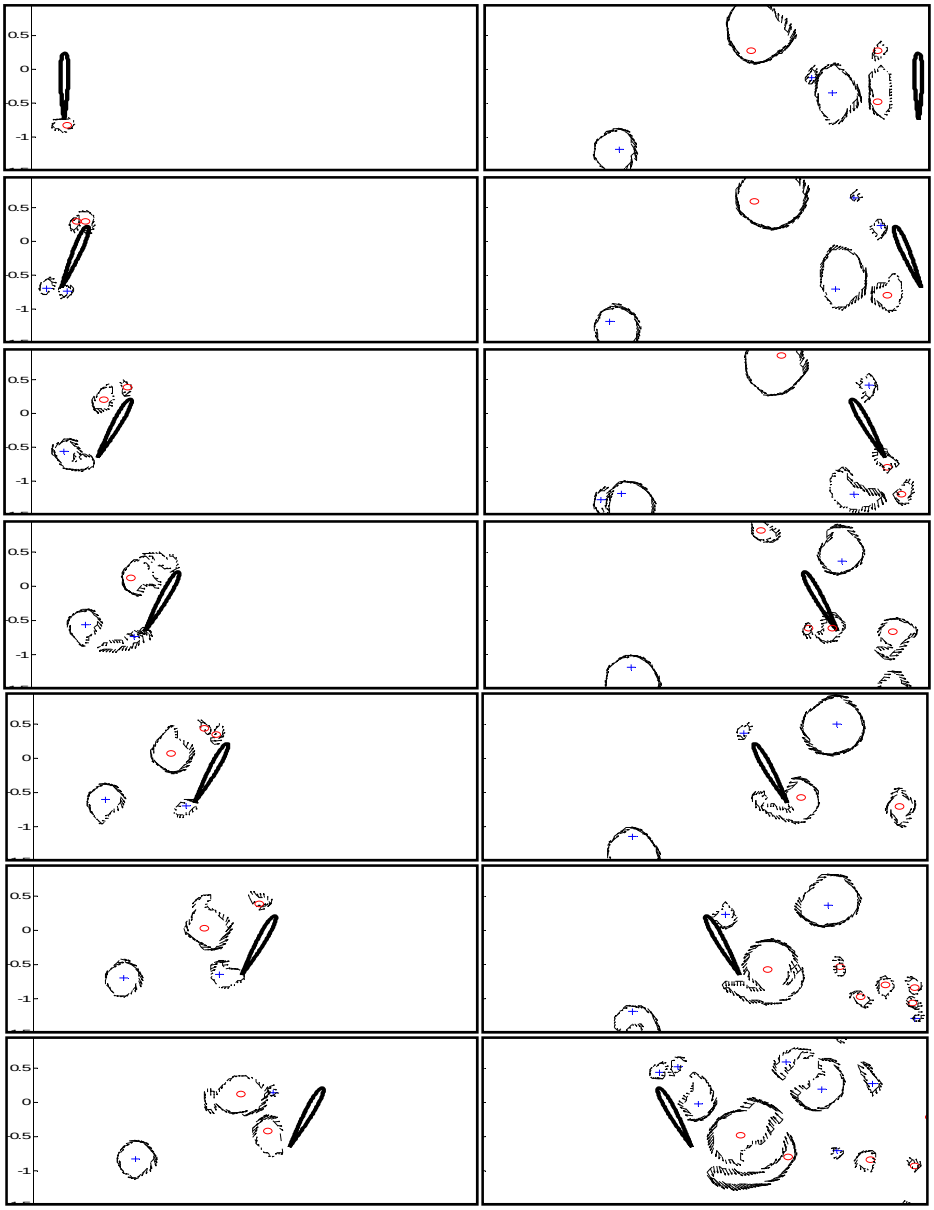

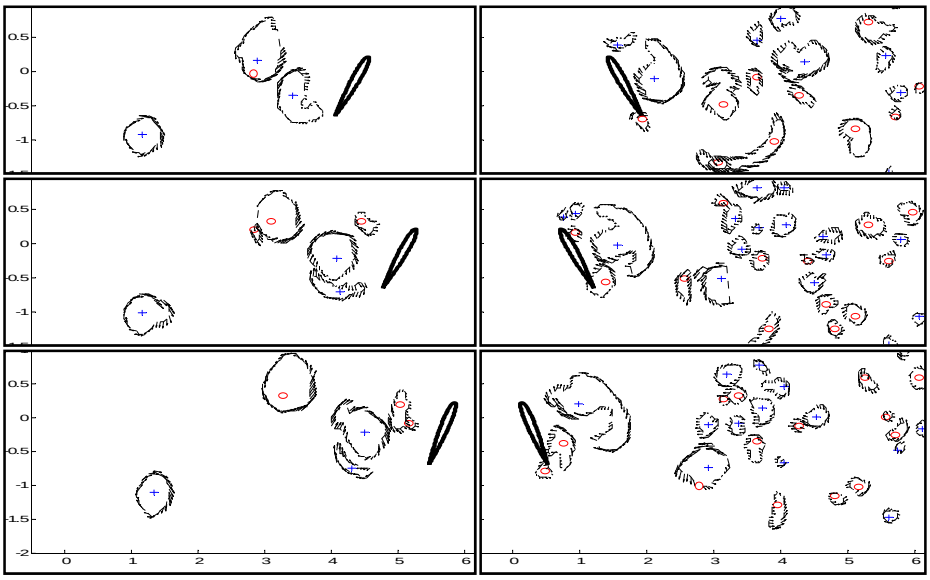

Figure 43 Instantaneous vorticity for α_0=60° beginning from impulsive start (photos are consecutive PIV images during 1st stroke (The centers of the vortices are represented by the symbols **o** for the counter-clockwise vortices and **+** for the clockwise vortices).

The instantaneous circulation data for each vortex formation during the impulsive start (1st period) is represented in Figure 4. Impulsive start effect is visiple on the firstly generated trailing edge vortex TV1. It has a negative circulation sign. Both the generated leading edge vortex (LEV1) and trailing edge vortex – TV1) have influences on the flowfield domain during the both upstroke and the downstroke of the motion.

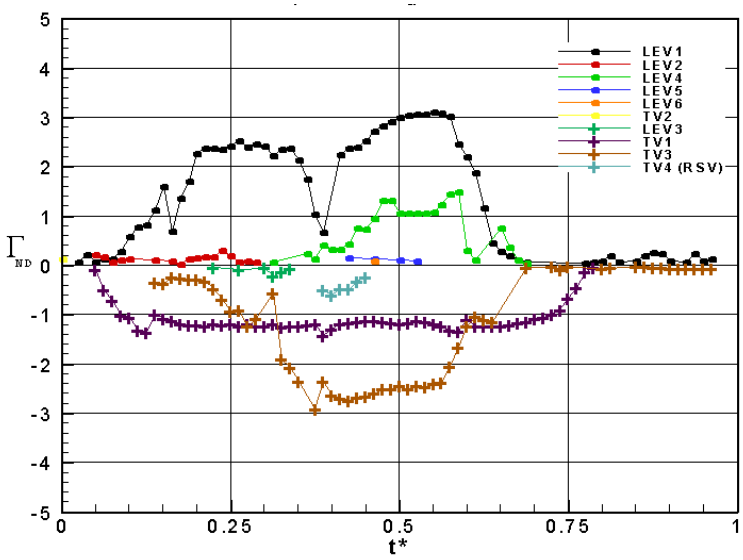

Figure 44 Instantaneous non-dimensional circulation for α_0=60° beginning from impulsive start. The vortices generated during the first half-stroke. (LEV: leading edge vortex, TV: Trailing edge vortex, RSV: Rotational stopping vortex).

At stroke reversal, the shedding of the leading edge vortex and rotational vortex forms a counter-rotating pair which imposes a fluid flow towards the lower surface of the wing at the onset of the next stroke (Birch and Dickinson, 2003). The vorticity shedding from the previous stroke influences the force production (Birch and Dickinson 2003).

Figure 45 represents the vortices generated during the first half-stroke of the flapping motion. As it is notices, all the vortices are generated before t*=0.5. The LEV1 (leading edge vortex), represented with black circle on the figure is the most dominant vortex in the flowfield. Until the end of the translation phase, we observed that

its circulation increases gradually. When the airfoil starts to its rotation, first we observed that the circulation of the LEV1 decreases and then increases very strongly until the end of the rotational motion.

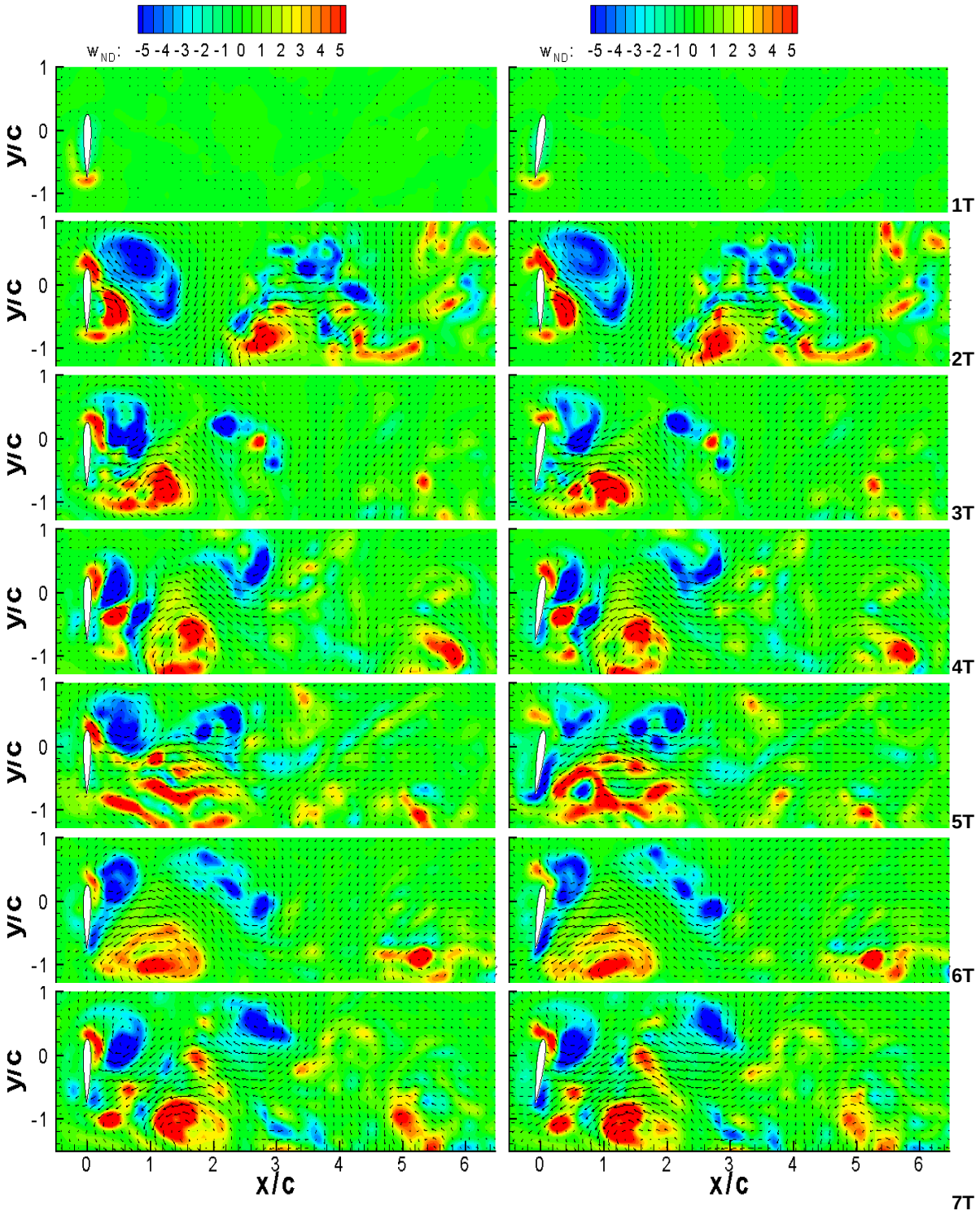

Figure 45 Instantaneous vorticity and velocity vectors relative to flapping translational velocity for α_0=60° (beginning of upstroke during different periods [from 1T to 7T])

The instantaneous vorticity contours during the impulsive start are represented in Figure 46 for two angles of attack distribution where the constant angle of attack α_0 is reached at $x_a=2c$.

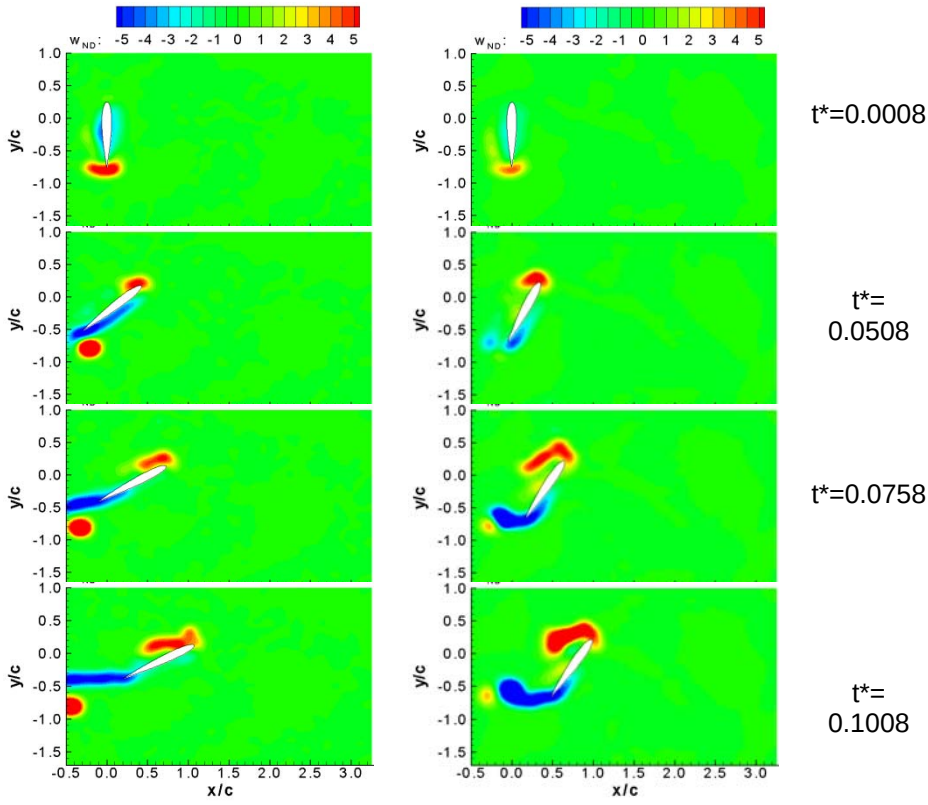

Figure 46 Instantaneous non-dimensional vorticity contours for impulsive start of the flapping motion from 90° to 30° (left column) and from 90° to 60° (right column) by PIV measurements

With the impulsive rotation and translation of the airfoil, a counter-clockwise trailing edge vortex is observed with a positive circulation. This trailing edge vortex detaches from the airfoil surface and is pushed outside the near wake where takes place one negative circulation trailing edge vortex. It is noted that, this first impulsive trailing edge vortex is stronger for $\alpha_0=30°$ since the instantaneous angular velocities are much bigger for this case. In the mean time, a leading edge vortex is growing with a positive circulation value. At $t^*=0.0133$, just after the motion of the airfoil starts, this counter-clockwise leading edge vortex starts to be visualized clearly and it grows up with the airfoil motion. The non-dimensional circulation, Γ/V_0c, of this leading edge vortex for $\alpha_0=60°$ case is nearly twice of the one for $\alpha_0=30°$ (Figure 47). Similar vortex topologies are observed both for $\alpha_0=30°$ and $\alpha_0=60°$ angles of attack cases however the traces of the leading and trailing edge vortices are more attached to the airfoil surface for $\alpha_0=30°$ case.

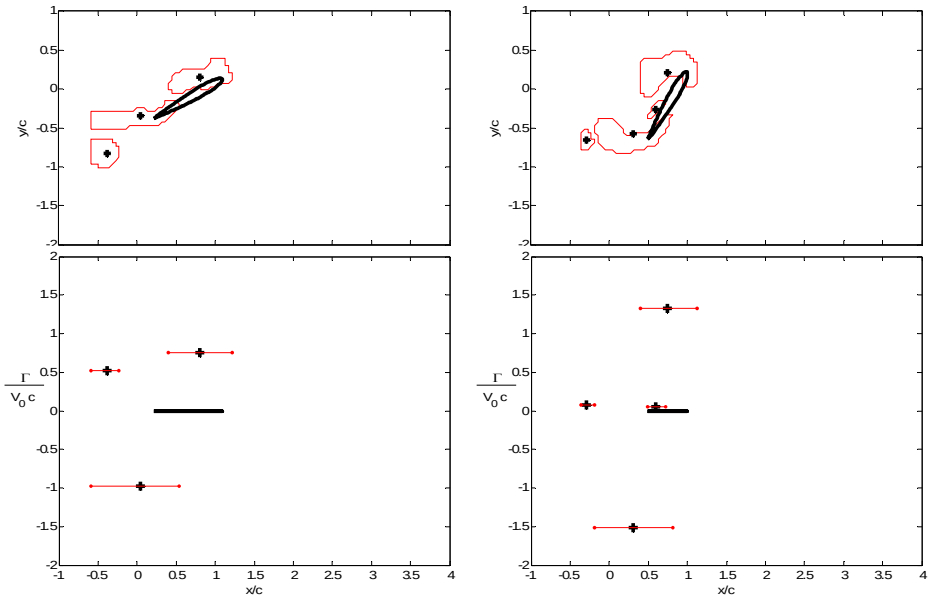

Figure 47 Instantaneous circulation of the vortices by PIV measurements for α_0=30° (left column) and α_0=60° (right column) at t*=0.1008

Conclusion and Perspective

The aim of the present study was to identify the unsteady vortex structures during a flapping motion in hover mode at Re=1000. Particle Image Velocimetry measurements are used in order to identify vortices generated during the flapping motion for different parameters. The complex instantaneous vortex dynamics is investigated first at the impulsive start region and then in the quasi-periodic region where the impulsive effect is lost. The instantaneous flow topology shows the importance of the interaction of the vortices generated with the trace of the vortices from the previous stroke.

References

Ansari SA, Zbikowski R, Knowles K (2006) Aerodynamic modelling of insect-like flapping flight for micro air vehicles. Prog Aerospace Sci 42:129-172

Birch J.M and Dickinson MH (2003) The influence of wing-wake interactions on the production of aerodynamic forces in flapping flight *J. Exp. Biol.* 206, 2257-2272

Dickinson MH, Götz KG (1993) Unsteady Aerodynamic Performance of Model Wings at Low Reynolds Number. J Exp Biol 174:45-64.

Dickinson MH (1994) The effects of wing rotation on unsteady aerodynamics performance at low Reynolds numbers J Exp Biol 192:179-206

Dickinson MH, Lehmann FO, Sane SP (1999) Wing Rotation and the Aerodynamic Basis of Insect Flight. Science 284: 1954-1960.

Freymuth P (1990) Thrust generation by an airfoil in hover modes. Exp in Fluids 9:17–24

Galvao R, Israeli E, Song A, Tian X, Bishop K, Swartz S, Breuer K (2006) The Aerodynamics of Compliant Membrane Wings Modeled on Mammalian Flight Mechanics. 36th AIAA Fluid Dynamics Conference and Exhibit, 5-8 June, San Francisco, California.

Koochesfahani MM (1989) Vortical patterns in the wake of an oscillating airfoil AIAA J 27:1200-1205.

Kurtuluş DF, David L, Farcy A, Alemdaroglu N (2008) Aerodynamic Characteristics of Flapping Motion in Hover. Experiments in Fluids, Vol. 44, pp. 23–36

Lehmann FO, Sane SP, Dickinson MH (2005) The Aerodynamic Effect of Wing-Wing Interaction in Flapping Insect Wings. J Exp Biol 208:3075-3092.

Ol M (2007) Vortical Structures in High Frequency Pitch and Plunge at Low Reynolds Number. AIAA-2007-4233, June 2007, Miami, FL

Platzer MF, Jones KD (2006) Flapping Wing Aerodynamics - Progress and Challenges. AIAA-2006-0500, Jan. 2006, Reno, Nevada
Poelma C, Dickson WB, Dickinson MH (2006) Time-resolved reconstruction of the full velocity field around a dynamically-scaled flapping wing. Exp in Fluids 41: 213-225.
Radespiel R, Windte J, Scholz U (2007) Numerical and experimental flow analysis of moving airfoils with laminar separation bubbles. AIAA J 45:1346-1356
Sane SP (2003) The aerodynamics of insect flight. J Exp Biol 206:4191-4208
Sane, S. P. and Dickinson, M. H. (2002). The aerodynamic effects of wing rotation and a revised quasi-steady model of flapping flight. *J. Exp. Biol.*205, 1087-1096.
Singh B, Ramasamy M, Chopra I, Leishman GJ (2005) Experimental Studies on Insect-Based Flapping Wings for Micro Hovering Air Vehicles. 46th Annual Structural Dynamics and Materials Conference 18-20 April 2005,Austin, TX
Sun, M. and Tang, J. (2002). Unsteady aerodynamic force generation by a model fruit fly wing in flapping motion. *J. Exp. Biol.* 205, 55-70.
Tian X, Iriarte J, Middleton K, Galvao R, Israeli E, Roemer A, Sullivan A, Song A, Swartz S, Breuer K. (2006), "Direct Measurement of the Kinematics and Dynamics of Bat Flight. 36th AIAA Fluid Dynamics Conference and Exhibit, 5-8 June 2006, San Francisco, California.
Usherwood JR, Hedrick LT, McGowan CP, Biewener AA (2005) Dynamic Pressure Maps for Wings and Tails of Pigeons in Slow, Flapping Flight, and Their Energetic Implications. J Exp Biol 208:355-369.
Wang JZ, Birch JM, Dickinson MH (2004) Unsteady Forces and Flows in Low Reynolds Number Hovering Flight: Two-Dimensional Computations vs Robotic Wing Experiments. J Exp Biol 207:449-460.
Wagner, H. (1925). Über die Entstehung des dynamischen Äuftriebes von Tragflügeln. *Z. Angew. Math. Mech.* 5, 17-35.
Viieru D, Tang J, Lian Y, Liu H, Shyy W (2006) Flapping and Flexible Wing Aerodynamics of Low Reynolds Number Flight Vehicles. AIAA 2006-503, 9 - 12 January 2006, Reno, Nevada, pp.1-18

2.2 **Design of a Four Wing Hovering MAV with Cooperating Slider Crank Mechanism**

(by Mehmet Kilic, M.Sc student ME METU, Asst. Prof. Dr. D. Funda Kurtulus AE METU, Asst. Prof. Dr. Yigit Yazicioglu ME METU)

This study examines the properties of the two dimensional four bar mechanism and the cooperating slider crank mechanisms for flapping wings. A detailed derivation procedure is given for the cooperating slider crank mechanisms. It is also noted that when the cranks of the slider crank mechanisms coincide, the kinematics of the mechanism simplifies greatly. It is also noted that with a cooperating slider crank mechanisms, symmetrically working wings can easily be obtained. The parts of the micro air vehicle utilizing this mechanism was designed, manufactured and tested for the required motion. As a future work, the flexible membrane wings will be added to the mechanism and dynamic lift forces will be measured.

1 - Introduction

With a more general sense, the wing of a micro air vehicle can make at most three rotations. So that, any motion required from the wing can be obtained. But an increased degree of freedom results in a complicated mechanism and the weight of the micro air vehicle increases which is not favored. Then researchers turn their faces to low degree of freedom and low weight mechanisms. To obtain a one degree of freedom flapping motion, the first mechanisms visited are the two dimensional and the three dimensional four bar mechanisms. There are several successful examples on this line at the literature (See Figure 48 and Figure 49).

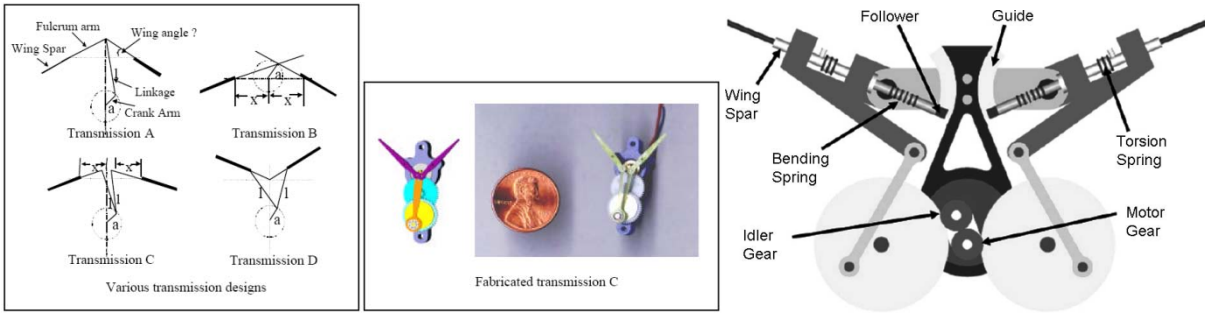

Figure 48 The transmission designs with two dimensional four bar mechanisms. Microbat at the left [1, 2], and Mechanical Humming Bird at the right [3]

Figure 49 The transmission designs with two dimensional four bar mechanisms. Delfly I [4] at the up
The transmission designs with three dimensional four bar mechanisms. Delfly II [4] at the down

2 - Design of a Two Dimensional Four Bar Mechanism for Flapping

With a four-bar mechanism, more specifically with a crank rocker type one, we can easily obtain a flap motion (See Figure 50).

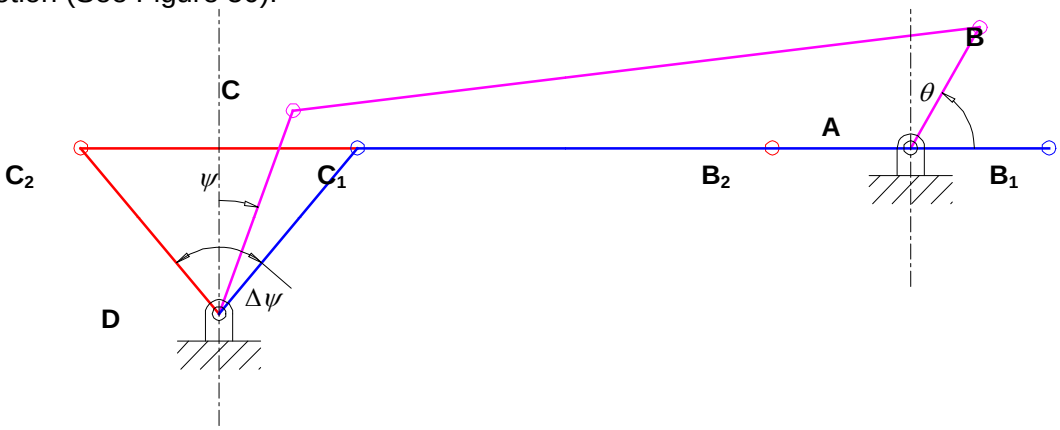

Figure 50 Crank rocker type four bar mechanism. AB is the crank and DC is the rocker.

At hovering flight, we expect the wing make the same motion during the downstroke and the upstroke. We cannot totally fulfill this task with a four bar mechanism, but the timing of the downstroke and the upstroke can be aligned. When θ is 0 and 180º, the rocker can happen to be at the dead centers. These two positions are shown at Figure 50. If the rocker is forced to swing $\Delta\psi$ much during the flaps, then there appear the following relations.

$$|DC| = \frac{|AB|}{\sin(\Delta\psi/2)} \tag{1}$$

$$|AD| = \sqrt{|BC|^2 + \left(\frac{|AB|}{\tan(\Delta\psi/2)}\right)^2} \tag{2}$$

Notice here that we can play with three parameters: $|AB|$, $|BC|$ and $\Delta\psi$. For $|AB|$ = 10 mm, $|BC|$ = 50 mm and $\Delta\psi$ = 80 degrees, the deviation of ψ with respect to θ is given in Figure 55 (. For comparison, a cosine curve is also given. As it is seen, the resultant swinging motion deviates from cosine curve. When the crank is rotating with a constant angular velocity, the downstroke and the upstroke takes same amount of time but the motion differs from each other greatly. If $|BC|$ were selected to be longer, the motion curve would approach the cosine curve more.

3 - Design of a Cooperating Slider Crank Mechanism for Flapping

Consider two inline slider crank mechanisms using the same slider (See Figure 51). The link AB drives the blue slider crank mechanism. Then, the slider drives the pink slider crank mechanism. Although link AB makes full rotation, now link ED makes a swinging motion.

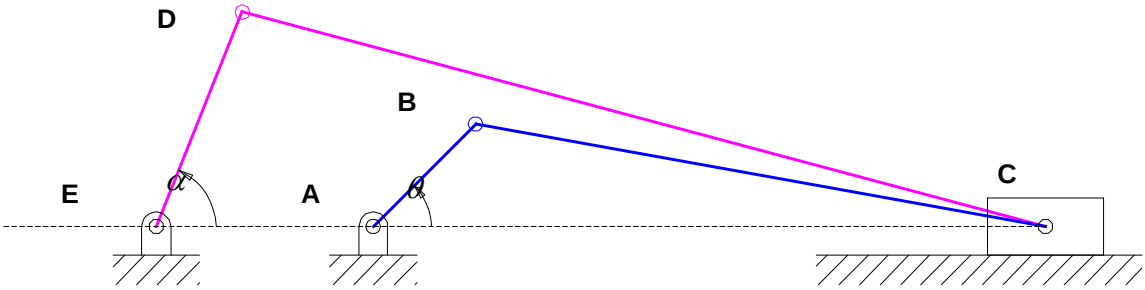

Figure 51 Cooperating slider crank mechanisms

We want to correlate the angular position of link ED with the angular position of link AB. That is, a correlation between α and θ. An arbitrary function relating α to θ cannot be realised for all angles to be satisfied with the cooperating slider crank mechanisms, yet, we can approximate it satisfying the function at the precision points. Like, when θ is θ_1, α is α_1 and when θ is θ_2, α is α_2, etc.

When we assign the dimensions of links AB and BC, we will know the locations of the slider point C. Let the distance between the slider and point E, (that is, $|EC|$), is S. Now the correlation problem reduces to correlating the rotations of the link ED with the slider distance S.

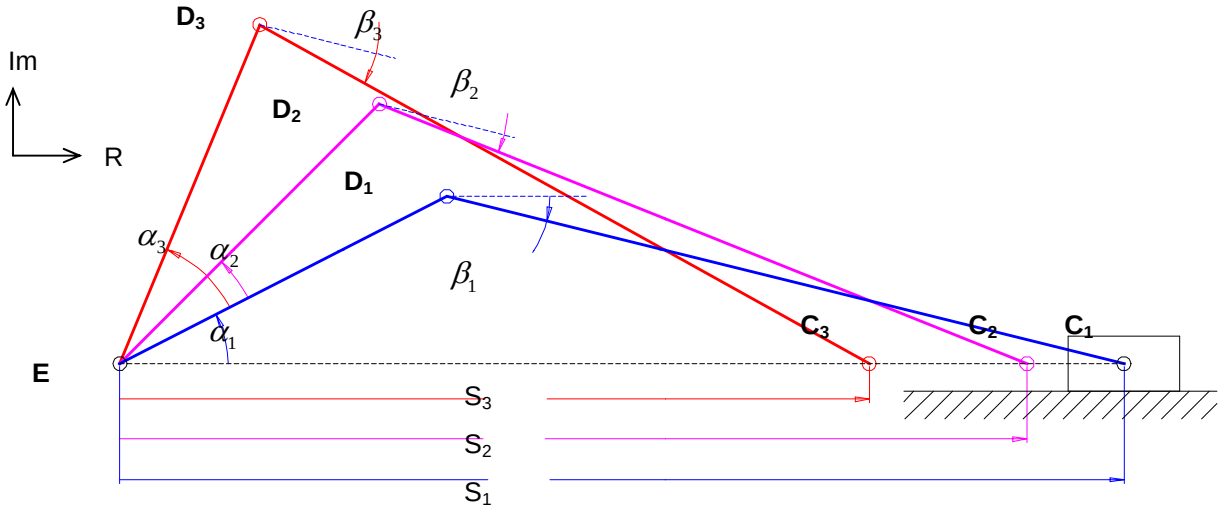

Figure 52 Inline slider crank mechanism

The possible three positions of the slider crank mechanism are given in Figure 52. At the first position, to fully define the mechanism, we have in total 4 parameters. Namely, $|ED|$, α_1, $|DC|$ and

β_1. On the other hand, satisfying the first position imposes only two kinematic equations. That is, 4 parameters and corresponding 2 equations. Now we assume the task as follows; when the slider translates from S_1 to S_2, link ED deviates α_2 much. Here, we gain another two kinematic equations with the cost of a new parameter, β_2. Then in total, 5 parameters and corresponding 4 equations. In a similar manner, satisfying a third position similar to the second, we will have 6 parameters; $|ED|$, α_1, $|DC|$, β_1, β_2 and β_3, and the corresponding 6 kinematic equations. This problem can be solved analytically and it is explained below.

In complex plane, the 6 kinematic equations can be expressed with 3 vector equations,

$$\overrightarrow{ED} + \overrightarrow{DC} = S_1 \tag{3}$$

$$\overrightarrow{ED}\, e^{i\alpha_2} + \overrightarrow{DC}\, e^{i\beta_2} = S_2 \tag{4}$$

$$\overrightarrow{ED}\, e^{i\alpha_3} + \overrightarrow{DC}\, e^{i\beta_3} = S_3 \tag{5}$$

where

$$\overrightarrow{ED} = |ED|\, e^{i\alpha_1} \tag{6}$$

$$\overrightarrow{DC} = |DC| e^{i\beta_1} \tag{7}$$

Observing the equations 3, 4 and 5; we see that they are linear in terms of $\overrightarrow{ED}$ and $\overrightarrow{DC}$, but the equation set is over defined. Then, the determinant of the augmented matrix must be zero.

$$\begin{vmatrix} 1 & 1 & S_1 \\ e^{i\alpha_2} & e^{i\beta_2} & S_2 \\ e^{i\alpha_3} & e^{i\beta_3} & S_3 \end{vmatrix} = 0 \tag{8}$$

Manipulating the determinant,

$$-\overrightarrow{\Delta_1} + \overrightarrow{\Delta_2}\, e^{i\beta_2} - \overrightarrow{\Delta_3}\, e^{i\beta_3} = 0 \tag{9}$$

where

$$\overrightarrow{\Delta_1} = S_3 e^{i\alpha_2} - S_2 e^{i\alpha_3} \tag{10}$$

$$\overrightarrow{\Delta_2} = S_3 - S_1 e^{i\alpha_3} \tag{11}$$

$$\overrightarrow{\Delta_3} = S_2 - S_1 e^{i\alpha_2} \tag{12}$$

The solution of equation 9 can be treated graphically (See Figure 53). It is clear that there are either two solution set or no solution (remember that the dashed circles can not intersect).

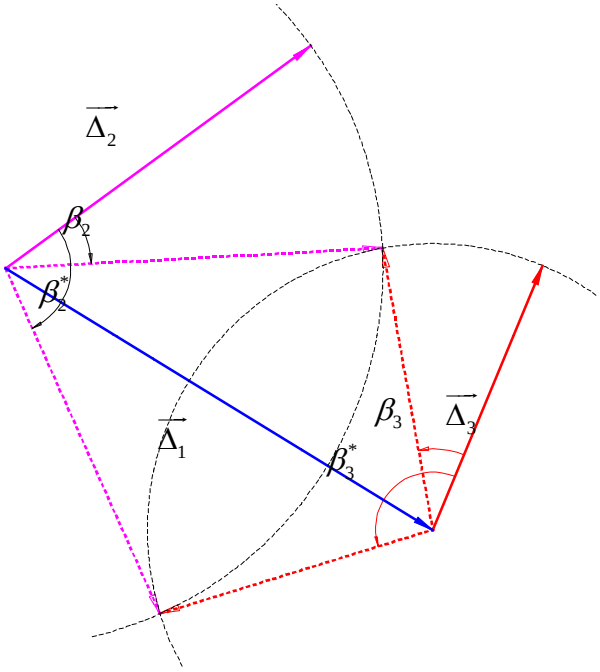

Figure 53 Graphical resolution to Equation 9

After finding the value of β_2, we insert it into Equation 4, and Equations 3 and 4 can now be solved for $\overrightarrow{ED}$ and $\overrightarrow{DC}$. Then using Equations 6 and 7, we calculate the remaining unknown parameters and the mechanism is fully designed.

With the four bar mechanism that have been designed, we guaranteed that, ψ is 40º when θ is 0 and ψ is -40 º when θ is 180 º. With a cooperating slider crank mechanisms, we can further force the system to ψ is 0 when θ is 90 º. So the ψ deviation with respect to θ will imitate the cosine curve better. The problem was solved for $|AB|$=10, $|BC|$=40, $|AE|$=15, θ_2= 90º, α_2= 40º, θ_3= 180º and α_3= 80º. One of the two possible solution sets resulted in infinite $|ED|$ and $|DC|$, then only one solution was possible and shown in Figure 54.

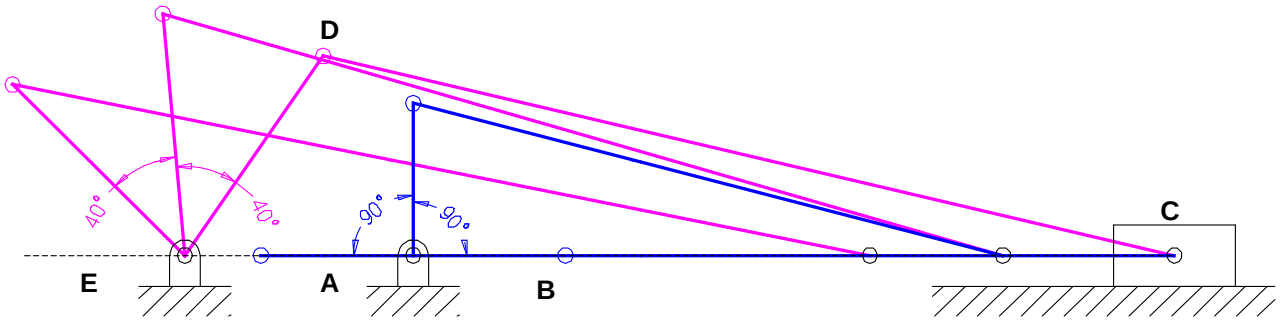

Figure 54 Cooperating slider crank mechanism satisfying the precision points.
$|AB|$=10, $|BC|$=40, $|AE|$=15, $|ED|$=15,94 and $|DC|$=57,43

Cooperating slider crank mechanism is superior to two dimensional four bar mechanism in some other ways other than approximating the cosine curve better. Firstly, it benefits from the symmetry of the inline nature. By default, the ψ deviation with respect to θ will be symmetric with respect to θ = 180º line like the cosine curve. That is, the upstroke of the flap is totally the same as the downstroke. The two dimensional four bar mechanism, on the other hand, does not have such a property (See Figure 55). Secondly, one can easily be place a second flapping wing to the cooperating slider crank mechanism which flaps symmetrical to the first wing (See Figure 56).

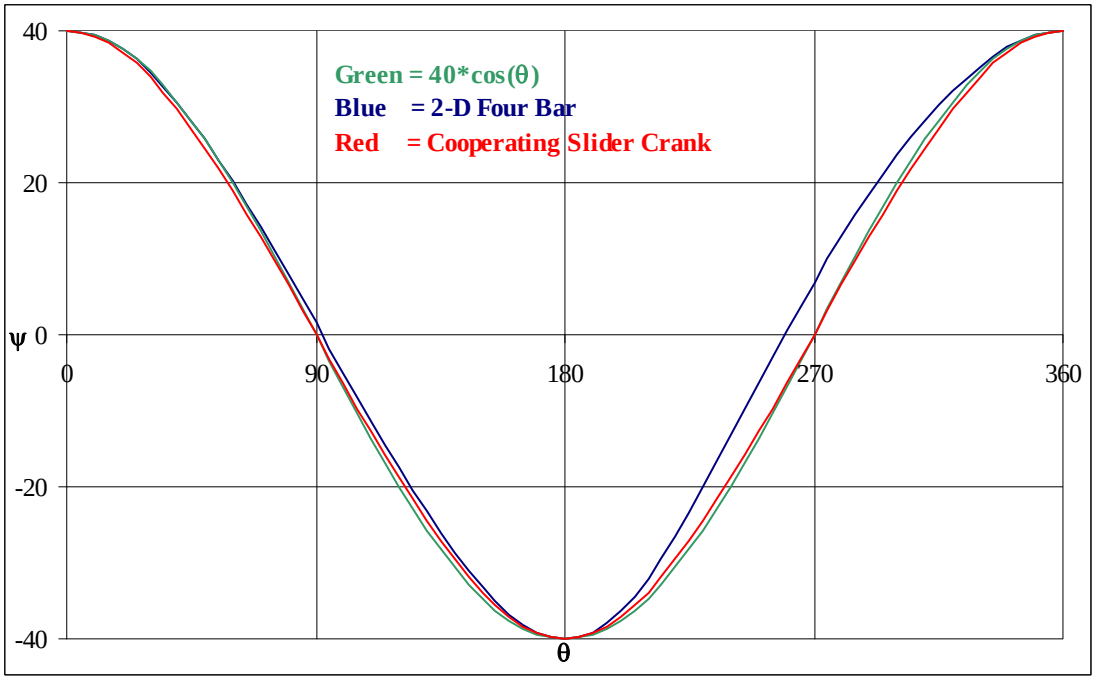

Figure 55 ψ versus θ

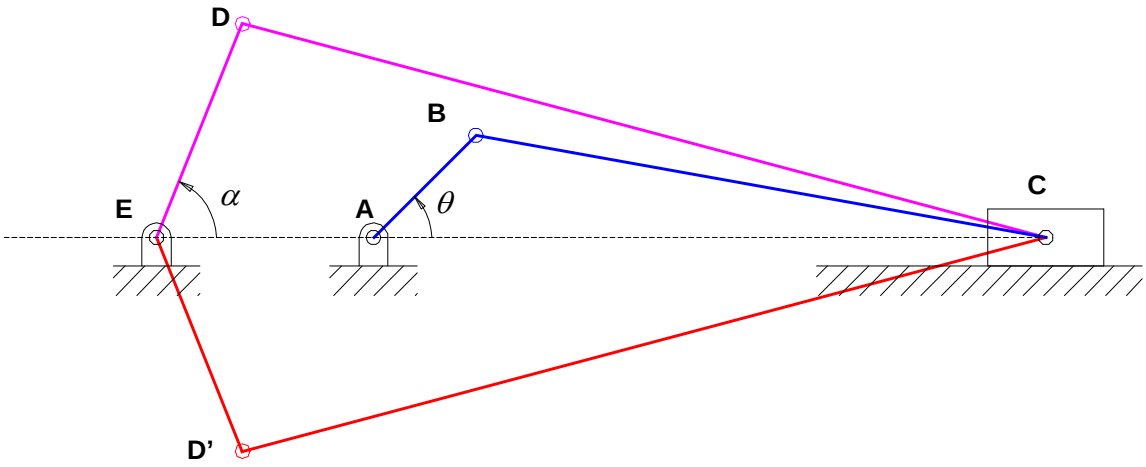

Figure 56 Cooperating slider crank mechanisms actuating 2 wings.
ED and ED' are symmetrically working wing arms.

4 - The Cooperating Slider Crank Mechanism used in our design

After feeling the merits of the cooperating slider crank mechanism, we intended to use it for the proposed design. There were some restrictions for the parts. First of all, we desire to obtain the wing wing interaction at the ends of the two strokes. Therefore, the only way to rotate the crank is driving it with a shaft passing through a hole at the rotation center of the wings. That means the $|AE|$ will be zero. This special case resulted in a more facilitated design procedure for the cooperating slider crank mechanism. Instead of the design procedure given in part 3, the following rules suffice.
When $|AD|$, $|DC|$, $\Delta\psi$ are given,

$$|AB| = |AD| \sin(\Delta\psi/2) \qquad (13)$$

$$|BC| = \sqrt{|AB|^2 + |DC|^2 - |AD|^2} \tag{14}$$

The problem was solved for $|AD|$=25, $|DC|$=45,25 and $\Delta\psi$ =80º and shown in Figure 57.

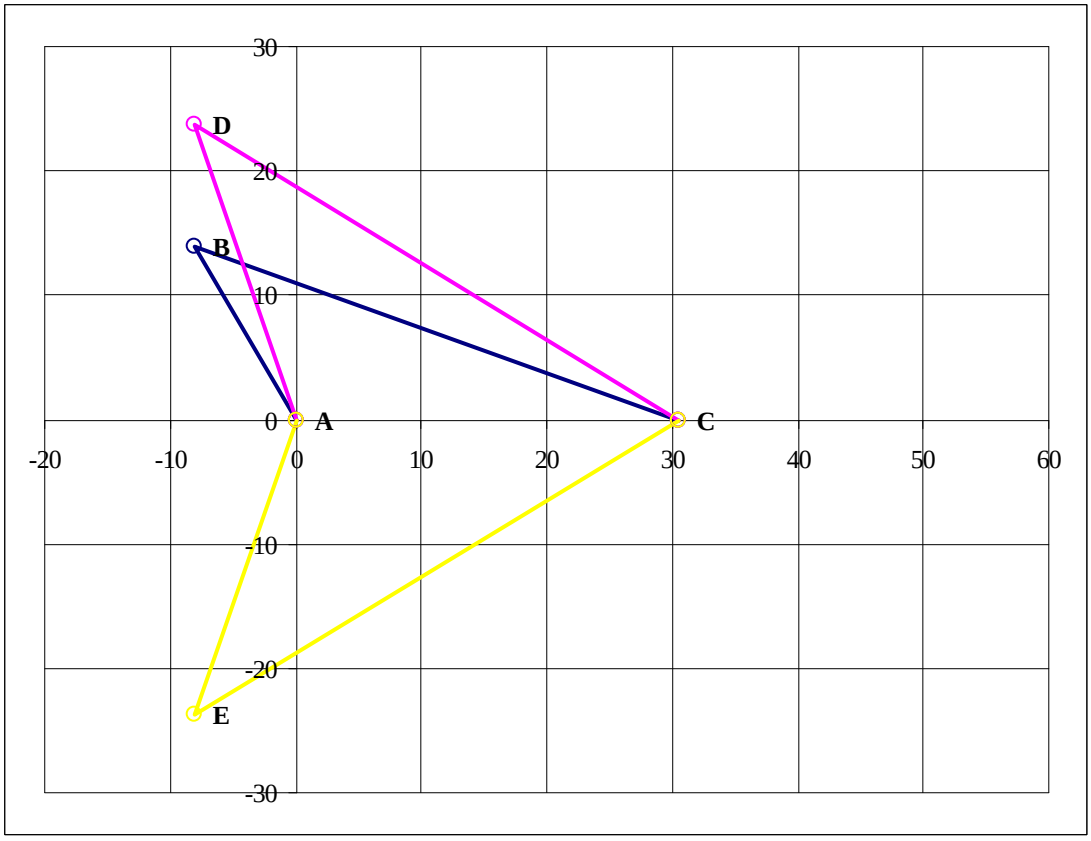

Figure 57 Cooperating slider crank mechanisms satisfying the precision points.
$|AD|$=25, $|DC|$=45,25, $\Delta\psi$ =80º , $|AB|$=16,07and $|BC|$ =41

The Equation 14 guaranties that line DB is always perpendicular to line AC. Then a simple explicit relation between ψ and θ can be obtained.

$$\psi = a\sin\left(\frac{|AB|}{|AD|}\cos(\theta)\right) \tag{15}$$

The mechanism working with this principle was manufactured and tested for the required motion (See Figure 58). All parts were made up of aluminum. The wing spars are 2 mm thick carbon fiber rods.

Currently, we work on the membrane wing geometry and the wing stiffener locations. We intend to measure real time lifting force history using sensitive force transducers. Hopefully, the correct dimensions will be found for the most efficient lifting force generation.

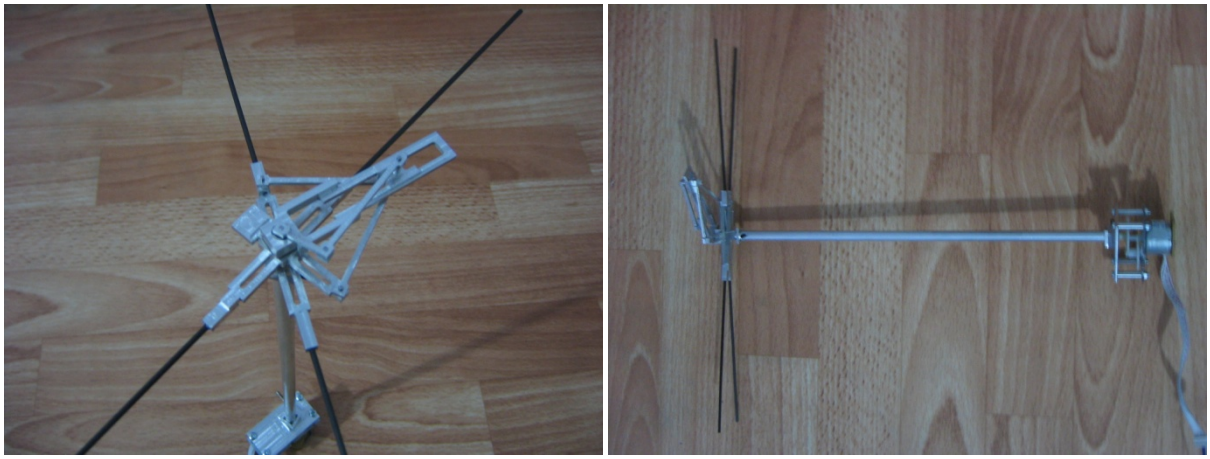

Figure 58 The mechanical flapper using cooperating slider crank mechanisms.

5 - References

[1] Pornsin-sirirak TN, Tai YC, Nassef H, Ho CM "Titanium-alloy MEMS Wing Technology for a Micro Aerial Vehicle Application", Sensors and Actuators A: Physical Volume 89, Issues 1-2, 20 March 2001, Pages 95-103.

[2] Pornsin-sirirak TN, Tai YC, Ho CM, M Keennon, "Microbat: A Palm-Sized Electrically Powered Ornithopter", Proceedings of NASA/JPL Workshop on Biomorphic Robotics, 2001.

[3] McIntosh, Sean H., Agrawal, Sunil K., Khan, Zaeem., "Design of a Mechanism for Biaxial Rotation of a Wing for a Hovering Vehicle," IEEE/ASME Transactions of Mechatronics, Vol. 11, No. 2, April 2006.

[4] www.delfly.nl last viewed on March 2th 2009.

2.3 Experimental Setups at AE METU

(by Hasan Hizli, M.Sc student AE METU, Asst. Prof. Dr. D. Funda Kurtulus AE METU with collaboration of Robotics & Mechatronics Technologies Ltd)

As it is explained in Report 1, we were at the stage of establishing the new experimental setup and a water supply system to the laboratory that is given to me as a research area. The water supply system has been added and the new experimental setup has been designed for water tank (Figure 59). Tests of the experimental setup will be started on September 2009.

Figure 59 Water tank (2m length)

Introduction

Research Pool Positioning System (RPPS) is an advanced laboratory platform designed to accurately position airfoils within research pools during experiments. The system enables users to move and locate airfoil equipment in two dimensions both longitudinal and rotational and provides logging for the complete motion during operation. RPPS can control and log the motion of the equipment in real-time through a PC installed Data Acquisition Board and Matlab/Simulink™ software.

RPPS can perform the following demonstrations and experiments:

- Linear position and rotation control of the cart mounted airfoil.
- Real-time linear and rotational position data tracing and logging.
- On the fly parameter updating.

Besides the basic functionalities given above, the system can be equipped with additional sensors to make calibration, estimation, identification and control practices in the laboratory.

The block diagram of RPPS is presented in Figure 60.

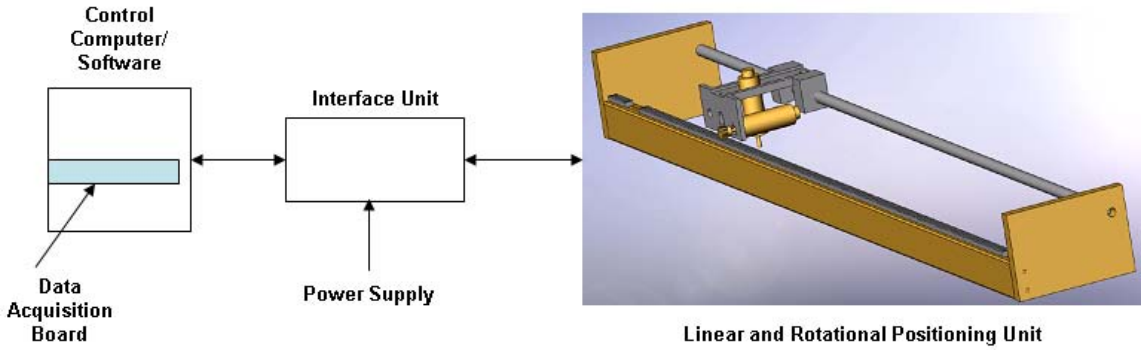

Figure 60 System Block Diagram.

System Components

System shown in Figure 60 is explained in details below.

Positioning Unit

Positioning Unit (PU), is the basic mechanical structure which holds the cart via the rack and the linear bearing. The main construction is composed of high quality machined aluminum housing and holds a custom precision machined rack. A picture of PU is available in Figure 61.

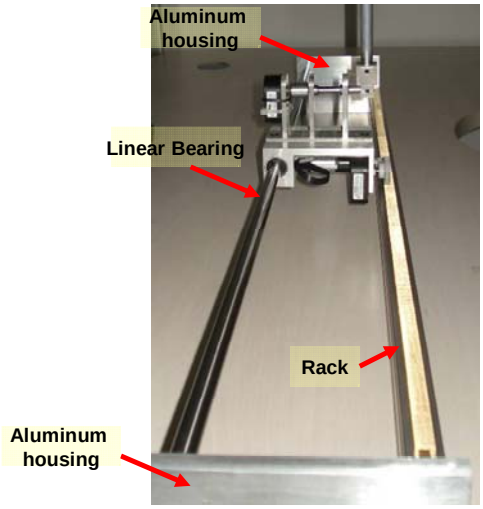

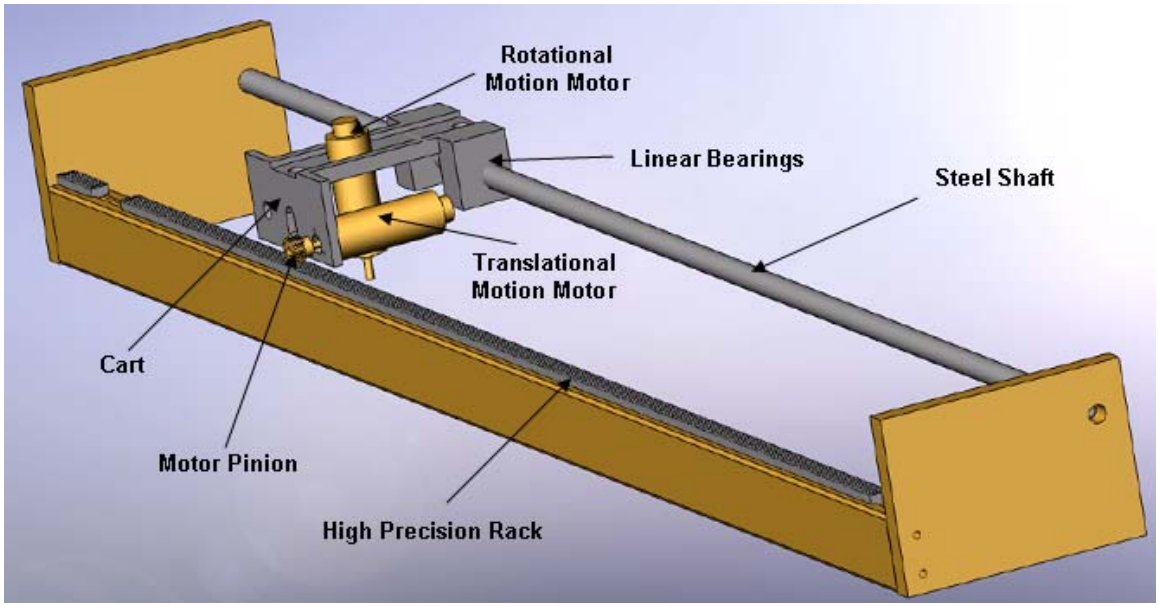

Figure 61 Positioning unit.

Cart

The Cart carries the airfoil equipment and moves along the rack via the pinion mounted on the motor. The linear position control of the airfoil is achieved with the motion of the cart. A cart mounted independent mechanism controls the rotational motion of the airfoil.

The cart consists of the carrier platform and two drive motors with embedded gear trains and encoders for translational and rotational motion of the airfoil.

The Cart uses high quality gear motors for translational and rotational motion along the rack (**Figure 62**). The geared motor has an embedded encoder for measuring direct position of the pinion during cart motion. The precision gear motor is a low power motor with high efficiency for smooth and quite operation in a small volume. The specifications for the motor are given below.

Figure 62 Cart motor with embedded encoder.

Motor:

Motor Data	Units	Value
Assigned power rating	W	5.0
Nominal voltage	Volt	6.0

Gearhead:

Gearhead Data	Units	Value
Planetary gearhead reduction	-	19:1
Number of stages	-	2

Digital Encoder:

Magnetic digital encoder provides 16 counts per turn. The encoder is embedded to the drive motor.

Interface Box

Interface Box (IB) is the main junction box between the data acquisition board, power supply and motors. The block diagram of the box is given below:

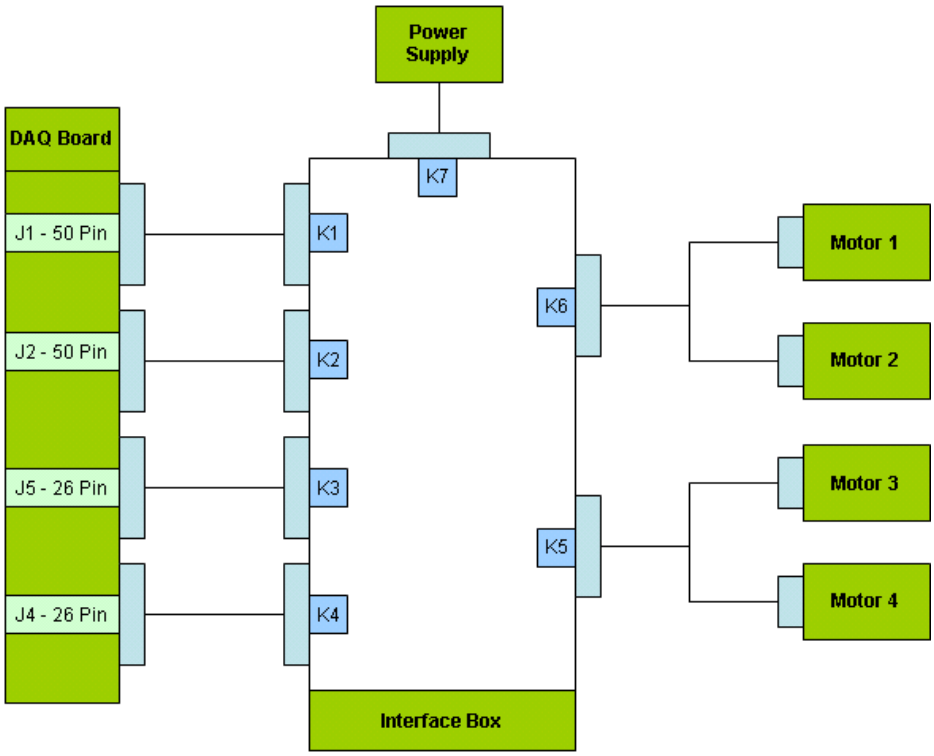

Figure 63 Interface Box block diagram.

Control inputs to the motor and sensor signals from the encoder are passed through the interface box. IB also contains electronics that provides motor driving and power distribution among units.

Motor Driver Electronics

Positioning unit driving motors is driven by pulse width modulation (PWM) signals through commands received from the controller PC through data acquisition board (**Figure 64**).

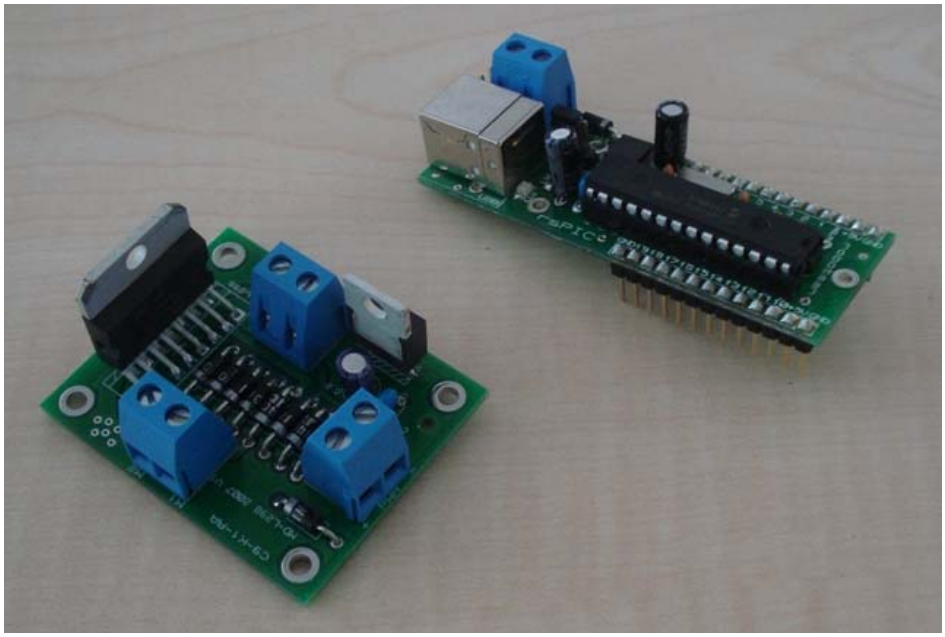

Figure 64 Motor driver electronics (Robotsan RS-MD02 and rsPIC units).

Motor driving is accomplished through Robotsan's RS-MD02 Motor Driver and rsPIC Intelligent Controller units.

Data Acquisition Board

Data Acquisition Board (DAQ Board) serves as the signal acquisition and command generation electronics onboard the PC. Encoder signals and motor driving logic and commands are generated on the DAQ Board. The board is also compatible with Matlab/Simulink™ and Real-Time Workshop® software enabling real-time implementations.

Data Acquisition Board used within the system is shown in Figure 65.

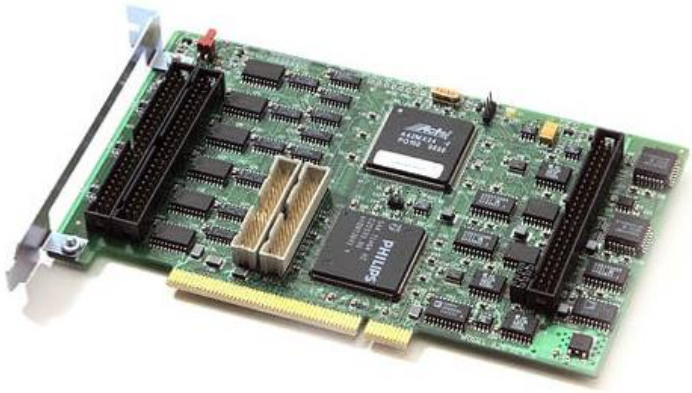

Figure 65 Data Acquisition Board.

Features of the board are listed below:

- Sixteen 16-bit differential A/D inputs, 15 kHz rate
- Four 14-bit D/A outputs, 20 kHz update rate
- 48 bi-directional digital signals
- Six quadrature encoder inputs
- Driver for Real-Time Windows Target
- Driver for xPC Target
- Driver for Windows

Real Time Control Software

Real-Time Windows Target™ rapid prototyping software is a PC solution for prototyping and testing real-time systems. Real-Time Windows Target software uses a single computer as a host and target. On this computer, you use the MATLAB® environment, Simulink® software, to create models using Simulink® blocks and Stateflow® diagrams.

After creating a model and simulating it using Simulink software in normal mode, you can generate executable code with Real-Time Workshop® code generation software and the C/C++ compiler. Then you can run your application in real time with Simulink external mode.

Integration between Simulink external mode and Real-Time Windows Target software allows you to use your Simulink model as a graphical user interface for

Signal visualization — Use the same Simulink Scope blocks that you use to visualize signals during a non-real-time simulation to visualize signals while running a real-time application.

Parameter tuning — Use the Block Parameter dialog boxes to change parameters in your application while it is running in real time.

Operating RPPS

Simulink Interface

This section describes the Simulink blocks used to interface with the RPPS hardware. The following explains these interfaces and provides notes on their usage:

Actuator Block

This block enables the user to provide a control signal to drive the motors for both translational and rotational motion.

The input of the block is a voltage between 0-5V's.

The outputs of the blocks are:

- an analog signal on the DAC output of DAQ providing the required drive voltage on the motor,
- control of two Digital Outputs on the DAQ providing direction control of the motor.

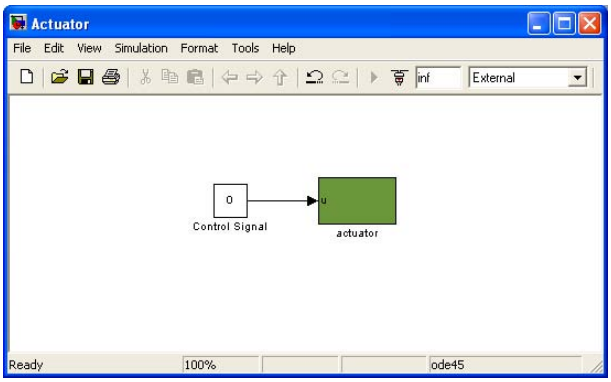

Figure 66 Actuator Block used for driving the motors.

The block determines the sign of the control signal which then calculates the required PWM value and the direction of the actuator. The user is only required to provide the control input.

The subsystem view of the Actuator Block is presented in the next figure.

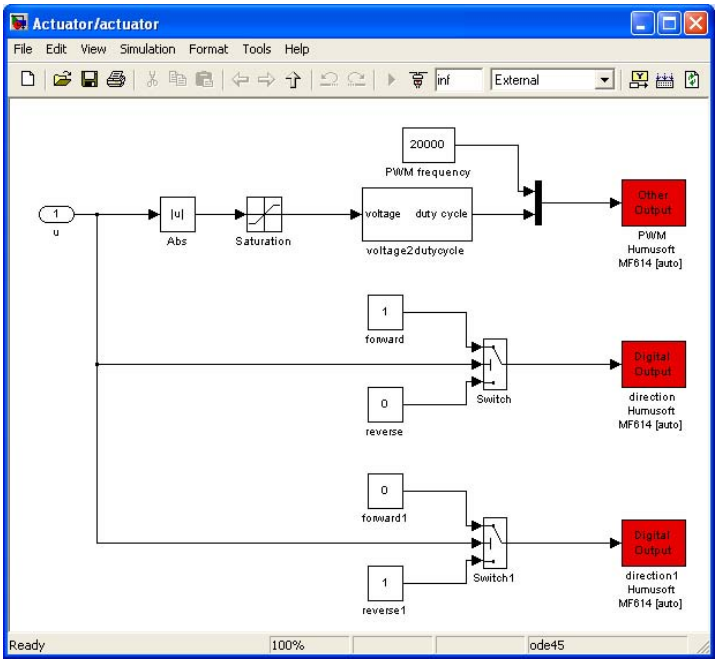

Figure 67 Actuator Block details.

Actuator Feedback Encoder Block

This block enables the user to read the incremental position of the drive motors.

The output of this block is the motor revolutions in encoder steps. The Encoder Input block is used to receive the encoder signals from the DAQ (Channel 3). A view of the block and conversion factors are given below:

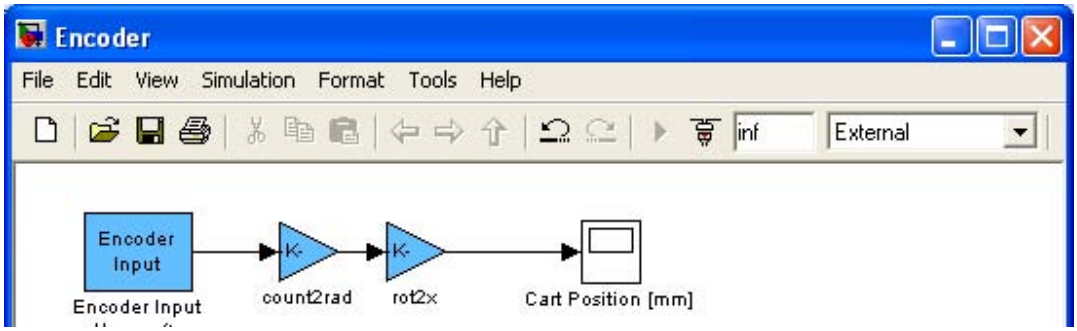

Figure 68 Feedback Encoder Blocks.

The block parameters are also presented in the next figure. In order to increase the resolution of feedback data available the encoder is read in quadrature mode where 1024x4=4096 counts per turn is achieved during encoder readings. The sample time Ts (i.e., 500Hz) should be set from within the Matlab window prior to operation.

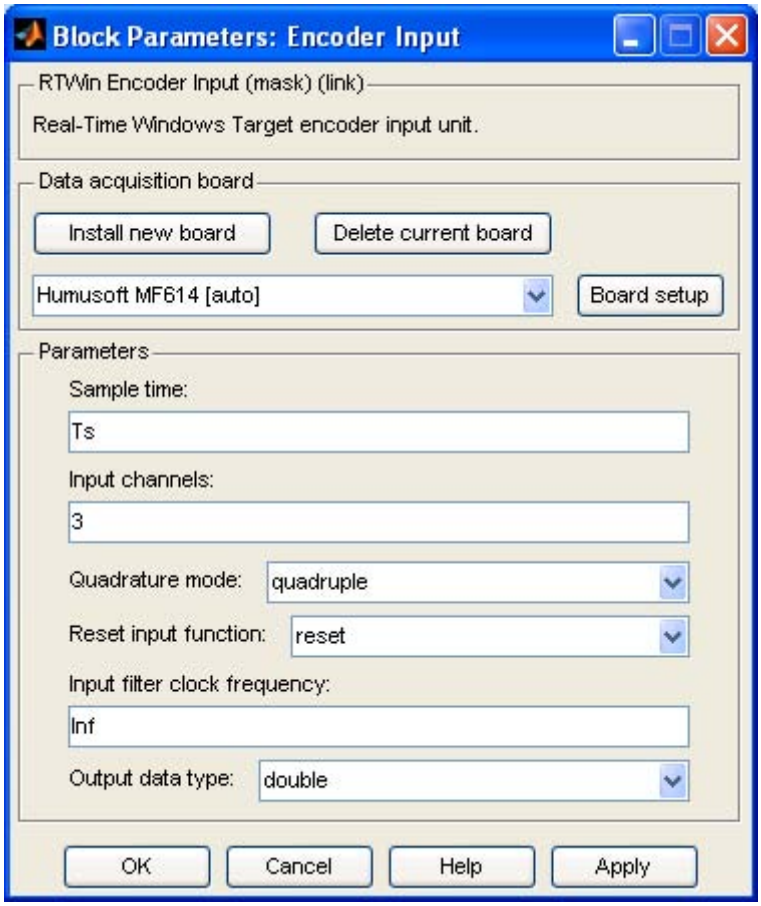

Figure 69 Actuator Feedback Encoder Input Block Parameters.